POLITECNICO DI TORINO

Corso di Laurea Magistrale in

Ingegneria Aerospaziale

Tesi di Laurea Magistrale

Design and simulation of a Radar System
for tracking of objects in Low Earth Orbit (LEO)

Relatori

Fioriti Marco

Manfletti Chiara (TUM)

Candidato

Amoroso Gabriele

Anno Accademico 2023/2024

I

Abstract

The proliferation of objects in Earth's orbit has surged since the launch of the first artificial satellite in 1957, posing significant threats to space security, safety, and long-term sustainability. As of November 1, 2022, the US Space Surveillance Network (SSN) tracks over 22,000 objects, with more than 90% being rocket bodies and debris. However, this covers just around 5% of the risk posed by potentially damaging collisions [13]. The European Space Agency estimates that roughly 900,000 objects sized between 1 and 10 cm are currently untracked [24].

To address this growing challenge, it is imperative to develop ground-based radar systems capable of detecting and tracking resident LEO objects down to 2 cm in diameter. For this reason, precise measurements are essential for extracting Keplerian elements used in orbit propagation. A single radar detection provides limited information, including the position vector and range ratio, which can introduce errors. Orbit determination requires the computation of all 6 Keplerian elements, therefore one potential solution involves utilizing a pair of independent radars, consisting of cylindrical parabolic reflector fed by linear phased array. Each radar points in different directions from the same location, providing the range and the two angular positions of the object. This configuration allows the orbit to intersect both radar fields of view, providing 8 independent information (three-dimensional position and radial velocity for field of view) at least. These data not only facilitate orbit determination but also enhance its accuracy. This study emphasizes the optimization of beam inclination as a means to achieve the highest possible accuracy for orbit determination, making it a focal point of this thesis.

In the initial phase, a basic two-dimensional model of the trajectory is constructed, and its outcomes and constraints are examined. Subsequently, this two-dimensional model forms the foundation for the creation of an advanced three-dimensional trajectory model. This enhanced model enables the incorporation of additional variables regarding to the trajectory of potential objects, expanding the scope of analysis.

After completing the preliminary design of radar parameters, the last step involves the simulation of various scenarios, considering both existing debris and satellite populations in Low Earth Orbit (LEO) to evaluate the radar's tracking performance.

Table of Contents

List of Figures

List of Tables

Acronyms

ECI   Earth-Centered Inertial
FOR   Field Of Regard
FOV   Field Of View
IOD   Initial Orbit Determination
KSR   Kiwi Space Radar
LEO   Low Earth Orbit
PDF   Probability Density Function
PRF   Pulse Repetition Frequency
PRT   Pulse Repetition Period
RAAN Right Ascension of Ascending Node
RCS   Radar Cross-Section
SNR   Signal-to-Noise Ratio
UCT   Uncooperative Space Target
UKF   Unscented Kalman Filter
UT   Unscented Transformation

Chapter 1 : Radar system

1.1   Introduction

This research aims to devise a radar system capable of tracking objects smaller than 10 cm in Low Earth Orbit (LEO). Accurate detection of Resident Space Objects (RSOs) is crucial for activities like satellite collision avoidance, satellite tracking, satellite launch support and general satellite mission operations. Ground operators can alter the satellite's course to avoid collisions if a crash is anticipated. This measure extends the satellite's lifespan and reduces the risk of future collisions caused by debris generating events. As of now, the current systems can only reliably detect and track objects 10 cm or larger. Objects smaller than this can pose a significant threat to satellites yet may go undetected. Therefore, recent advancements in radar systems have focused on increasing the number of cataloged objects. Many of these innovations are based on the concept of electromagnetic "fence," which offers extensive coverage, and it is a promising option for monitoring high-speed LEO objects. Typically, the electromagnetic fence is a system with a field of regard (FOR) which extends widely in the longitudinal direction while staying narrow in the latitudinal direction. This configuration leads to a short time interval for space debris to traverse the fence. It is important between the field of regard, which is the total area that can be captured by a movable sensor and the field of view (FOV), which is the angular cone perceivable by the sensor at a particular instant. A double-fence radar approach has been examined for Low Earth Orbit (LEO) debris monitoring, capable of generating a V-shaped electromagnetic beam [17].

A notable system using this concept is the LeoLabs Kiwi Space Radar (KSR), an S-band radar in New Zealand. The KSR has two autonomous radars, KSR1 and KSR2, each employing two 1-D parabolic reflectors with 1-D phased-arrays at the optical focal points. Their fields of regard are symmetrical with boresights at an elevation of 70°. KSR1's boresight points at -13° azimuth, while KSR2's at 167° azimuth [24]. The radar system's field of regard is shown in Figure 1.1.

In the scanning plane, the array focalizes the energy, while in the elevation plane, the parabolic shape of the reflector aperture assists in focusing. This design significantly diminishes the necessary components, usually by a square root, leading to an economical solution [35]. This setup allows for electronic steering in one dimension, which in turn enables a broad range for identifying objects like debris or satellites. However, compared to 2D arrays, the drawback is the inability to adjust the beam in the elevation direction.

The Kiwi Space Radar (KSR) employs a distinctive method to monitor Uncooperative Space Targets (UCTs). It measures their distance, Doppler velocity, and angular trajectory in a single field of regard, enabling the anticipation of the UCT's position in a second field of regard. Subsequent measurements are planned, resulting in another set of distance, Doppler velocity, azimuth, and elevation measurements taken just minutes later. With a total of eight independent measurements, the KSR facilitates an over-constrained initial orbit determination (IOD) for the newly detected UCT [24].

The primary objective of this study is to investigate the optimal elevation angles of the radar beams to attain the most accurate measurements within this configuration, which will be addressed in this study as "space fence" or "radar system", while each independent radar composing the system is called sensor.

The degree of correlation between the two beams measurements and their accuracy depends significantly on the angular separation between them. In scenarios with minimal angular divergence, due to the high correlation, the improvement in measurement quality is relatively modest. The most extreme case occurs when the elevation angle reaches 90°, causing the beams to align perfectly, resulting in complete measurement correlation. Conversely, as the elevation angle decreases, the distance between the radar and the object increases, leading to a reduction in the signal-to-noise ratio and an increase in the associated uncertainties of measurements.
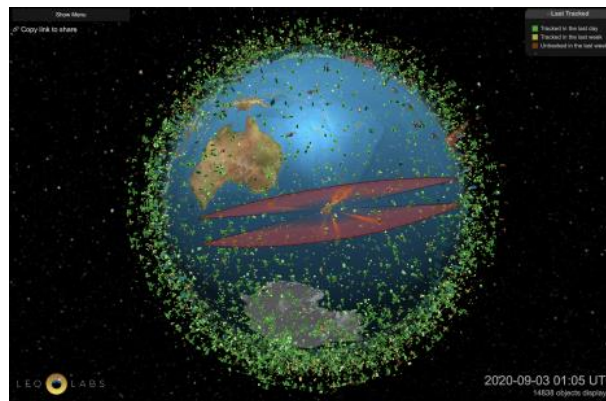
Figure 1.1: Rendering of the KSR, from [21].

1.2   Radar performance equations

Before delving into a detailed analysis of this radar configuration, it is crucial to outline the parameters that influence radar performance. A valuable tool for creating an initial design of a radar system is the radar equation. This equation establishes a connection between the radar's range and several factors, including the transmitter, receiver, antenna, target, and environmental characteristics.

It also acts as a tool for comprehending radar operation and lays the foundation for radar design. One of its key applications is the computation of the signal-to-noise ratio (SNR), a critical factor that determines the accuracy of the radar measurements [31].

1.2.1 Radar Equation

In this section, the simplified form of the radar equation is derived. By denoting the power of the radar transmitter as P_t and using an isotropic antenna (which radiates uniformly in all directions), the power density (expressed in watts per unit area) at a distance ρ from the radar is equal to the transmitter power divided by the surface area of an imaginary sphere with a radius of ρ, which is $4\pi\rho^2$.

However, radar systems typically utilize directive antennas to focus or direct the radiated power, denoted as P_t, into a specific direction. The gain of an antenna, denoted as G, quantifies the increase in power radiated in the direction of the target compared to what would have been radiated from an isotropic antenna. The power density at the target, when using an antenna with a transmitting gain G, can be expressed as:

$$Power\ density\ from\ directive\ antenna\ = \frac{GP_t}{4\pi\rho^2} \tag{1.1}$$

The radar cross-section (RCS) denoted as σ, quantifies the extent to which a target intercepts incident power and reflects it back in the direction of the radar. This parameter is defined by the following relationship:

$$Power\ density\ of\ echo\ signal\ at\ radar\ = \frac{GP_t}{4\pi\rho^2}\frac{\sigma}{4\pi\rho^2} \tag{1.2}$$

The radar cross-section is a property unique to a specific target, serving as a gauge of how the radar perceives its size. When the radar antenna captures a fraction of the reflected signal power, the effective area of the receiving antenna is denoted as A_e. Antenna theory provides a relationship between the transmitting gain and the receiving effective area of an antenna, expressed as follows [25]:

$$G = \frac{4\pi A_{eff}}{\lambda^2} \tag{1.3}$$

therefore, the power P_r, received by the radar is [25]:

$$P_r = \frac{GP_t}{4\pi\rho^2}\frac{\sigma}{4\pi\rho^2}\ A_{eff} = \frac{G^2 P_t}{(4\pi)^3\rho^4}\sigma\lambda^2\ . \tag{1.4}$$

The radar receiver's capacity to detect a weak echo signal faces a limitation imposed by the presence of noise energy sharing the same portion of the frequency spectrum as the signal. In this context, noise refers to unwanted electromagnetic energy that disrupts the receiver's ability to discern the desired signal. This interference may arise from within the receiver itself or enter through the receiving antenna alongside the desired signal. Even in a hypothetical scenario where the radar operates in a perfectly noise-free environment, with no external sources of noise accompanying the desired signal, and the receiver itself is flawless and generates no additional noise, there remains an inherent noise component known as thermal noise or Johnson noise.

This thermal noise is directly proportional to the temperature of the ohmic elements in the receiver's input stages and the receiver's bandwidth. The available thermal noise power generated by a receiver with a bandwidth of B_n (measured in hertz) at a temperature T (in degrees Kelvin) can be expressed as follows [25]:

$$Available\ thermal\ noise\ power = kTB_n. \tag{1.5}$$

where $k = 1.38 \cdot 10^{-23}\ J/K$ (Boltzmann's constant).

It is important to note that the bandwidth B_n discussed here is not the commonly used half-power bandwidth typically employed by electronic engineers. Instead, it is an integrated bandwidth, which can be defined as:

$$B_n = \frac{\int_{-\infty}^{\infty} |H(f)|^2 df}{|H(f_0)|^2}$$ (1.6)

Here, $H(f)$ represents the frequency-response characteristic of the IF amplifier or filter, and f_0 is the frequency of maximum response, which usually occurs at midband. In many practical radar receivers, the frequency-response characteristics are such that the 3-dB bandwidth and the noise bandwidth are quite similar. Therefore, in many cases, the 3-dB bandwidth can be used as an approximation to the noise bandwidth [25].

Practical radar receivers often exhibit noise power levels that exceed what can be attributed to thermal noise alone. Whether the noise originates from a thermal mechanism or some other source, the total noise at the receiver's output can be considered equivalent to the thermal-noise power derived from an ideal receiver, multiplied by a factor known as the noise figure.

Once the system noise temperature is known, it is possible to compute the signal-to-noise ratio (SNR) which is just the ratio between the power of the received signal and the noise power. However, a particular component of the receiver, called matched filter allows to increase the parameter, using a filter response which is "matched" to the signal waveform. It is possible to compute the SNR at the output of the receiver which is given by:

$$SNR = \frac{2P_r\tau}{N_0} = \frac{2E}{N_0},$$ (1.7)

where τ is the pulse duration. This means that the product $P_r\tau$ gives the energy of the received signal. When comparing the signal-to-noise ratio before and after pulse compression, it becomes apparent that the compression gain is equal to the product of the bandwidth and the duration of the pulse.

This SNR is a measure of the power of the pulse reflected by the target relative to the noise level. However, it is important to note that the target may remain inside the radar beam for a duration longer than a single pulse period, allowing it to reflect more than one pulse. This presents an opportunity to enhance the SNR by integrating the reflections from different pulses originating from the same object, taking advantage of the inherent randomness of the noise. In case of coherent integration, the resulting signal-to-noise ratio is just the product of the one given by a single pulse and the number of pulses integrated (M):

$$SNR = M \cdot SNR_1 = M\frac{2E}{N_0},$$ (1.8)

In this case the gain is supposed to be constant inside the radar's beam.

1.2.2 Measurements accuracy

The signal-to-noise ratio plays a crucial role in shaping the accuracy of radar measurements. In the analyses within this section, radar accuracy is quantified by the standard deviation of a Gaussian distribution, represented as σ. This Gaussian distribution serves as a reasonable model for characterizing measurement errors in many cases of interest. In practical applications, it is often useful to express the boundaries of the error distribution in terms of multiples of σ. For instance, approximately half of the measurements will fall within the range

of $\pm 0.675\sigma$. Only 1 out of 370 measurements will lie outside the $\pm 3\sigma$ boundary, which is a commonly employed threshold.

The range-measurement accuracy is characterized by the rms measurement error, σ_r, given by the root-sum-square of the three error components [31]:

$$\sigma_r = (\sigma_{rN} + \sigma_{rF} + \sigma_{rB})^{1/2} \,, \tag{1.9}$$

where:

- σ_{rN}, the SNR-dependent random range measurement error;
- σ_{rF}, the range fixed random error, the root sum squared of the radar fixed random range error and the random range error from propagation;
- σ_{rB}, range bias error, the root sum squared of the radar range bias error and the range bias error from propagation.

The error in radar range is typically dominated by SNR-dependent factors, and it exhibits a random behavior. This randomness is characterized by a standard deviation, which is given by [31]:

$$\sigma_{rN} = \frac{\Delta R}{\sqrt{2 \cdot SNR}} = \frac{c}{2B\sqrt{2 \cdot SNR}} \,. \tag{1.10}$$

The constrained variability in random ranges could compromise the precision of range measurements, especially with higher signal-to-noise ratios. Typically, internal radar noise yields SNR levels ranging from 25 to 35 dB, leading to random fixed errors σ_{rF} between 1/25th and 1/80th of the range resolution. While propagation-induced random range errors are generally insignificant, they may become pronounced under multipath conditions. Similarly, the angular accuracy can be expressed as function of the signal-to-noise ratio [31]:

$$\sigma_a = \frac{\theta_{BW}}{k_M \sqrt{2 \cdot SNR}} \,, \tag{1.11}$$

where θ_{BW} is the radar beamwidth in the angular coordinate of the measurement, and k_M is the monopulse pattern difference slope, and its values is typically 1.6. Similar to range measurement, fixed angular random errors might constrain angular measurement accuracy, especially with high signal-to-noise ratios. The internal radar noise levels mentioned earlier could result in angular errors ranging from 1/40th to 1/125th of the beamwidth σ_{aF}. This condition is occasionally termed as a maximum beam-splitting ratio ranging from 40 to 125. Random angular errors attributable to propagation tend to be minor in most cases [31].

The error in measuring the cross-range target position in an angular coordinate direction, σ_{cr}, is given by:

$$\sigma_{cr} = R\sigma_a \,. \tag{1.12}$$

For most radars, the cross-range errors that result from angular-measurement errors at useful ranges far exceed the range-measurement errors [31].

1.3 Antenna geometry

The ideal elevation angle of the double-fence setup is mainly determined by the range of the measurements and their correlation. Yet, the radar's accuracy and its capability to track objects in space are linked to the radar parameters, like the antenna's gain and beamwidth, which are influenced by the antenna's design, material, and geometry.

This investigation will concentrate on a setup featuring a one-dimensional array of elements aligned at the feed point of a cylindrical reflector with a parabolic cross-section (Figure 1.2), similar to the configuration employed in the Kiwi Space Radar. The principal distinction here is that a monostatic radar is employed, where both the transmitter and receiver are positioned at the same site.
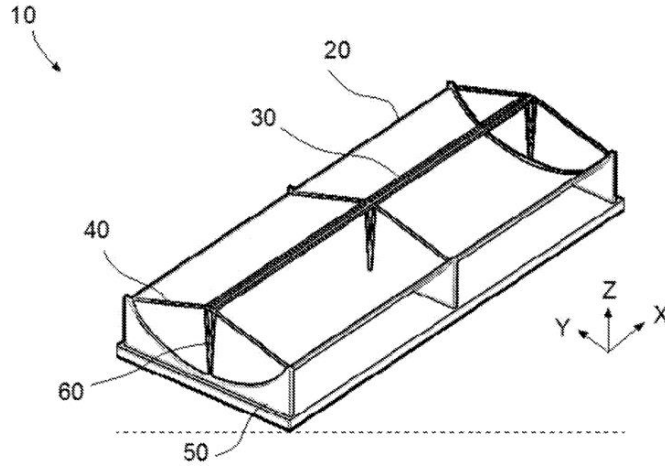
Figure 1.2: 1D phased array antenna system with a parabolic trough reflector [35].

The angle of elevation is determined by the curvature of the parabolic section of the cylinder reflector, a critical factor in concentrating transmission power in the vertical direction, thus determining the beamwidth in that direction. Conversely, for cross-elevation, the length of the linear array is utilized. The phased-array's advantage lies in its capability to electronically sweep the beam almost instantaneously, covering the space in the cross-elevation direction. When the beam of a phased array is deflected away from the broadside direction by an angle φ, its width broadens, and both the array's gain and effective aperture area decrease in relation to the broadside values. This reduction in gain and effective aperture area due to beam scanning is influenced by two main factors [15]:

- The reduction in the projected array area in the direction of the beam, which is given by:

$$G_{phi} = G \cos \varphi .$$

(1.13)

- A further reduction in the gain and effective aperture area of the individual phased-array elements at off-broadside angles. This reduction depends on the element design and is often smaller than the other factor.

The joint effect of these two factors is identified as off-broadside scan loss, which is typically represented as a two-way loss, a product of transmit and receive scan losses [15]:

$$L_s = (\cos \varphi)^{2.5} . \tag{1.14}$$

The antenna gain at the boresight is equivalent to [35]

$$G = \frac{4\pi}{\lambda^2} A_{eff} , \tag{1.15}$$

where λ is the radar wavelength, and A_{eff} is the effective aperture, given by [35]

$$A_{eff} = \varepsilon D_l D_w , \tag{1.16}$$

where D_w is the reflector's width, D_l is the array's length, and ε represents the aperture efficiency. The array length is obtained by multiplying the number of elements by their spacing, which is typically half of the carrier frequency's wavelength. As for the beamwidth, it is generally established at half the power of the beam peak, known as the 3-dB beamwidth. Beamwidths are computed utilizing the antenna's dimensions in their respective planes, as detailed in [15]:

$$x_{BW} \approx \frac{\lambda}{d_x} . \tag{1.17}$$

Therefore, the beamwidth in the elevation direction is approximately λ/D_w, and in the cross-elevation direction is approximately λ/D_l. In this setup, the beamwidth in the latter direction expands as the scan angle deviates from the broadside [15]:

$$\varphi_{BW} = \frac{\lambda}{D_l \cos \varphi} . \tag{1.18}$$

Chapter 2 : Fence bidimensional model

In the initial stages of exploring the optimal elevation angle for the radar fence, the problem is simplified by looking at a two-dimensional scenario, specifically, a circular orbit lying within the plane perpendicular to the space fence bisector is assumed, as shown in Figure 2.1. In order For an orbit to be categorized as a Low Earth Orbit (LEO), its height (h) above Earth must range from 100 to 2000 kilometers [18].

Figure 2.1: Bidimnesional rendering of the KSR, from [21].

To establish a coordinate system that makes sense for this setup, it is used a geocentric coordinate system. Here, the y-axis points from the Earth's surface toward the radar's position on the planet. Importantly, Earth's rotation is not considered in this context, so this coordinate system remains fixed.
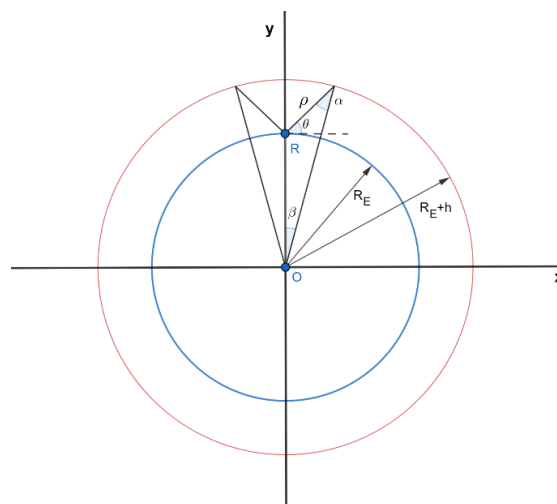
Figure 2.2: 2D model showing the orbit (red), the Earth's surface (blue) and the the radar's location and beams.

2.1   Geometry

In order to solve the model, the initial step involves calculating the distance ρ between an object orbiting at an altitude h and each sensor when the object reaches the center of its beam. This distance is a function of the elevation angle θ of the object, measured from the radar position. Given that both sensors' beams are symmetrical with respect to the y-axis, the distance remains the same for both.

All the angles within the triangle formed by the Earth's center, the sensor position, and the target at the detection point can be calculated. By applying the law of sines to this triangle, it becomes possible to compute the two angles α and then β (Figure 2.2):

$$\frac{R_E}{\sin(\alpha)} = \frac{R_E + h}{\sin(90° + \theta)} \rightarrow \alpha = \operatorname{asin}\left(\frac{R_E}{R_E + h} cos(\theta)\right), \tag{2.1}$$

$$\beta = 90° - \alpha - \theta, \tag{2.2}$$

where R_E is the Earth's radius.

Finally, the distance between the target and the radar (ρ) can be computed:

$$\rho = \sqrt{R_E^2 + (R_E + h)^2 - 2R_E(R_E + h)\cos(\beta)}. \tag{2.3}$$

The distance ρ can be used in the radar equation to compute the power of signal received by the sensor, which decreases with the fourth power of ρ

$$P_r = \frac{P_t G A_e \sigma}{(4\pi)^2 \rho^4}, \tag{2.4}$$

where σ is the radar cross section of the target, which is supposed to be a point scatterer.

The received power is used to obtain the signal-to-noise ratio, which is given by the equation (1.8). The number of pulses coherently integrated depends on the dwell time, which is the duration during which the object remains within the beam. The dwell time is a function of both ρ and the beamwidth θ_{BW}.

To compute the dwell time, the angles β_1 and β_2, as depicted in Figure 2.3, are calculated. This process follows a similar approach to the one used for determining ρ:

$$\begin{cases} \theta_i = \theta \pm \theta_{BW}/2, \\ \alpha_i = \operatorname{asin}[R_E/(R_E + h) \cos\theta_i] \\ \beta_i = 90° - \theta_i - \alpha_i \end{cases} \tag{2.5}$$
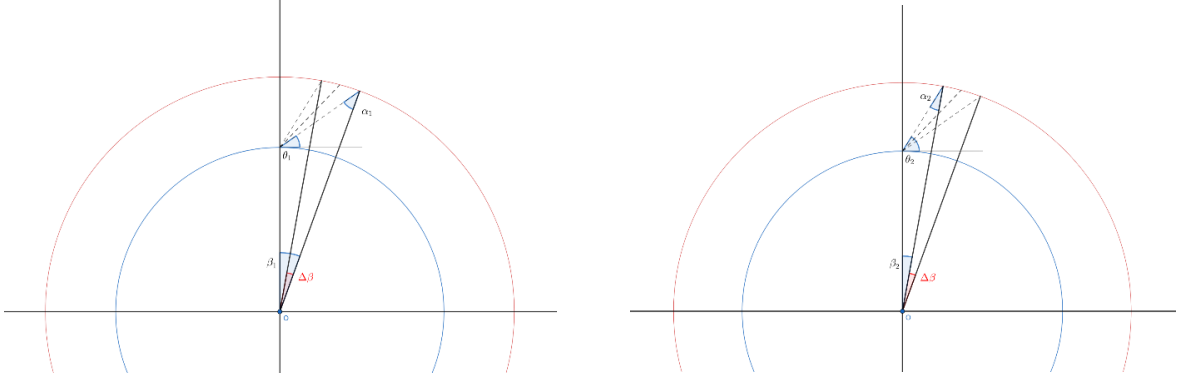
Given that a circular orbit is under consideration, it is important to note that the angular velocity of the object remains constant:

$$\omega = \frac{2\pi}{T} = \sqrt{\frac{GM}{r^3}} \,, \qquad \text{with } r = R_E + h. \tag{2.6}$$

At this stage, the dwell time can be computed, and it is expressed as:

$$t_{dwell} = \frac{\Delta\beta}{\omega} = \frac{\beta_1 - \beta_2}{\omega}. \tag{2.7}$$

In conclusion, the number of pulses reflected by the target within one of the sensor beam is calculated as:

$$M = \frac{t_{dwell}}{PRT} \,, \tag{2.8}$$

where PRT is the pulse repetition period.

2.1   Accuracy of measurements

The signal-to-noise ratio computed in the previous chapter can be used to calculate the standard deviation of the range and cross-range error (σ_r, σ_{cr}) given by the equations (1.10) and (1.12). With these two values the probability distribution of the position measured by a single beam of the radar can be computed and an example is displayed in Figure 2.4.

The disparity in error magnitudes is evident, as shown in Figure 2.4, with the range error demonstrating an approximate reduction by two orders of magnitude compared to the cross-range error. The idea behind employing dual beams rests on the potential to get two measurements from different directions. This dual-measurement approach facilitates the acquisition of uncorrelated data points, consequently culminating in greater accuracy. In the context of a circular orbit assumption, positional information suffices for trajectory determination.
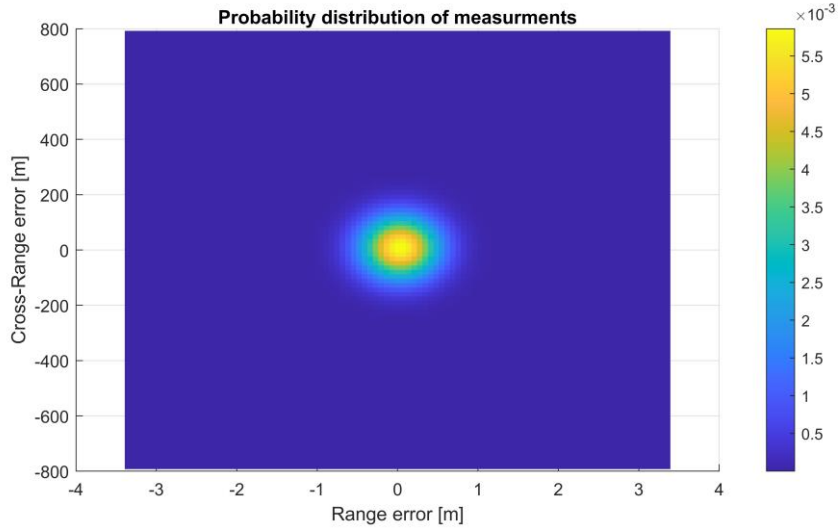
Figure 2.4: Probability distribution of the radar measurement.

The target transits the two beams at distinct instances denoted as t_1 and t_2. As a result, an idea to measure the correlation between the measurements is to temporally propagate the probability distribution of the initial detection to the time of the subsequent measurement. Two reference systems are introduced, each centered on the radar's location. Notably, both systems designate the x-axis to align with the center direction of the respective beams, as displayed in Figure 2.5.
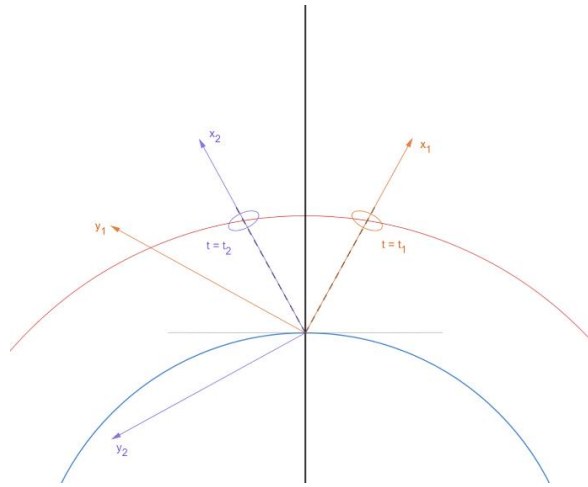
Figure 2.5: Accuracy ellipses regarding the first beam (orange) and second one (blue).

The ellipses portrayed in the figure outline the $\pm 3\sigma$ limits concerning both range, aligned with the x-axis, and cross-range, aligned with the y-axis dimensions. Each point situated within these ellipses carries a specific probability associated with being an outcome of detection. Through the temporal extension of the primary ellipse to t_2, an anticipated region materializes within which the target is likely to reside.

To calculate the propagation, it is sufficient to compute, for each point on the ellipse, the distance to the Earth's center. This distance calculation enables the determination of the angular velocity ω_i (Equation 2.6), which when multiplied by Δt (where $\Delta t = t_2 - t_1$) to compute the angle $\Delta\theta_i$. By applying a rotation around the z-axis for each point, the resulting

shape is referred to as the "propagated ellipse." It is worth noting that, due to variations in orbit altitude among the points on the ellipse, the shape after propagation is not strictly an ellipse. The rotation angle changes for each point, leading to a more complex geometric shape. However, for simplicity, the term "ellipse" is still used to describe this propagated shape.

The propagation corresponds to an emulation of a secondary beam capturing the target's position at t_2, albeit with a divergent orientation.

Consequently, an improvement in the cross-range error materializes. As already mentioned, in scenarios of minimal angular divergence between the two beams, their measurements exhibit strong correlation and resultant enhancement remains modest. Conversely, a reduction in elevation amplifies distance from the object, thereby decreasing the signal-to-noise ratio while increasing the associated uncertainties delineated by the ellipses (Figure 2.6).

The trade-off in this context revolves around two key considerations. In the pursuit of achieving an optimal elevation angle, the analysis does not account for perturbations, and the primary objective is to minimize the overlap between the uncertainty ellipse generated by the second radar beam and the propagated ellipse created by the first one. It is important to note that this approach, while straightforward, does not encompass the entirety of the probability distributions associated with the measurements. To propagate the first ellipse, a crucial series of steps is involved. Firstly, it is necessary to represent all the points on the ellipse in the geocentric reference system. This enables the calculation of the distance between the target measurement and the center of the Earth. With this information, the angular velocity of the target can be determined. By knowing the time taking for the object to move from the first beam to the second, the new position at time t_2 can be computed.

The subsequent step involves converting these propagated positions into the reference system relative to the second radar beam. Finally, with all these preparations completed, it becomes possible to measure the overlapping area between the uncertainty ellipse generated by the second beam and the propagated ellipse from the first one (Figure 2.7).
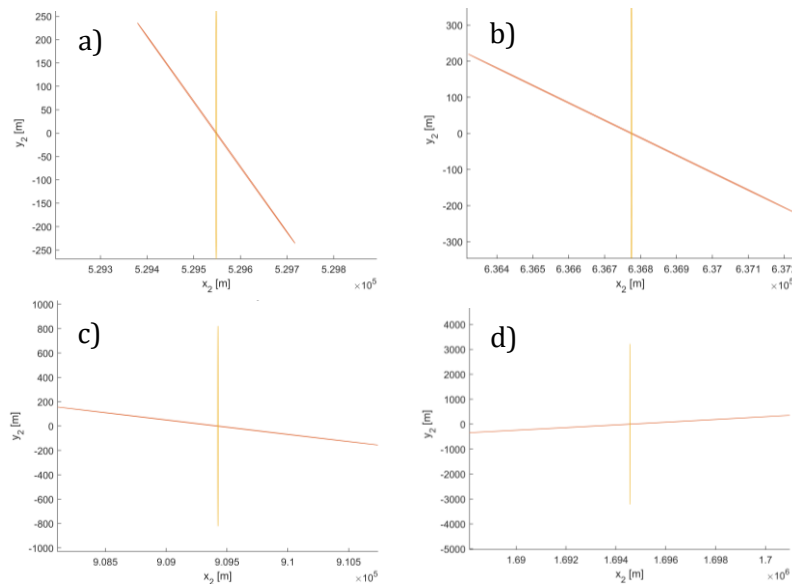
Figure 2.6: 1st beam accuracy ellipse propagated (red) and 2nd beam accuracy ellipse for an elevation angle of 70° (a) ,50° (b) ,30°(c) and 10° (d).
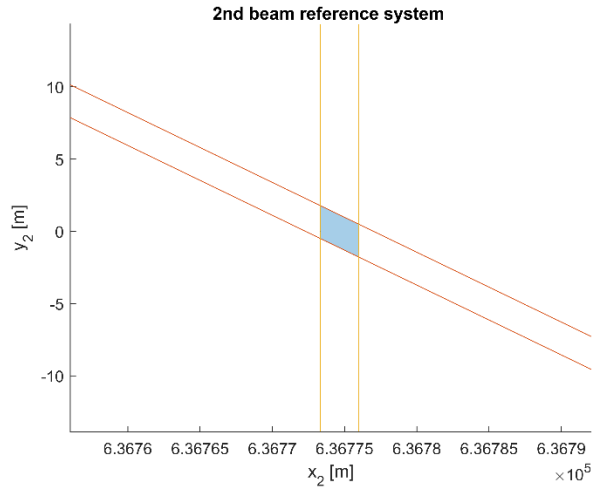
Figure 2.7: Enhanced view of the overlapping area for an elevation angle of 50°.

2.1 Results

To facilitate a meaningful comparison of the results with the Kiwi Space Radar, identical parameters are employed in the analysis:

- central frequency, $f_c = 3$ GHz;
- bandwidth, $B = 10$ MHz;
- power transmitted, $P_t = 50$ kW.

For the antenna gain a value of 63.2 dB is assumed, while concerning the pulse parameters the following values are implemented:

- pulse duration, $\tau = 2$ ms;
- pulse repetition period, $PRF = 60$ Hz.

The first parameter influences the signal-to-noise ratio and the minimum detectable range, while the second one is linked to the range ambiguity.

Simulating object with a radar cross-section of -40dBsm and different radar's elevation angles for different orbit altitudes, it can be seen that the latter parameter influences slightly the optimal elevation angle which leads to a minimum of the intersection area, which oscillates between 54° (Figure 2.8), while the angle used for the KSR is 70°.

The shape of the graph in all four the cases illustrated are quite similar, with a maximum for $\theta = 90°$, where the two ellipses coincide. As the orbit altitude also increases the distance between the radar and the object increases and this leads to a lower SNR, which influences the accuracy. In fact, even though the optimal angle does not change significantly, the ellipses get bigger and therefore so does the overlapping area.

14
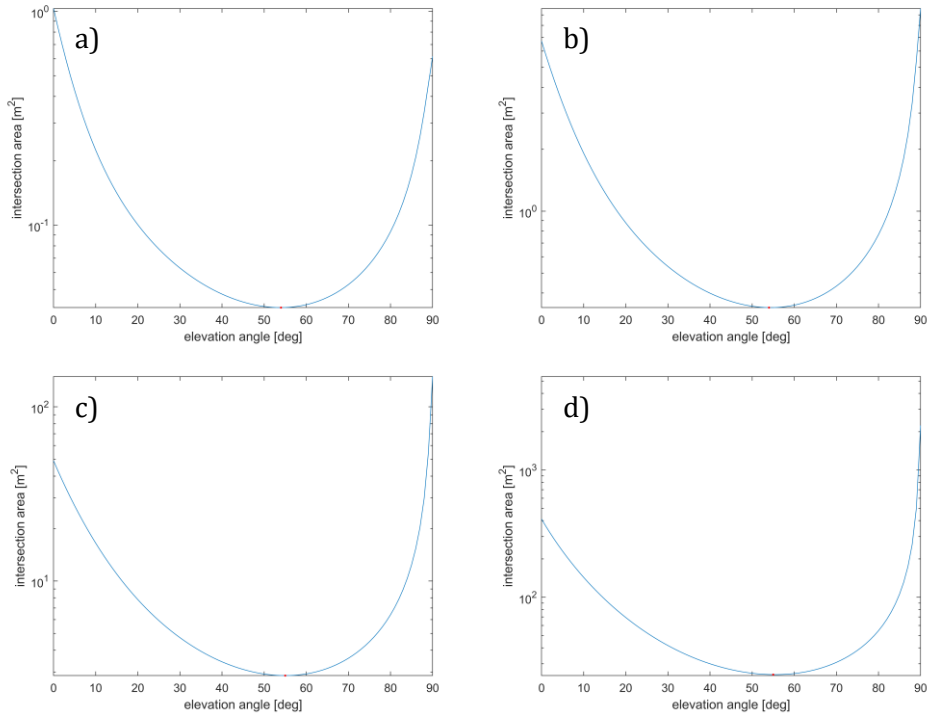
*Figure 2.8: : Ellipses overlapping area as function of elevation angle
for an orbit altitude of (a) 250 km, (b) 500 km, (c) 1000 km, (d) 2000 km.*

2.1   Approximation

As previously discussed, the propagation process does not perfectly preserve the ellipse shape due to variations in the angular velocity of each point. Nevertheless, it is observed that the angular velocity does not change significantly, especially for higher elevation angles. In such cases, the difference between the highest and lowest points on the ellipse is primarily influenced by the range error, which tends to be relatively small. In the scenario where the elevation angle is 90 degrees, the disparity in altitude is precisely equivalent to the length of the ellipse's minor axis, which amounts to $6\sigma_r$.

Conversely, for lower elevation angles, the cross-range dimension, which is significantly larger than the range error, becomes the dominant factor. Given the identification of an optimal elevation angle of around 56 degrees, a potential simplification arises: applying the same rotation angle to each point on the first ellipse. This angle is determined by the precise intersection points with the field of view and the Earth's center, namely is equal to two times the angle β shown in Figure 2.9.
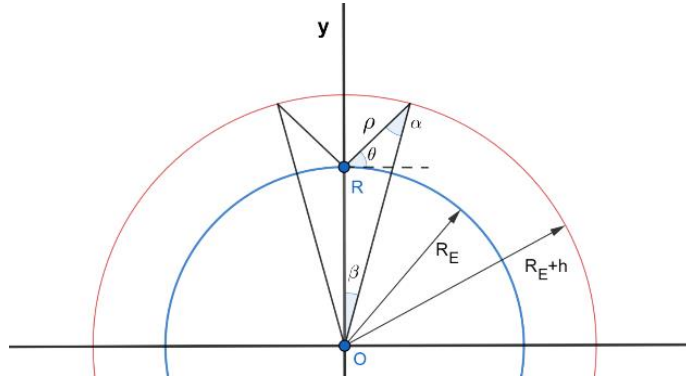
Figure 2.9: 2D model showing the orbit (red), the Earth's surface (blue).

The results, as illustrated in Figure 2.10, validate the small error introduced by this approximation for higher elevation angles. Additionally, it can be observed that the discrepancy between the exact and approximated cases diminishes with increasing altitudes.

While this simplification may not significantly reduce the computational time required to solve the model, it proves valuable in preparing for the 3D analysis.
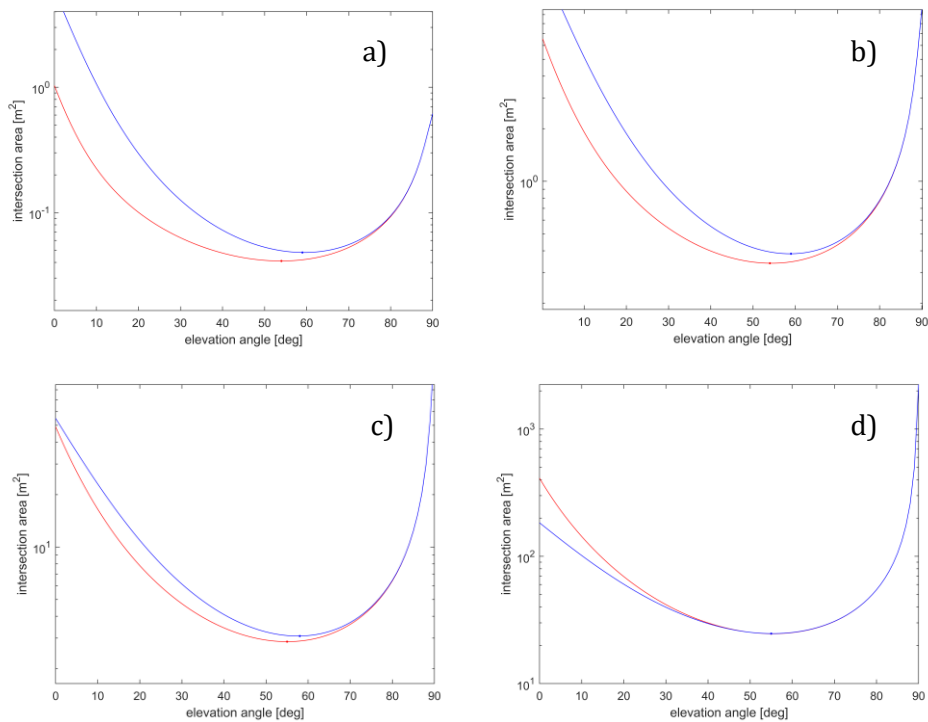
Figure 2.10: Comparison between the exact case (red) and the approximate one (blue).

16

2.5   Model limitations

The model under consideration is deliberately simplified and lacks incorporation of several pertinent factors:

- Probability distribution: the portrayal presented does not integrate the inherent probability distribution associated with Gaussian characteristics. The ellipses depicted, while indicative of a certain level of uncertainty, omit the probabilistic nature of measurement outcomes governed by Gaussian distributions.
- Orbital eccentricity and three-dimensionality: the model fails to account for the eccentricity intrinsic to actual orbital trajectories. By simplifying to a circular orbit, the nuanced three-dimensional nature of orbits is disregarded, thereby omitting variations in altitude, inclination, and orbital shape that typify real-world scenarios.
- Earth's rotation: The model's static depiction refrains from consideration of the Earth's rotational motion. The consequential dynamic aspects like the change in radar-target geometry due to Earth's rotation during measurement intervals are absent from this portrayal.

To comprehensively address the complexities of the system being studied, future iterations of the model should integrate these aspects, acknowledging the probabilistic nature of measurements, accommodating orbital eccentricity and three-dimensionality, and accommodating the dynamic impact of Earth's rotation on the measurement process.

Chapter 3 : Fence three-dimensional model

The next step in this analysis is to extend the previous model into a three-dimensional orbit. In practical situations, radar may not always be situated within the orbital plane, and the orbit may possess specific characteristics such as inclination and eccentricity.

In this 3D scenario, two uncertainties impact the cross-range measurements, and they are assumed to be identical. Consequently, the uncertainty ellipse transforms into an ellipsoid (error in range, and two angular directions). As previously mentioned, the measurement from the first beam is highly likely to fall within the $\pm 3\sigma$ ellipsoid. By propagating the points within this ellipsoid, it becomes possible to simulate a secondary beam that captures the target's position at t_2, although with a divergent orientation.

Nonetheless, as discussed earlier in the introduction, a single measurement is insufficient to determine the orbit. Therefore, orbit propagation, as implemented in the 2D model, is no longer feasible. However, by assuming a circular orbit, which is a reasonable assumption as many objects follow this type of orbit, a single radar measurement provides adequate information. In cases of circular orbits, eccentricity is zero, and the argument of perigee holds no significance because the object maintains a constant distance from the Earth's center. In this context, information about the range ratio obtained from the Doppler effect is necessary to determine the orbital plane.

However, this approach introduces significantly higher complexity and computational demands because errors affect the range rate, resulting in a 4-dimensional ellipsoid. To simplify the problem, a similar approximation to the one employed in the 2D case is applied. The first uncertainty ellipsoid is rotated around the axis perpendicular to the orbit plane, using the angle formed by the two target position vectors when they intersect both field-of-view boundaries.
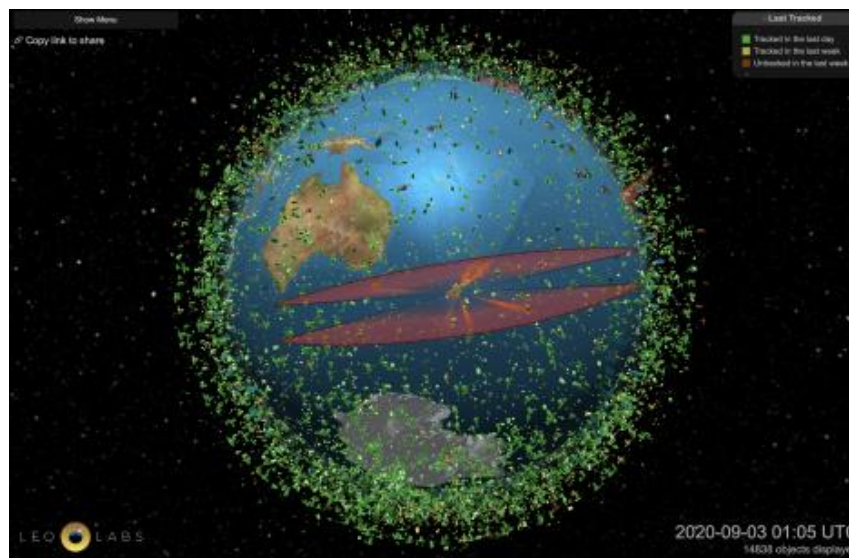
Figure 3.1: FOR of the KSR, from [21].

3.1 Geometry

Just as in the previous model, the initial step involves calculating the distances ρ_1 and ρ_2 between the object and the radar when the radar intersects both sensors field of regard. However, in this case, these distances are not equal due to the orbit not being perpendicular to the field of view. Instead, the field of view is described by a plane, as depicted in Figure 3.1.

For this analysis, two coordinate systems are considered. The first is the geocentric coordinate system, with the x and y-axes situated in the equatorial plane and the x-axis oriented towards the Vernal Equinox. The second reference system (x', y', z') has the x-axis directed towards the ascending node, which is the point where the orbital plane intersects the equatorial plane, and the y-axis situated within the orbital plane. The center of both systems coincides and transforming between these coordinates entails applying rotations. For this reason, it is necessary to define the rotation matrices:

$$\boldsymbol{R_x}(t) = \begin{bmatrix} 1 & 0 & 0 \\ 0 & \cos t & -\sin t \\ 0 & \sin t & \cos t \end{bmatrix}, \tag{3.1}$$

$$\boldsymbol{R_y}(t) = \begin{bmatrix} \cos t & 0 & \sin t \\ 0 & 1 & 0 \\ -\sin t & 0 & \cos t \end{bmatrix}, \tag{3.2}$$

$$\boldsymbol{R_z}(t) = \begin{bmatrix} \cos t & -\sin t & 0 \\ \sin t & \cos t & 0 \\ 0 & 0 & 1 \end{bmatrix}. \tag{3.3}$$

A vector represented in the orbital coordinate system can be transformed into the equatorial coordinate system by multiplying it with the following rotation matrix:

$$\boldsymbol{R} = \boldsymbol{R_z}(\Omega)\boldsymbol{R_x}(i), \tag{3.4}$$

Where i represents the orbit inclination, and Ω denotes the right ascension of the ascending node (RAAN). The inverse transformation can be achieved by taking the inverse of this matrix:

$$\boldsymbol{R_2} = \boldsymbol{R}^{-1} = \boldsymbol{R_x}(-i)\boldsymbol{R_z}(-\Omega). \tag{3.5}$$

The latter transformation is particularly valuable for identifying the points on the orbit where the radar observes the target. In fact, expressing the analytical trajectory in three dimensions becomes simpler when it is represented in the orbital system, where the z-component is consistently 0.

To determine the intersection, it is also necessary to express the FOR plane in this reference system. The first step in this process involves deriving the analytical expressions for the two planes. For the sake of simplicity, the radar is positioned on the equatorial plane, with the following coordinates:

$$\overrightarrow{r_R} = [0, R_E, 0]^T, \tag{3.6}$$

where R_E is the Earth radius. The general formula for a plane is:

$$ax + by + cz + d = 0 \,, \tag{3.7}$$

where $[a, b, c]$ represents the vector normal to the plane. To derive the plane equation that describes the FOR, a plane with the same inclination can be considered, passing through the center of the Earth. In the equatorial reference system, this plane contains the unit vector in the z-direction $\vec{u}_z$, and for the first beam, a second vector which depends on the elevation θ. The cross product of these two vectors yields the normal vector (n_1). Therefore, the plane equation is given by:

$$n_{1,x}x + n_{1,y}y + n_{1,z}z = 0 \,, \tag{3.8}$$

the constant term in the plane equation is 0 because the plane passes through the origin. Finally, by applying the following translation the FOR plane is positioned through the radar location:

$$\begin{cases} x \to x - r_{R,x} \\ y \to y - r_{R,y} \\ z \to z - r_{R,z} \end{cases} \tag{3.9}$$

where the only non-zero component of the vector $\vec{r_R}$ is the on in the y direction.
Figure 3.2 illustrates the original plane, obtained using the red vectors, alongside the translated plane that represents the FOV of the first portion of the radar, situated along the y-axis.
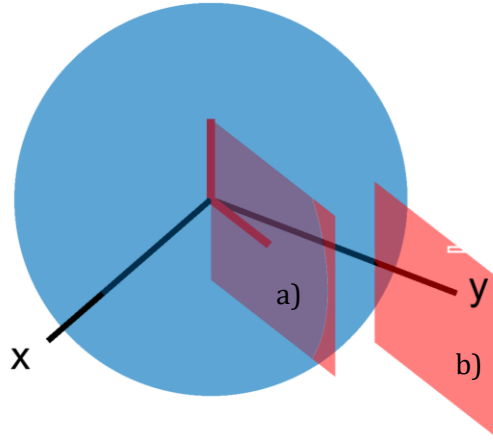
Figure 3.2: Plane generated using the unit vectors $\vec{u_z}$ and $\vec{n_2}$ (a) and radar FOR (b).

The final equation, in the equatorial system, is as follows:

$$n_{1,x}x + n_{1,y}y + n_{1,z}z - n_{1,y}R_E = 0 \,, \tag{3.11}$$

or, in its explicit form:

$$x = h_1 y + h_2 z + h_3 \,, \tag{3.12}$$

with

$$h_1 = -\frac{n_{1,y}}{n_{1,x}} \,, \qquad h_2 = -\frac{n_{1,z}}{n_{1,x}} \,, \qquad h_3 = \frac{n_{1,y}R_E}{n_{1,x}} \,. \tag{3.13}$$

A similar procedure can be applied to compute the equation for the second FOV. However, in this case, the normal vector is defined as:

$$\vec{n_2} = [0, 0, 1] \times [\cos(\theta), \sin(\theta), 0] . \tag{3.14}$$

The sensor is not capable of detecting all objects crossing the FOR plane. Therefore, a minimum elevation angle within the Field of View and a maximum orbit altitude can be defined. This allows for the creation of a visualization similar to the renderings displayed on the LeoLabs website (Figure 3.3).
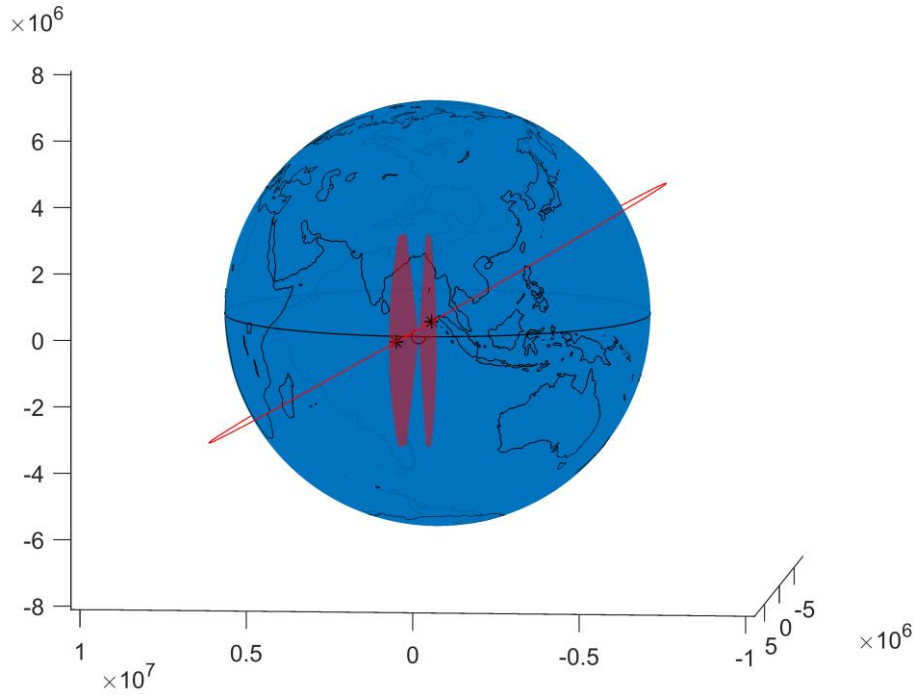
Figure 3.3: Orbit and radar FOR in the equatorial reference frame.

Utilizing the relationship between equatorial (x, y, z) and orbital coordinates (x', y', z'), the plane equation in the second reference system can be derived as follows:

$$\vec{r} = \boldsymbol{R}\,\vec{r}' \rightarrow \begin{cases} x = R_{11}x' + R_{12}y' + R_{13}z' \\ y = R_{21}x' + R_{22}y' + R_{23}z' \\ z = R_{31}x' + R_{32}y' + R_{33}z' \end{cases}, \tag{3.15}$$

$$x' = h_1'y' + h_2'z' + h_3' . \tag{3.16}$$

Given the assumption of a circular orbit, its equation in the orbital reference frame can be expressed as:

$$\begin{cases} x'^2 + y'^2 = a^2 \\ z' = 0 \end{cases}, \tag{3.17}$$

where a is the orbit radius.

Figure 3.4 shows the FOV and the orbit in the orbital reference system. As expected, the orbit lies within the x'-y' plane.

To determine the intersection between the orbit and the plane, it is sufficient to solve the following system of equations:

$$\begin{cases} x' = h'_1 y' + h'_2 z' + h'_3 \\ \quad x'^2 + y'^2 = a^2 \\ \quad\quad z' = 0 \end{cases}.$$

(3.18)

This system of equations has two solutions. One solution corresponds to the point of interest where the radar observes the object, while the other solution is on the opposite side of the Earth.
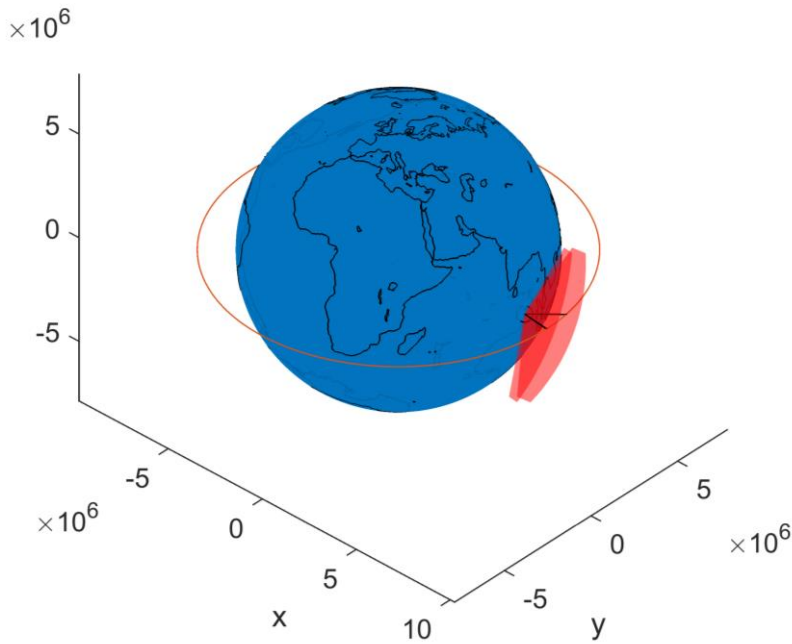
Figure 3.4: Orbit and radar FOR in the orbital reference frame.

3.2   Accuracy of measurements

The subsequent calculations will be performed in reference to the orbital coordinate system, with the apex omitted for clarity.

After obtaining the coordinates of the two intersection points, it is possible to calculate the distance between the radar and the object when it crosses the radar's Field of View:

$$\vec{\rho}_{1,2} = \vec{r}_{1,2} - \vec{r}_R,$$

(3.19)

Where $\vec{\rho}$ represents the vector connecting the radar and the target, and $\vec{r}$ is the vector identifying the target in the orbital reference frame (Figure 3.5). Using ρ, it is possible to calculate the signal-to-noise ratio required to define the ellipsoid, with one semimajor axis equal to $3\sigma_r$ and the others equal to $3\sigma_{cr}$.
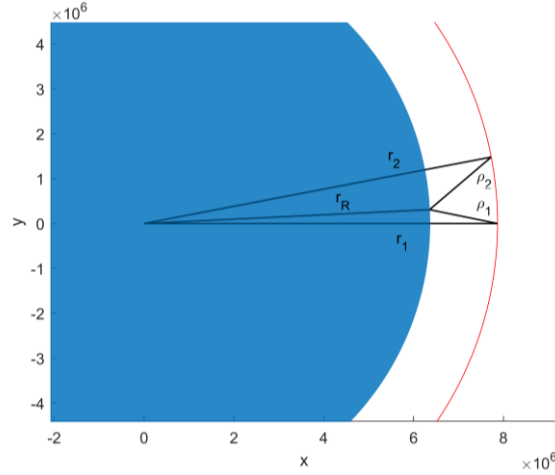
Figure 3.5: Radar and target position vectors in the orbital reference frame.

Nonetheless, in order to compute the signal-to-noise ratio it is imperative to calculate the time spent by the object inside both beams, thereby determining M_1 and M_2, which represent the number of pulses coherently integrated to enhance the SNR. To accomplish this, two additional planes must be defined, inclined of $\pm\,\theta_{BW}/2$ with respect the FOR plane described before (**Error! Reference source not found.**). The intersections of the orbit with these planes will p rovide the positions where the target enters and exits the beam. With this information, the dwell time can be computed, consequently yielding the parameter M. Once again, it is assumed that the gain inside the beam remains constant.
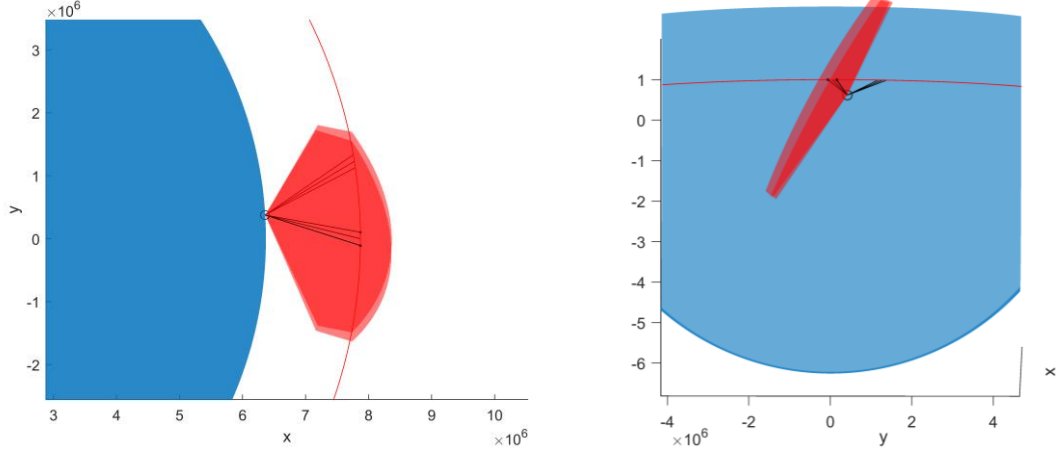
Figure 3.6: FOR of the first sensor.

Unlike the 2D case, the sizes of the ellipsoids are different because ρ_1 and ρ_2 are generally not equal.

The coordinates of the ellipsoids can be expressed in quadratic notation as follows [4]:

$$(\vec{r} - \vec{r_c})^T \boldsymbol{D A D^T} (\vec{r} - \vec{r_c})^T = 1 \,. \tag{3.20}$$

In this equation, $\vec{r_c}$ represents the ellipsoid center, $\boldsymbol{A}$ is a diagonal matrix containing the squared inverses of the semimajor axes, and $\boldsymbol{D}$ is an orthogonal matrix describing the orientation of the ellipsoid's axes. For this specific case, $\vec{r_c}$ is equal to $\vec{r_1}$ for the first ellipsoid and $\vec{r_2}$ for the second one. $\boldsymbol{D}$ is a function of $\vec{\rho}$, while A is given by:

$$A = \begin{bmatrix} \dfrac{1}{9\sigma_R^2} & 0 & 0 \\[2mm] 0 & \dfrac{1}{9\sigma_{CR}^2} & 0 \\[2mm] 0 & 0 & \dfrac{1}{9\sigma_{CR}^2} \end{bmatrix}, \tag{3.21}$$

while the rotation matrix D is given by two consecutive rotations around y and z-axis:

$$D = R_y(\alpha)R_z(\beta), \quad \alpha = -\left(\frac{\pi}{2} + \tan^{-1}\frac{\rho_y}{\rho_x}\right), \quad \beta = \tan^{-1}\frac{\rho_z}{\sqrt{\rho_x^2 + \rho_y^2}}. \tag{3.22}$$

3.3 Approximation

As previously mentioned, a similar simplification to the one used in the 2-dimensional case is now applied. To simulate the propagation of the points inside the first ellipsoid, a rotation around the z-axis (perpendicular to the orbital plane) is employed (Figure 3.7). Calculating the rotation angle is straightforward; it involves computing the angles formed by the target positions at times t_1 and t_2 with respect to the x-axis:

$$v_{1,2} = \operatorname{atan}\left(\frac{y_{1,2}}{x_{1,2}}\right), \quad \Delta v = v_2 - v_1, \tag{3.23}$$

with $y_{1,2}$ and $x_{1,2}$ the components of the vectors $\vec{r}_{1,2}$.

After applying the rotation $R_z(\Delta v)$ to each point of the first ellipsoid, the last step involves determining the overlapping volume between the second ellipsoid and the propagated one. Analytically solving this problem is quite challenging, so a numerical method is implemented. Specifically, a sufficiently large number, N_1, of random points inside the propagated ellipsoid are generated randomly. Then, it is verified whether these points also fall within the ellipsoid associated with the second beam or not (Figure 3.8). If they do, they will satisfy the following relation [4]:

$$(\vec{r} - \vec{r_2})^T D_2 A_2 D_2^T (\vec{r} - \vec{r_2})^T \leq 1, \tag{3.24}$$

where $\vec{r}$ contains the coordinates of a generic point.

The formula used to approximate the overlapping volume is as follows:

$$V = V_1 \frac{N_{12}}{N_1} = \frac{4}{3}\pi(3\sigma_{R1})(3\sigma_{CR1})^2 \frac{N_{12}}{N_1}. \tag{3.25}$$

Here, V_1 represents the volume of the first ellipsoid, which remains constant even after the rotation, and N_{12} is the number of points falling within both ellipsoids.
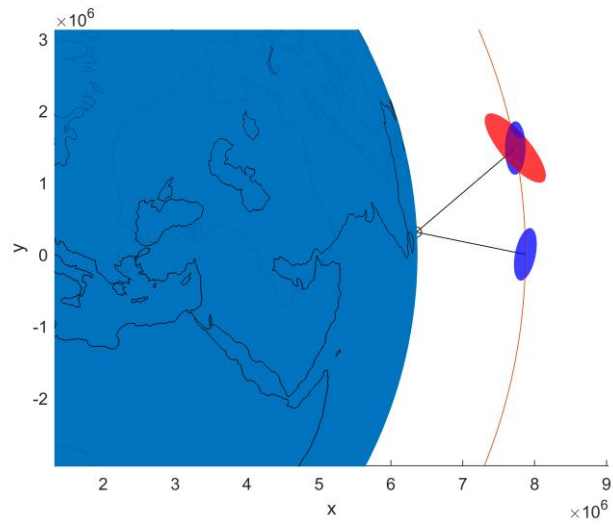
Figure 3.7: Accuracy ellipsoids related to the first beam (blue), with its propagation, and to the second one (red).
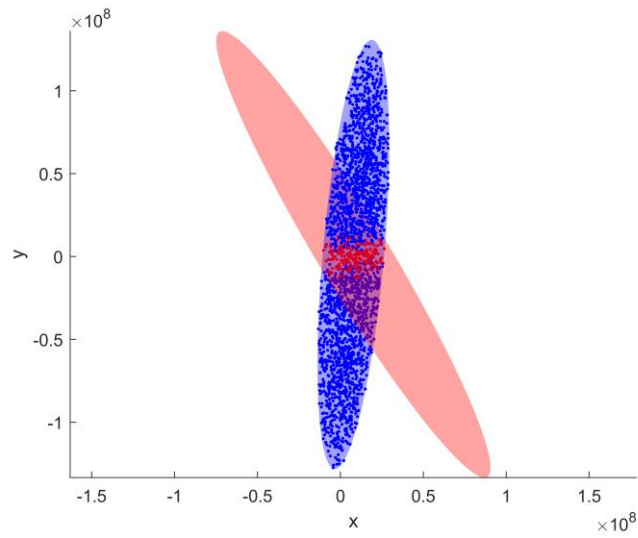
Figure 3.8: Enhanced view of the overlapping volume of the two ellipsoids.

3.4 Probability distribution

The decision to impose a rotation on the first ellipsoid yielded a significant simplification of the probability distribution function for measurements. A straightforward rotation not only maintains the ellipsoid's shape but also the Gaussian distribution, whose equation expressed in the matrix notation in the n-dimensional space closely resembles the ellipsoid's equation [8]:

$$p(\vec{x}; \vec{\mu}, \boldsymbol{\Sigma}) = \frac{1}{(2\pi)^{\frac{n}{2}} |\boldsymbol{\Sigma}|^{1/2}} \exp\left(-\frac{1}{2}(\vec{x} - \vec{\mu})\boldsymbol{\Sigma}^{-1}(\vec{x} - \vec{\mu})\right), \quad (3.26)$$

where $\vec{\mu} \in \boldsymbol{R}^n$ is the mean vector and $\boldsymbol{\Sigma} \in \boldsymbol{R}^{n,n}$ the covariance matrix.
In this scenario, the dimension is 3, reflecting the target's position measurement. The mean vector represents the true target position, while the covariance matrix should consider not only the accuracy of the measurements in range, elevation, and cross-elevation (which make up the standard deviation in the principal directions) but also the orientation of these directions with respect to the reference system adopted, which in this case is the orbital one. To model this accurately, the same approach used for the ellipsoid is adopted, given that the main axes of the ellipsoid coincide with those of the normal distribution. However, the $\boldsymbol{A}$ matrix is replaced by the matrix $\boldsymbol{C}$, containing the squared standard deviation of the measurements.

$$\boldsymbol{\Sigma} = \boldsymbol{DCD^T}. \quad (3.27)$$

The first PDF is further rotated around the z-axis to approximate the propagation of the initial detection. Utilizing probability distribution functions confers an advantage: the final PDF describing the target's position at the time of the second detection, combining both measurements, is simply the multiplication of the individual distributions. If the ranges at the two detection points are equal, the determinants of the covariance matrices are also equal, resulting in the following equation to describe the distribution:

$$p_f = p_1 p_2 = \frac{1}{(2\pi)^3 |\boldsymbol{\Sigma_1}|} \exp\left(-\frac{1}{2}(\vec{x} - \vec{\mu})\boldsymbol{\Sigma_1^{-1}}\boldsymbol{\Sigma_2^{-1}}(\vec{x} - \vec{\mu})\right). \quad (3.28)$$

This situation arises when the ascending node precisely divides the two fields of regard. The final distribution's shape is nearly Gaussian, albeit not perfectly, owing to the coefficient that deviates from the Gaussian norm. Despite this, a covariance matrix can be derived from the Equation (3.28):

$$\boldsymbol{\Sigma}_f = \left(\boldsymbol{\Sigma_1^{-1}}\boldsymbol{\Sigma_2^{-1}}\right)^{-1}, \quad (3.29)$$

The standard deviation along the principal axes can be calculated by computing the eigenvalues of $\boldsymbol{\Sigma}_f$. This information enables one to compute the volume of the 3σ ellipsoid for the final distribution with ease.
In Figure 3.9, an example of a three-dimensional Gaussian distribution is visualized using a scatter plot, with point color and size varying based on the probability density. The product of

the two PDFs is depicted in Figure 3.10, highlighting an enhanced accuracy in the y-direction attributable to the uncorrelation of the two measurements.

Normalized PDFs
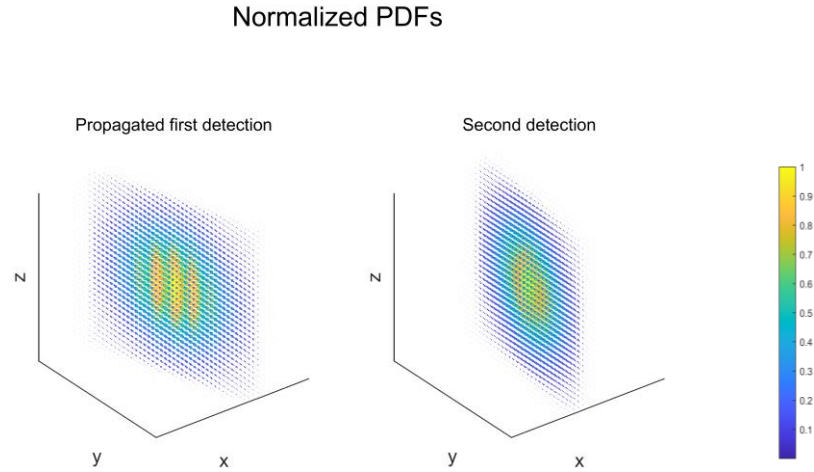
Figure 3.9: PDFs of the propagated first detection and of the second detection, with $i = 50°$.
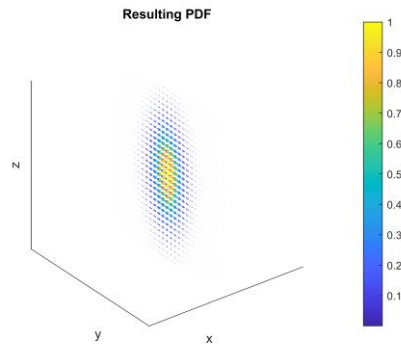
Figure 3.10: Resulting PDF given by the product of the two distributions depicted in Figure 20.

This analytical approach offers two primary benefits. Firstly, it significantly reduces computational expenses compared to the Monte Carlo method, which often necessitates generating a vast number of points to attain precision. In contrast, this approach involves merely calculating the inverse matrices and the eigenvalues of the square root of the final covariance matrix. Secondly, this method does not account for the probability density within the ellipsoids when determining the overlapping volume.

3.5 Results

As done previously in the two-dimensional case, the search for the optimal elevation angle continues in this scenario. However, here the goal is not to minimize the area but rather the overlapping volume. Additionally, it is possible to explore various orbits, although it was demonstrated in the previous chapter that the approximation works well for high orbits. Therefore, the focus is on circular orbits with a radius of 2000 km [18], which represents the upper limit for Low Earth Orbit (LEO).

In this initial phase, the right ascension of the ascending node (Ω) is kept constant at 90 degrees. This configuration ensures that the intersection between the orbital plane and the equatorial plane is equidistant from the two radar beams (Figure 3.11). The only parameter that varies is the orbit's inclination. This specific choice of Ω results in ellipsoids of equal size since the detection points are equidistant from the radar.
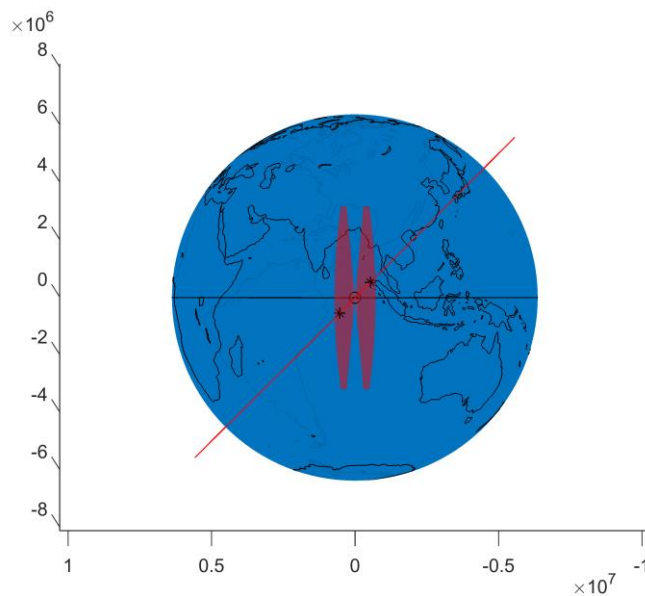
Figure 3.11: FOR and orbit in the equatorial coordinate system.

However, altering the inclination leads to a change in the portion of the orbit traversed between the two detections. A higher inclination results in a larger portion of the orbit being covered, leading to a lower correlation between the two measurements. Consequently, the optimal point is expected to be at a higher elevation angle in this case.

These findings are partially supported by the graph in Figure 3.12, where, except for the case with a 20-degree inclination, the optimal elevation angle increases with the inclination. The peculiar nature of the case depicted in Figure 3.12-b may be related to the approximation error made in estimating the overlapping volume. Despite employing a substantial number of points in the numerical method (about 10^6), the overlapping volume remains relatively insignificant compared to the volume of the ellipsoids, especially at low elevation angles. Consequently, the graphs presented in Figure 3.12 have been smoothed to mitigate noise, introduced by the numerical method.

Furthermore, it is worth noting that for higher inclinations, the flat zone near the minimum point diminishes. This occurs because a slight increase in elevation angles in such cases leads to significant distances between the radar and the object at the detection points.

Figure 3.13 provides a visual representation of the optimal elevation angle for various inclinations. The linear regression curve, showed in Figure 3.13, supports the previously discussed behavior. It is important to note that, for this plot, only inclinations up to 60 degrees have been included, as there is a risk that the target may not intersect the radar field of regard for higher inclinations. Within this range, the linear regression indicates an average value of approximately 68 degrees. This value is notably close to the 70 degrees utilized for the Kiwi Space Radar.
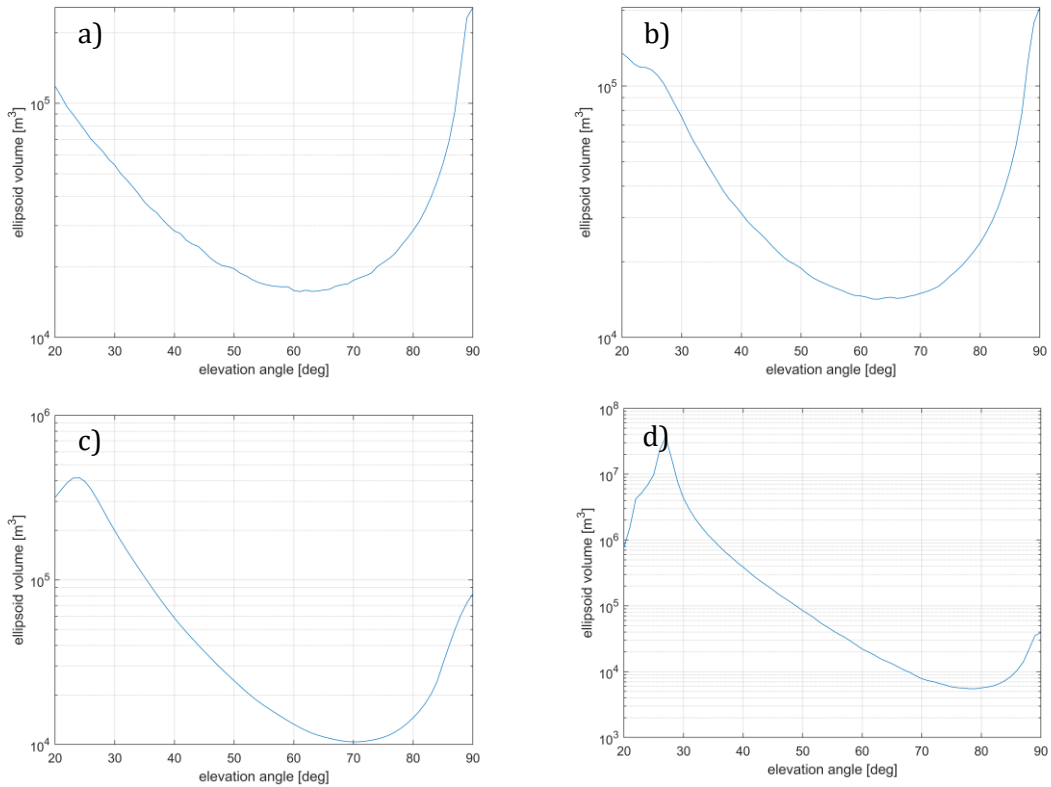
Figure 3.12: Overlapping volume as function of the elevation angle
for different orbit inclination: 0° (a), 20° (b), 40° (c), 60° (d).
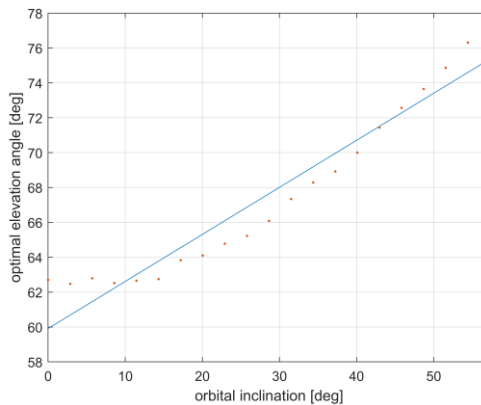
Figure 3.13: Optimal elevation angle as function of the orbital inclination.

Utilizing probability distributions, rather than solely considering the overlapping volume of the two accuracy ellipsoids, yields comparable plots (Figure 3.14). These plots demonstrate a similar profile, with the optimal elevation increasing with inclination. Notably, the most significant disparity lies in the region of low elevations, where accuracy degrades quickly.
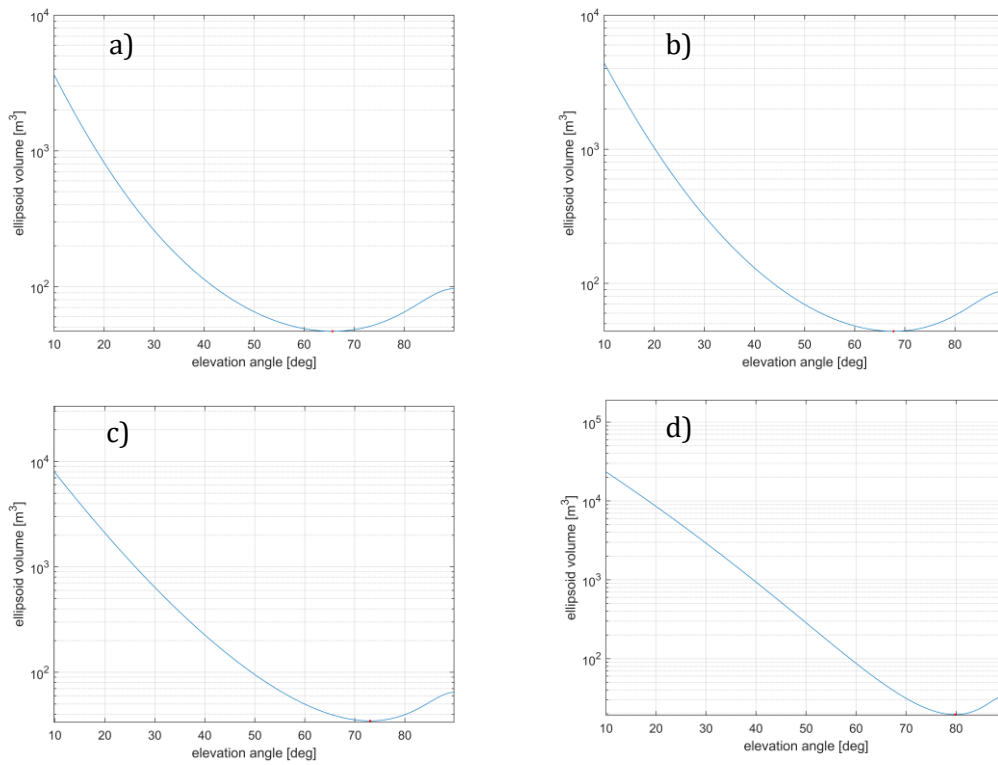
Figure 3.14: Accuracy ellipsoid volume as function of the elevation angle
for different orbit inclination: 0° (a), 20° (b), 40° (c), 60° (d).

Finally, Figure 3.15 compares the optimal elevation profiles as a function of the orbital inclination using the two methods. The outcomes are as expected, showing similar behaviors in the optimal elevation region. However, the overlapping volumes method displays noise in the results, attributed to inaccuracies introduced by the Monte Carlo method.
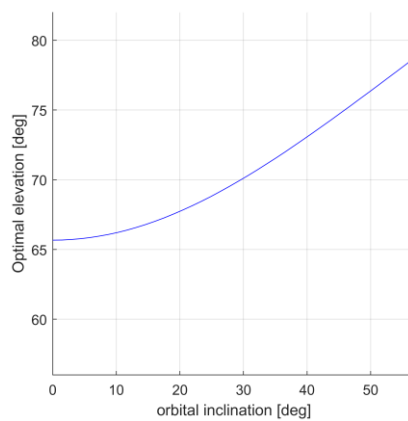
Figure 3.15: Optimal elevation angle as function of the orbital inclination.

31

Chapter 4 : Orbit determination

The previous chapters offer valuable insights and results regarding the selection of an optimal elevation for the two fields of regard, they are subject to significant simplifications. One notable simplification is the assumption of a circular orbit, which is reasonable in the context of Low Earth Orbit (LEO) due to atmospheric drag tending to circularize orbits in this region. However, a more substantial simplification arises when considering the propagation of the first detection to the time of the second one.

Applying the same rotation to the entire ellipsoid or covariance matrix would only be feasible with exact knowledge of the orbital plane. However, this information is typically unavailable with just one radar measurement. Consequently, this reasoning is valid primarily for cataloged objects or when there is sufficient dwell time inside the radar beam to enable multiple detections, which can provide information about the orbital plane.

In the general case, an uncatalogued object may cross one of the two fences and produce only a single detection. From this observation alone, orbital propagation cannot be accurately executed. At least one more detection from the second fence is required to determine the target orbit. This chapter delves into studying this scenario, aiming to calculate an optimal elevation as a function of the accuracy of orbit determination provided by the two measurements.

4.1   Keplerian elements

Orbital elements are parameters that can uniquely characterize a specific orbit (Figure 4.1), particularly in celestial mechanics when dealing with Kepler orbits in two-body systems.

Shape and size are defined by two key elements:

- Eccentricity (e): This determines the shape of the ellipse and describes how elongated it is compared to a circle (not depicted in the diagram).
- Semi-major axis (a): Calculated as the average of the periapsis and apoapsis distances, this element specifies the overall size of the ellipse.

The orbital plane's orientation is determined by the following elements:

- Inclination (i): This indicates the tilt of the ellipse with respect to the reference plane, measured at the ascending node (the point where the orbit intersects the reference plane from below, marked as the green angle i in the diagram). The tilt angle is measured perpendicular to the line of intersection between the orbital plane and the reference plane.
- Longitude of the ascending node (Ω): This orients the ascending node of the ellipse (the point where the orbit passes from south to north through the reference plane, symbolized by ♈) with respect to the reference frame's vernal point.

The remaining elements are as follows:

- Argument of periapsis (ω): This specifies the orientation of the ellipse within the orbital plane as an angle measured from the ascending node to the periapsis (the point nearest to the primary object around which the orbiting body revolves).
- True anomaly (ν) at epoch (t_0): This defines the position of the orbiting body along the ellipse at a specific time (the "epoch").
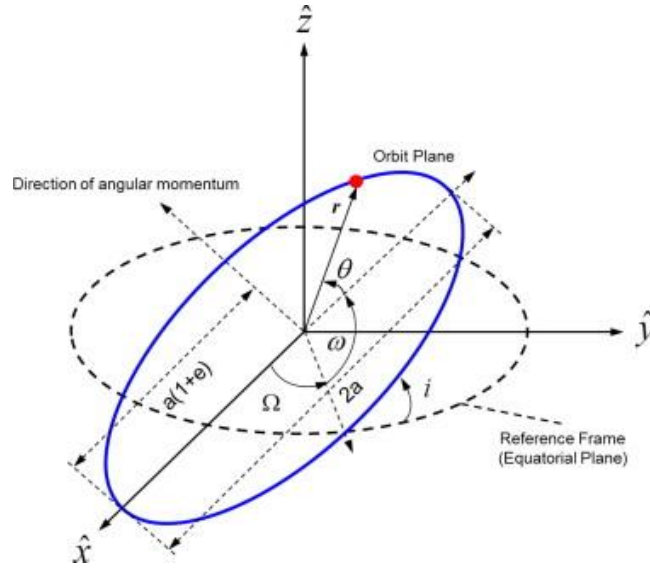
Figure 4.1: Earth-centered inertial (ECI) coordinate frames and Keplerian elements [32].

The mean anomaly serves as a mathematically convenient, but non-geometric, parameter that linearly varies with time. It can be converted into the true anomaly (ν) which corresponds to the geometric angle within the plane of the ellipse, extending from periapsis (the closest point to the central body) to the orbiting object's position at any given time.

The standard reference frame used is an Earth-centered inertial (ECI) coordinate frame, with its origin situated at Earth's center of mass. ECI coordinates remain fixed relative to the stars and do not rotate. In the current coordinate system, the x-axis aligns with the mean Vernal Equinox, while the z-axis aligns with Earth's rotation axis. The y-axis is rotated by 90° East relative to the celestial equator.

A secondary coordinate system can be defined based on the object's orbital path. In this newly established system, denoted as (x_o, y_o, z_o), the x-axis points toward the orbit's perigee, the z-axis is perpendicular to the orbit's plane, and the y-axis is perpendicular to both the x and z-axes. To transform a generic vector $\vec{r}_o$ from the orbital frame (depicted in red in Figure 4.2) to the Earth-centered inertial (ECI) frame (depicted in black), a sequence of rotations must be applied as follows:

$$\vec{r}' = \boldsymbol{R_z}(-\omega)\vec{r}_o,$$

$$\vec{r}'' = \boldsymbol{R_x}(-i)\,\boldsymbol{R_z}(-\omega)\vec{r}_o, \qquad\qquad (4.1)$$

$$\vec{r} = \boldsymbol{R_z}(-\Omega)\boldsymbol{R_x}(-i)\,\boldsymbol{R_z}(-\omega)\vec{r}_o,$$

where $\boldsymbol{R_1}$, $\boldsymbol{R_2}$ and $\boldsymbol{R_3}$ are the rotation matrices around respectively the x, y, and z axis.

The inverse rotation is achieved by applying the reverse sequence of rotations:

$$\vec{r}_o = \boldsymbol{R_z}(\omega)\boldsymbol{R_x}(i)\boldsymbol{R_z}(\Omega)\vec{r}. \tag{4.2}$$
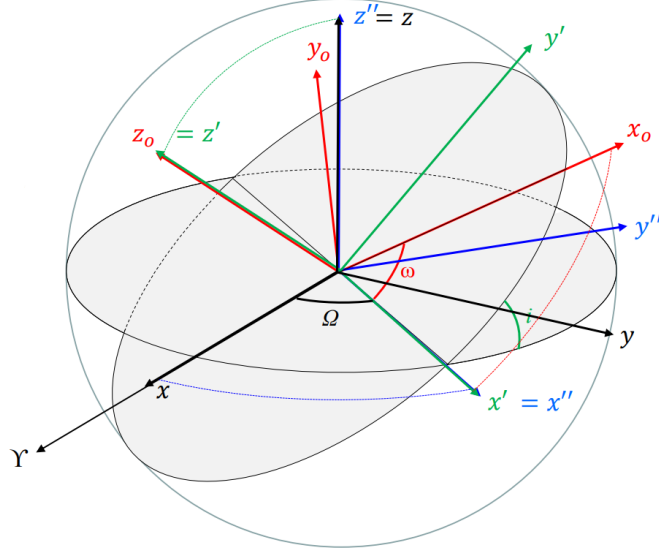
Figure 4.2: Rotations required to transform the ECI frame into the orbital frame.

4.2 Radar measurements

A radar system has the ability to determine both the position and range rate of a target. Thus, when utilizing a setup with two sensors, it furnishes a total of eight pieces of information: two position vectors at two distinct time points (t_1 and t_2), along with two range rates. The information concerning the target's position alone is adequate for computing a unique orbit. Therefore, the range rates are initially disregarded in the analysis. This decision is rooted in the reality that, although an infinite number of ellipses can be drawn through two given points, only one ellipse aligns with the time interval between the two measurements. Notably, for a known orbit, it is possible to calculate the time required for a target to traverse from one point to another on the orbit, using Kepler's equation:

$$E - e\sin E = M \tag{4.3}$$

The angle E, known as the eccentric anomaly, is determined by constructing an auxiliary circle around an ellipse and then drawing a line perpendicular to the semi-major axis, as illustrated in the Figure 4.3.

The eccentric anomaly is related to the true anomaly by the following equation [37]:

$$\tan\frac{E}{2} = \frac{\sqrt{1-e}}{\sqrt{1+e}}\tan\frac{v}{2}. \tag{4.4}$$

As previously mentioned, the mean anomaly (M) can also be expressed as follows:

$$M = n\big(t - t_p\big), \tag{4.5}$$

where n is the mean angular velocity, calculated as 2π divided by the period of the orbit (T), and the perigee passing time (t_p) is defined as zero. Therefore, from the true anomaly (v), which represents the angular position within the orbit, you can determine the exact moment when that point is reached.

$$t_i = \frac{M_i}{n}. \tag{4.6}$$
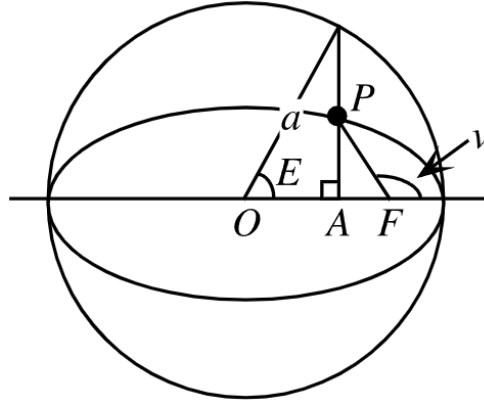
Figure 4.3: Eccentric anomaly E and Kepler's auxiliary circle [39].

4.3   From radar measurements to Keplerian elements

4.3.1 Orbit determination from position measurements

The radar provides the following data:

- $\vec{\rho_1}$: position vector of the target when it crosses the first radar beam, in the radar reference system.
- $\vec{\rho_2}$: position vector of the target when it crosses the second radar beam, in the radar reference system.
- Δt: time interval between the two detections.

These positions, represented by vectors $\vec{\rho_1}$ and $\vec{\rho_2}$, can be readily transformed into the Earth-centered inertial frame, where they are denoted as $\vec{r_1}$ and $\vec{r_2}$. As both vectors lie within the orbital plane, their cross-product results in a vector that is orthogonal to the plane (Figure 4.4), and consequently, parallel to the axis z_o.

$$\vec{h} = \frac{\vec{r_1} \times \vec{r_2}}{|\vec{r_1} \times \vec{r_2}|}. \tag{4.7}$$

The unit vector in question adequately defines the orbital plane, and, as a result, determines the two associated Keplerian elements: inclination and the right ascension of the ascending node (Ω):

$$i = \text{acos} \frac{h_z}{|\vec{h}|},$$

(4.8)

$$\Omega = \text{atan} \frac{-h_y}{h_x}.$$

(4.9)
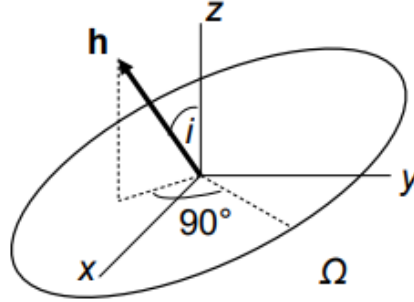
Figure 4.4: Angular momentum vector in the ECI frame.

It is noteworthy that Ω can range from -180° to 180°, and therefore, it is crucial to adjust the output of the arctangent function as needed. This adjustment is not necessary for the inclination angle, as it remains within the bounds of -90° to 90°. Specifically, a negative inclination signifies a retrograde orbit, indicating that the object orbits in the opposite direction to the Earth's rotation about its axis. In such cases, the calculation of $\vec{h}$ should be conducted as follows:

$$\vec{h} = \frac{\vec{r_2} \times \vec{r_1}}{|\vec{r_1} \times \vec{r_2}|}.$$

(4.10)

In the MATLAB script (Appendix **Error! Reference source not found.**, these two scenarios are differentiated based on the sign of Δt, which represents the time difference between when the object crosses the second beam (t_2) and when it crosses the first beam (t_1), regardless of whether the orbit is prograde or retrograde. Therefore, in the first case, Δt is positive, while in the latter case, it is negative.

Once these two elements are calculated, the complexity of the problem can be reduced to a bidimensional framework. It becomes feasible to define the two positions corresponding to the detections in a new orbital reference frame by applying the following rotation:

$$\vec{r}' = \boldsymbol{R_1}(i)\boldsymbol{R_3}(\Omega)\vec{r}.$$

(4.11)

The new reference system is illustrated in Figure 4.5 and in Figure 4.2 (green). The coordinates in this system cannot be expressed using the previously defined orbital reference system (x_o, y_o, z_o) due to the unknown argument of periapsis (ω). However, it is worth noting that the two vectors, $\vec{r_1}'$ and $\vec{r_2}'$, lie within the (x', y') plane.
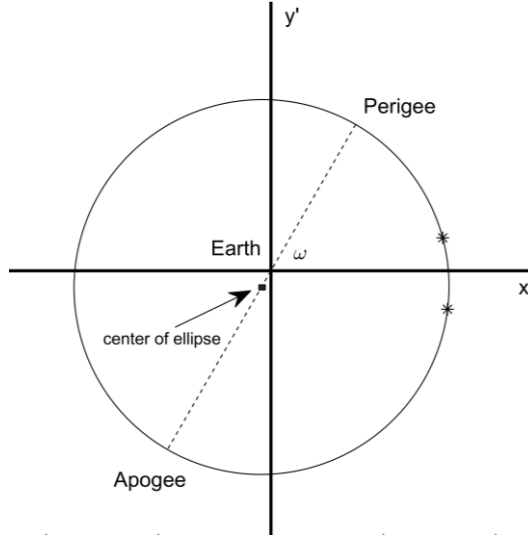
Figure 4.5: New orbital reference system with the x-axis directed toward the ascending node.

The subsequent step involves computing three elements that characterize the ellipse within the orbital plane: the semimajor axis (a), the eccentricity (e), and the argument of perigee (ω). The argument of perigee determines the angle between the semimajor axis and the x' axis. From now on, the reference system depicted in Figure 4.5 will be the sole reference system used, and therefore, the apex will not be explicitly written to enhance clarity in notation.
The general equation of an ellipse is expressed as [2]:

$$(\vec{r} - \vec{r}_c)^T \boldsymbol{E} \, (\vec{r} - \vec{r}_c) - 1 = 0 \,, \tag{4.12}$$

where $\vec{r}_c$ is the vector that represents the center of the ellipse. In this reference system, it is given by:

$$\vec{r}_c = -a \cdot e \cdot (\cos \omega \,, \sin \omega)^T \,. \tag{4.13}$$

The matrix $\boldsymbol{E}$ can be obtained by the following matrix product:

$$\boldsymbol{E} = \boldsymbol{R} \boldsymbol{D} \boldsymbol{R}^T, \tag{4.14}$$

where $\boldsymbol{D}$ and $\boldsymbol{R}$ are expressed by the following equations:

$$\boldsymbol{D} = \begin{bmatrix} 1/a^2 & 0 \\ 0 & 1/b^2 \end{bmatrix}, \tag{4.15}$$

$$\boldsymbol{R} = \begin{bmatrix} \cos \omega & -\sin \omega \\ \sin \omega & \sin \omega \end{bmatrix}. \tag{4.16}$$

The semi-minor axis b can be expressed as function of the semi-major axis and the eccentricity:

$$b^2 = a^2(1 - e^2) \,. \tag{4.17}$$

Using the latter equation and through a series of calculations, the explicit form of the matrix $\boldsymbol{E}$ can be derived:

$$E = \frac{1}{a^2} \begin{bmatrix} \cos\omega + \dfrac{\sin\omega}{1-e^2} & \dfrac{1}{2} \cdot \sin 2\omega \cdot \left(1 - \dfrac{1}{1-e^2}\right) \\ \dfrac{1}{2} \cdot \sin 2\omega \cdot \left(1 - \dfrac{1}{1-e^2}\right) & \sin\omega + \dfrac{\cos\omega}{1-e^2} \end{bmatrix}. \tag{4.18}$$

The parameters that define the ellipse $(E, \vec{r}_c)$ functions of the three Keplerian elements: a, e and ω. Nevertheless, since only two points on the ellipse are known, this leads to two non-linear equations:

$$\begin{cases} (\vec{r}_1 - \vec{r}_c(a,e,\omega))^T E(a,e,\omega) \ (\vec{r}_1 - \vec{r}_c(a,e,\omega)) - 1 = 0 \\ (\vec{r}_2 - \vec{r}_c(a,e,\omega))^T E(a,e,\omega) \ (\vec{r}_2 - \vec{r}_c(a,e,\omega)) - 1 = 0 \end{cases}, \tag{4.19}$$

However, these two equations are insufficient to calculate all three Keplerian elements. Yet, it is important to note that the time information has not yet been utilized. The time interval between the two measurements is also dependent on the same set of elements:

$$\Delta t = t_2 - t_1 = \frac{M_2 - M_1}{n} = \frac{M(v_2, e) - M(v_1, e)}{n(a)} = f(a, e, \omega). \tag{4.20}$$

Indeed, the true anomalies of the two target positions (v_1 and v_2) are function of ω:

$$v_i = \omega_i - \omega, \qquad \text{with } i = 1,2. \tag{4.21}$$

Here, ω_i represents the angle that characterizes the positions of the known points within the reference system defined in Figure 4.5.

The numerical method employed for solving this problem capitalizes on the fact that the semi-major axis has the most significant impact on Δt, particularly for orbits characterized by low eccentricity. The method begins by assuming an initial value for the semi-major axis, denoted as a_0. Using this assumed semi-major axis, e and ω can be calculated by solving the system (4.18). The result yields an elliptical orbit that passes through the two desired points ($\vec{r}_1$ and $\vec{r}_2$). However, the time between these two points on the computed orbit may not necessarily match the interval Δt obtained from radar measurements.

This discrepancy in time is utilized to compute a correction to the semi-major axis (Δa). This process is iterated until the correction falls below a predefined threshold, as depicted in Figure 6. Additionally, it is necessary to set a maximum number of iterations. To facilitate the solution of the non-linear system, the variables are made non-dimensional at each generic iteration, using a_0 as the length scale.

Therefore, at any given iteration:

$$v_i = \omega_i - \omega, \qquad \text{with } i = 1,2, \tag{4.22}$$

$$\vec{r}_c = -\frac{a_i}{a_0} * e * (\cos\omega, \sin\omega)^T, \tag{4.23}$$

$$E_i = \frac{a_0^2}{a_i^2} \begin{bmatrix} \cos\omega + \dfrac{\sin\omega}{1-e^2} & \dfrac{1}{2}\cdot\sin 2\omega \cdot \left(1 - \dfrac{1}{1-e^2}\right) \\ \dfrac{1}{2}\cdot\sin 2\omega \cdot \left(1 - \dfrac{1}{1-e^2}\right) & \sin\omega + \dfrac{\cos\omega}{1-e^2} \end{bmatrix}. \tag{4.24}$$

Updating the semi-major axis is a crucial step for achieving convergence. The time interval between the two known points can be expressed as:

$$\Delta t_i = f(a_i, e_i, \omega_i) = f_i. \tag{4.25}$$

By utilizing the Taylor expansion, it becomes possible to express:

$$f(a, e, \omega) - f(a_i, e_i, \omega_i) \approx f_a(a_i, e_i, \omega_i)\Delta a, \quad \text{with } f_a = \frac{\partial f}{\partial a} \tag{4.26}$$

because the dependence of f on e and ω is relatively small. Now, it is feasible to compute the correction to the semi-major axis required to achieve an orbit that aligns with the time interval specified by the radar measurement from this expression:

$$\Delta a = \frac{f(a, e, \omega) - f(a_i, e_i, \omega_i)}{f_a(a_i, e_i, \omega_i)} = \frac{\Delta t - \Delta t_i}{f_a(a_i, e_i, \omega_i)}. \tag{4.27}$$

The value of the partial derivative can be approximated using finite differences:

$$\frac{\partial f}{\partial a}(a_i, e_i, \omega_i) \approx \frac{f(a_i + dx, e_i, \omega_i) - f(a_i - dx, e_i, \omega_i)}{2 \cdot dx}. \tag{4.28}$$

After computing the Keplerian elements that characterize the orbital geometry, deriving the final element associated with time (the true anomaly at a given epoch) becomes a straightforward process. This is facilitated by the known moment when the target intersects the initial beam, along with the corresponding true anomaly that characterizes that particular point, given the well-defined orbit geometry. Furthermore, leveraging these pieces of information enables the determination of the time at which the perigee is crossed.

The method has proven effective for higher eccentricities exceeding 0.01, delivering a balance of computational efficiency and solution accuracy across various orbital trajectories. However, its performance can falter for orbits with lower eccentricities. Particularly in low Earth orbits (LEOs), where objects often exhibit minimal eccentricity, the method tends to fluctuate around the correct semi-major axis, despite delivering near-exact solutions for the argument of perigee and eccentricity. To address this issue, a new strategy has been developed. This approach involves reconfiguring the system of equations, including an additional equation that accounts for the time interval between observations and the unknown parameters of semi-major axis, eccentricity, and argument of perigee (a, e, ω).

$$\begin{cases} (\vec{r}_1 - \vec{r}_c(a, e, \omega))^T E(a, e, \omega)\,(\vec{r}_1 - \vec{r}_c(a, e, \omega)) - 1 = 0 \\ (\vec{r}_2 - \vec{r}_c(a, e, \omega))^T E(a, e, \omega)(\vec{r}_2 - \vec{r}_c(a, e, \omega)) - 1 = 0 \\ \Delta t - f(a, e, \omega) = 0 \end{cases}. \tag{4.29}$$

The revised system now comprises three equations and three unknowns, making it suitable for numerical solution. A viable starting point for solving this system is to leverage the algorithm

output described earlier. Attempting to solve system (4.27) directly without a close initial estimate of the exact solution would pose a significant challenge, particularly due to the intricate dynamics of low eccentricity. In such cases, small variations in the argument of perigee (ω) have minimal effect on the time interval, thereby making it difficult to pinpoint the correct ω value without an approximate solution to guide the process.
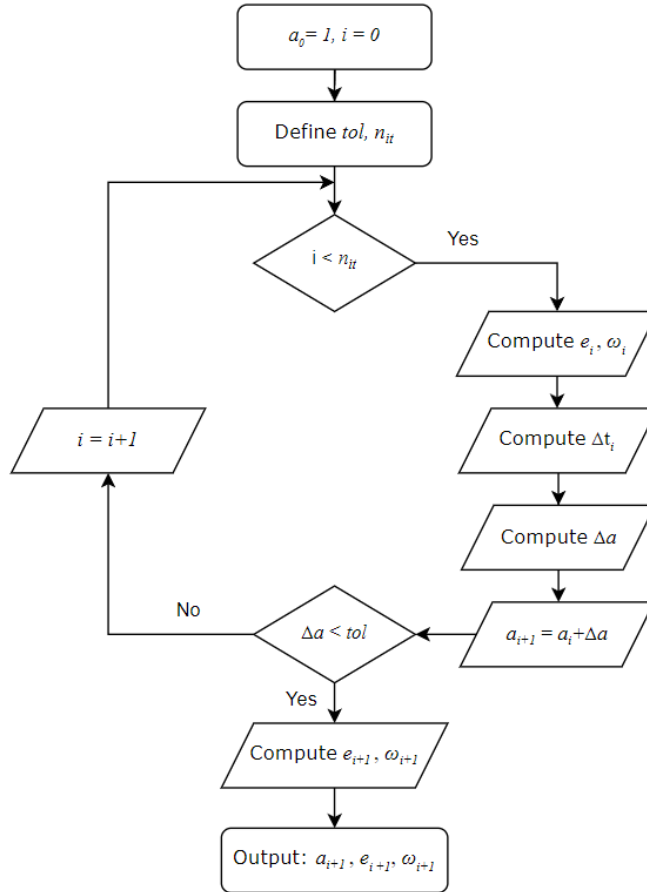
Figure 4.6: Flow-chart of the algorithm to compute the Keplerian elements.

4.3.2 Orbit determination from radar measurements

It has been noted that merely two position measurements are adequate for ascertaining an orbit. Nonetheless, a radar system can furnish additional data in the form of range rate information, which can increase the orbit determination precision.

In such an instance, taking into account two detections, the equation count rises to 8, with 6 unknowns. Consequently, an overdetermined non-linear system may be articulated, utilizing the inverse technique delineated in the preceding paragraph. Specifically, instead of expressing the Keplerian elements as a function of radar measurements, the inverse is applied: the radar measurements are now represented as functions of the Keplerian elements. The vector containing the Keplerian elements is denoted by $\vec{x} = (a, e, i, \Omega, \omega, t_p)$, and the one containing the radar measurements as $\vec{y} = (\rho_1, \varphi_1, \theta_1, \dot{\rho}_1, \rho_2, \varphi_2, \theta_2, \dot{\rho}_2)$. The nonlinear system in this case is the following:

$$\vec{y}(\vec{x}) - \vec{y}_{obs} = 0 \, , \tag{4.30}$$

where $\vec{y}_{obs}$ contains the actual observations made by the radar.

Additional information is provided by the delta time between detections. However, it is not incorporated into the vector $\vec{y}$, as it is considered unaffected by error and is thus regarded as a constraint. Consequently, the system is addressed utilizing the least squares method, a standard technique in regression analysis, to approximate the solution of overdetermined systems. This method achieves this by minimizing the sum of the squares of residuals, with each residual denoting the difference between an observed value and the corresponding fitted value provided by a model. Ultimately, the function f to minimize is represented as follows:

$$f = \|\vec{y}(\vec{x}) - \vec{y}_{obs}\| \, , \tag{4.31}$$

with the constraint

$$\Delta t(\vec{x}) - \Delta t_{obs} = 0. \tag{4.32}$$

In order to solve this problem, the MATLAB function "lsqnonlin" is exploited, using the solution provided by the method presented in the previous paragraph as starting value.

4.4   Error propagation

Radar measurements are susceptible to errors, which can be aptly characterized by a Gaussian distribution. The standard deviation of these errors is contingent upon the signal-to-noise ratio. Specifically, the determination of the target's position relies on measuring the range, namely the distance between the radar and the object, as well as the elevation and cross-elevation. Errors in the measurement of these angles result in two cross-range errors, typically surpassing the magnitude of the range error.

Hence, the two positions identified by the radar can be articulated as functions of the range (ρ), elevation (θ), and cross-elevation (α):

$$\vec{r_i} = f(\rho_i, \theta_i, \varphi_i) \, , \quad \text{for } i = 1, 2. \tag{4.33}$$

The additional variable utilized for orbit determination is Δt, which, although susceptible to error, bears a magnitude so small that its influence on the orbit is negligible. Indeed, an error on the order of milliseconds can substantially affect the distance covered by the signal, yet it remains inconsequential when compared to the timescale of the orbit.

Given the known distributions of errors in range, elevation, and cross-elevation, the current objective is to assess the repercussions of these errors on the orbit. As previously demonstrated, a generic Keplerian element (denoted as k_i) can be expressed as function of the range and two measured angles from both beams:

$$k_i = f(\rho_1, \theta_1, \varphi_1, \rho_2, \theta_2, \varphi_2, \Delta t) = f(\vec{x}), \tag{4.34}$$

when f is a set of non-linear combination of the variables $\vec{x}$.

In a probabilistic approach, the function f is typically linearized by approximating it to a first-order Taylor series expansion. The general form of the Taylor expansion is:

$$f \approx f_0 + \sum_i \frac{\partial f}{\partial x_i} x_i ,$$ (4.35)

where $\partial f / \partial x_i$ denotes the partial derivative of f with respect to the i-th variable, calculated at the mean value of all components of vector $\vec{x}$. This can also be expressed in matrix notation as:

$$f \approx f_0 + \vec{\nabla} \cdot \vec{x}.$$ (4.36)

where $\vec{\nabla}$ is the gradient of the function f, calculate at the point x_0. Since f_0 is a constant, it does not contribute to the error on f:

$$\sigma_f^2 = \mathrm{cov}(f,f) \approx \mathrm{cov}(f_0 + \vec{\nabla} \cdot \vec{x}, f_0 + \vec{\nabla} \cdot \vec{x}) = \mathrm{cov}(\vec{\nabla} \cdot \vec{x}, \vec{\nabla} \cdot \vec{x}) = \sum_{i,j=1} \frac{\partial f}{\partial x_i} \frac{\partial f}{\partial x_j} \mathrm{cov}(x_i, x_j).$$ (4.37)

Assuming independent variables the standard deviation of the function f is equal to

$$\sigma_f = \sqrt{\sum_i \left(\frac{\partial f}{\partial x_i} \sigma_i \right)^2 },$$ (4.38)

where σ_f represents the standard deviation of the function f, σ_i represents the standard deviation of x_i. It is important to note that this formula is based on the linear characteristics of the gradient of f and therefore it is a good estimation for the standard deviation of f as long as σ_i are small enough [9].

For vectorial function the gradient is substituted by the Jacobian matrix J, and it can be proved that the Jacobian of the function is used to transform the rows and columns of the variance-covariance matrix of the argument [16]:

$$\Sigma^f = J \Sigma^f J^T .$$ (4.39)

Since the derivation of the Keplerian elements is done using an iterative method, it is difficult to calculate the partial derivative analytically, therefore a finite difference approximation is employed. In case $\vec{f}$ is the vectorial function containing the Keplerian elements, the Jacobian matrix will be as follows:

$$J = \begin{bmatrix} \frac{\partial a}{\partial \rho_1} & \frac{\partial a}{\partial \theta_1} & \frac{\partial a}{\partial \varphi_1} & \frac{\partial a}{\partial \rho_2} & \frac{\partial a}{\partial \theta_2} & \frac{\partial a}{\partial \varphi_2} \\[2mm] \frac{\partial e}{\partial \rho_1} & \vdots & \cdots & \cdots & \vdots & \frac{\partial e}{\partial \varphi_2} \\[2mm] \frac{\partial i}{\partial \rho_1} & \frac{\partial i}{\partial \theta_1} & \cdots & \cdots & \frac{\partial i}{\partial \theta_2} & \frac{\partial i}{\partial \varphi_2} \\[2mm] \frac{\partial \Omega}{\partial \rho_1} & \vdots & \cdots & \cdots & \vdots & \frac{\partial \Omega}{\partial \varphi_2} \\[2mm] \frac{\partial \omega}{\partial \rho_1} & \frac{\partial \omega}{\partial \theta_1} & \frac{\partial \omega}{\partial \varphi_1} & \frac{\partial \omega}{\partial \rho_2} & \frac{\partial \omega}{\partial \theta_2} & \frac{\partial \omega}{\partial \varphi_2} \end{bmatrix}$$ (4.40)

In Figure 4.7 the standard deviations for various Keplerian elements are presented as a function of the radar elevation angle, using just the information about the position. Specifically, the impact of the orbit inclination is analyzed while keeping all other Keplerian elements constant ($a = 8371$ km, $e = 0.01$, $\Omega = 90°$, $\omega = 90°$). Since the magnitude of the semi-major axis error is much larger than the others, in the plot, each standard deviation is divided by the corresponding Keplerian element to calculate the relative error. Notably, the eccentricity and argument of perigee yield the largest relative errors, which is sensible as a slight positional error, especially in orbits with minimal eccentricity, can yield significant fluctuations in these two elements. To gain a more nuanced understanding of error profiles, they are normalized (as depicted in the right segment of Figure 4.7), revealing a drop in error for both Ω and e with increasing elevation, while other profiles exhibit a minimum. The semi-major axis and argument of perigee share an almost identical profile, indicating a strong correlation, with a decreasing minimum as inclination increases. Conversely, the inclination error demonstrates an opposing trend.
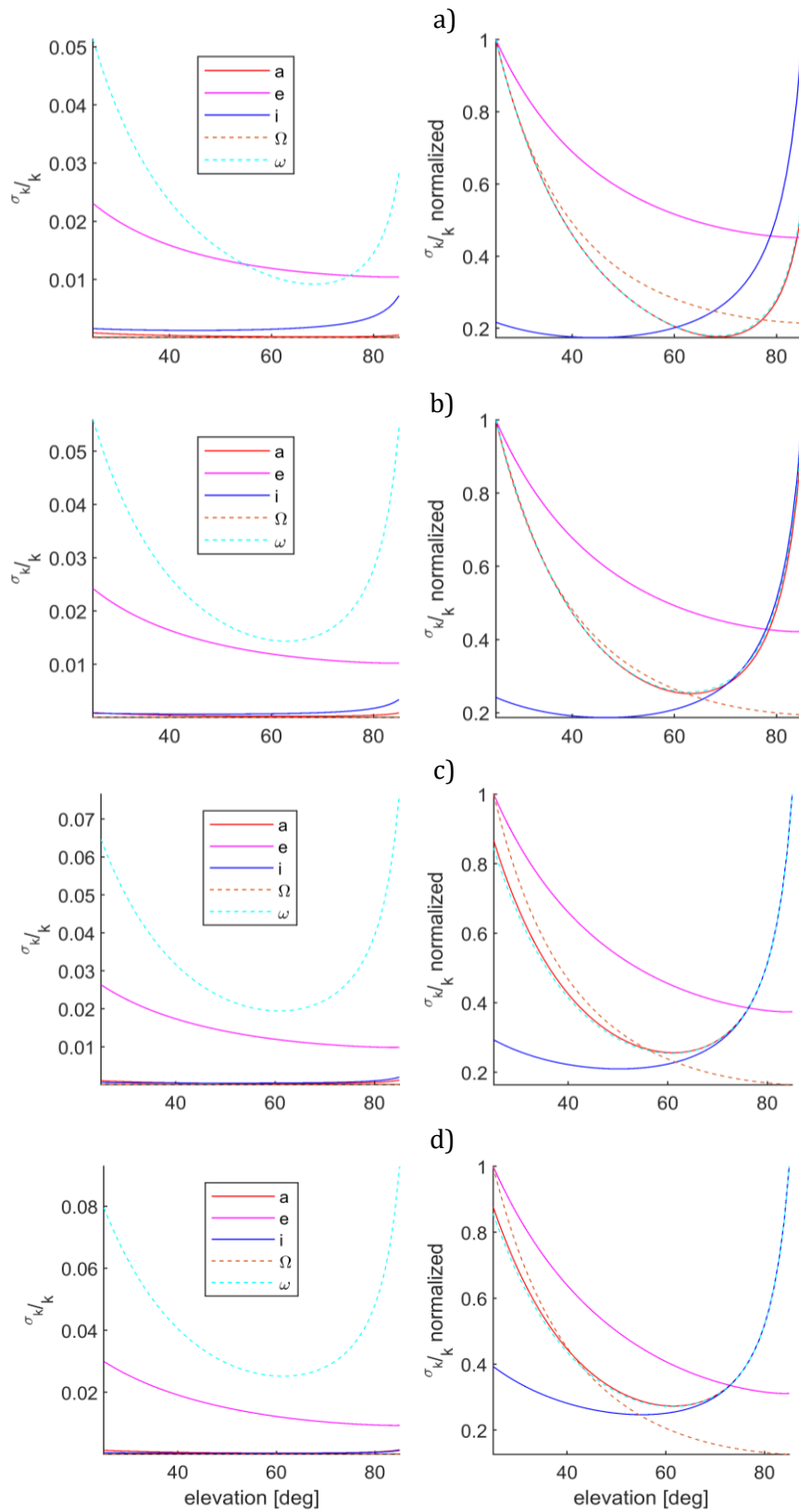
Figure 4.7: Relative standard deviation of each Keplerian element as function of the elevation angle for different orbital inclinations (10° (a), 20° (b), 30° (c), 40° (d))

4.5 RSW error

Identifying the Keplerian elements that exert a greater impact on orbit precision is challenging, as it depends on the specific characteristics of the orbit. For instance, in a low eccentricity orbit, a substantial error in the argument of perigee has a minor effect, given that the orbit altitude remains nearly constant regardless of the error. Therefore, a more insightful indication can be derived from the time evolution of the orbit position error. This is determined by subtracting the position vector obtained from radar measurements at a particular time from the exact position vector:

$$\overrightarrow{\Delta r}(t) = \vec{r}(t) - \vec{r}_{ex}(t).\qquad(4.41)$$

This vector can be decomposed in the RSW reference system. In the RSW frame, the x-axis of the RSW frame points away from the origin, and the y-axis lies in the orbital plane, and is positive in the direction of the velocity vector (Figure 4.8).
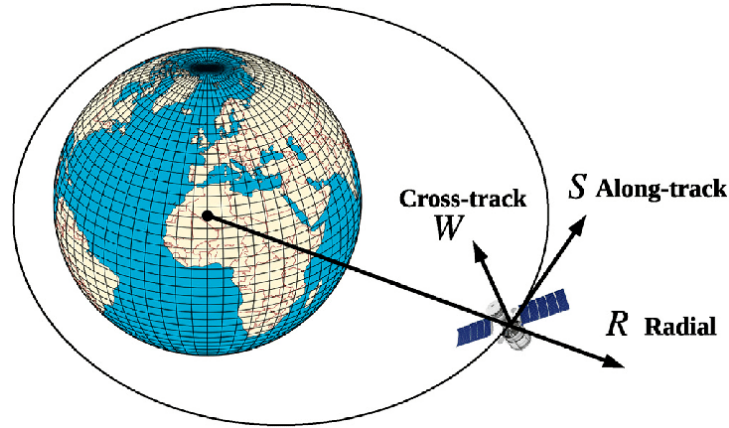
Figure 4.8: RSW reference system [6].

The influence of each variable $(\rho_1, \theta_1, \alpha_1, \rho_2, \theta_2, \alpha_2)$ on position error for a specific orbit is portrayed in Figure 4.9. In each subplot, the position error in the RSW reference frame is depicted, considering solely a single error in one of the measurements at the time. This error aligns with the standard error of the corresponding measurement. Consequently, the plots defined by elevation or cross-elevation errors illustrate a greater error in orbit determination than those characterized by range error. The dominant component of the error in each instance is the S-component, which is delineated by a profile resulting from a blend of a linear trend and an oscillation for every component.

The same scrutiny is conducted utilizing the least squares method, as demonstrated in Figure 4.10. Here, range rate information introduces a new error source but significantly boosts orbit determination precision. Particularly, it aids in mitigating the influence of elevation error.
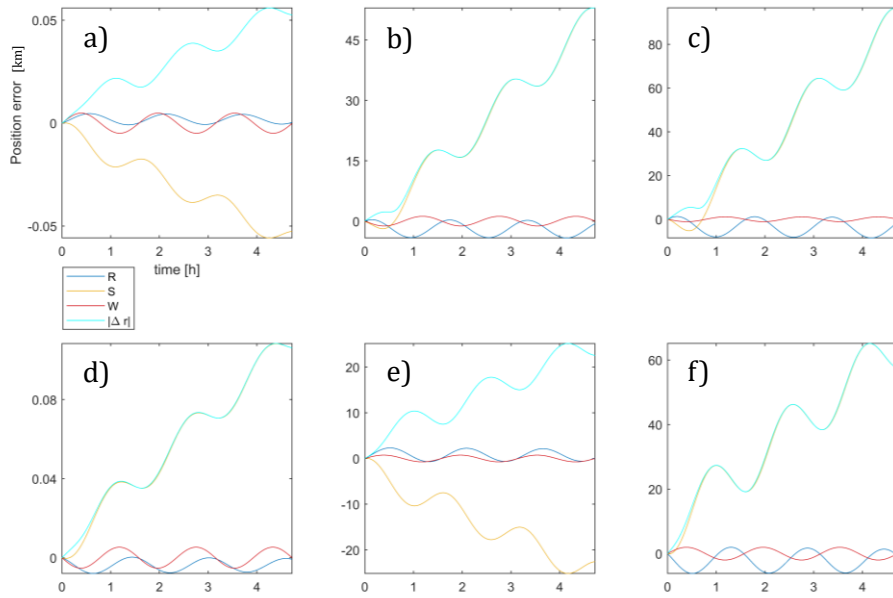
Figure 4.9: Position error in the RSW reference frame calculated using the fitting orbit algorithm,
considering a single error in one of the measurement component at a time:
$\rho_1\ (a), \theta_1\ (b), \varphi_1\ (c), \rho_2\ (d), \theta_2\ (e), \varphi_2\ (f).$
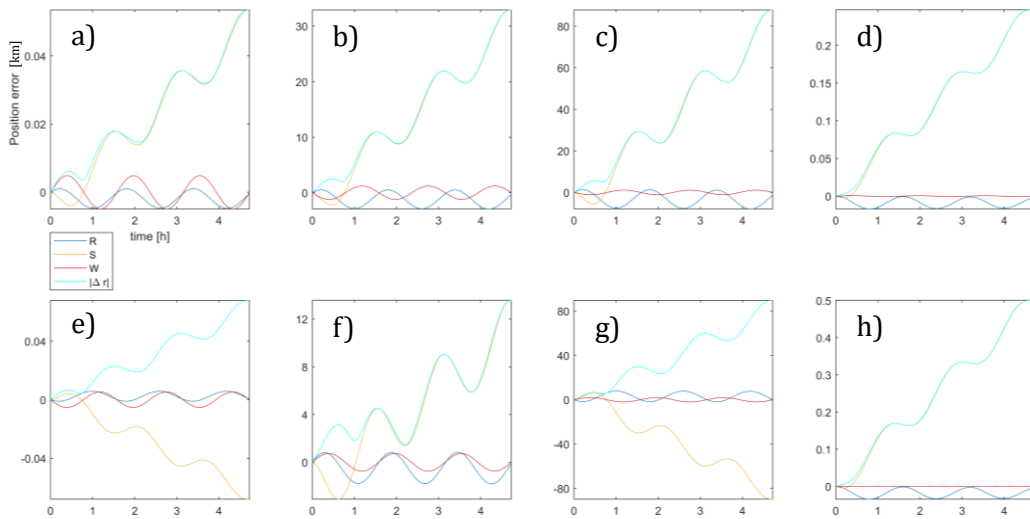
Figure 4.10: Position error in the RSW reference frame calculated using the LSM,
considering a single error in one of the measurement component at a time:
$\rho_1\ (a), \theta_1\ (b), \varphi_1\ (c), \dot{\rho}_1\ (d), \rho_2\ (e), \theta_2\ (f), \varphi_2\ (g), \dot{\rho}_2\ (h).$

The objective now is to identify an elevation angle that yields satisfactory orbit accuracy using two radar measurements. It has been established that the error in the S-direction significantly surpasses that of the other two directions within just three revolutions. The error profile exhibits a composite structure, combining a linear trajectory and sinusoidal oscillations. However, while the latter maintains a constant amplitude, the linear component propels error growth over time. Consequently, the accuracy of orbital determination can be aptly summarized by the S-component error after a set number of revolutions, discounting the

oscillations. This parameter, denoted as e_S, can be represented as a function of radar measurements. Thus, its standard deviation can be ascertained in a manner similar to the Keplerian elements, employing Equation (4.32).

Alternatively, the distribution of e_S can be examined through the Monte Carlo method, simulating numerous detections generated from the normal distribution of each measurement. An illustration of this approach is presented in Figure 4.11, where two scenarios are considered: one utilizing the orbit fitting algorithm (a), and the other employing the least squares method (b). The parameter e_S is evaluated after 10 revolutions.

In both cases, the parameter retains the normal distribution of the measurements, centered at zero. However, the substantial computational cost associated with the Monte Carlo method renders its use impractical for the current objectives. Since various elevation angles and inclinations necessitate examination, generating a substantial number of measurements sets for each parameter combination would be requisite.
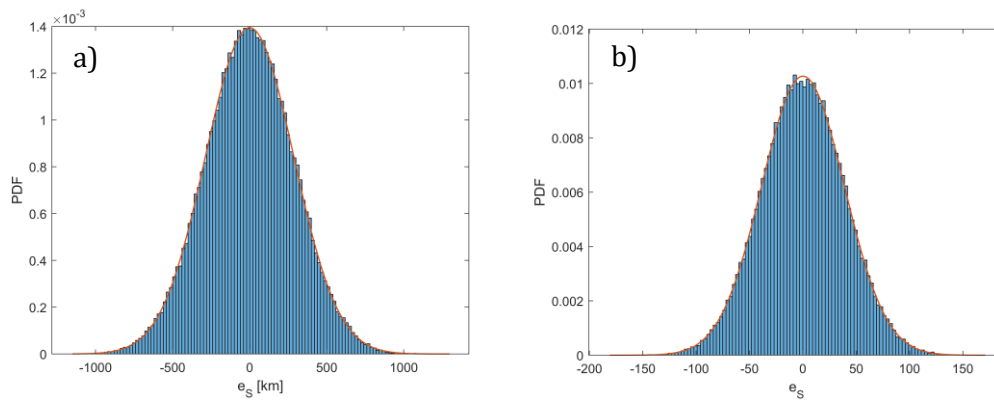
Figure 4.11: Distribution of the parameter e_S after 20 revolution, using a fence elevation of 70°.

4.6   Results

The results from the fitting orbit algorithm are illustrated in Figure 4.12, representing an orbit characterized by variable inclination and mean altitude. In terms of the other Keplerian elements, the orbit exhibits an eccentricity of 0.01, with both Ω and ω set at 90°. A notable divergence from the previous model, discussed in earlier chapters, is the dependence of the optimal elevation (θ_{opt}) on orbit altitude, which intensifies as inclination rises. However, the most significant departure pertains to the behavior of θ_{opt} in relation to inclination. In contrast to the previous model where θ_{opt} rises monotonically with increasing inclination, in this scenario, θ_{opt} initially decreases before experiencing an ascent for inclinations beyond 32-40 degrees. Further investigation is warranted to comprehensively comprehend the underlying factors driving this distinctive profile.
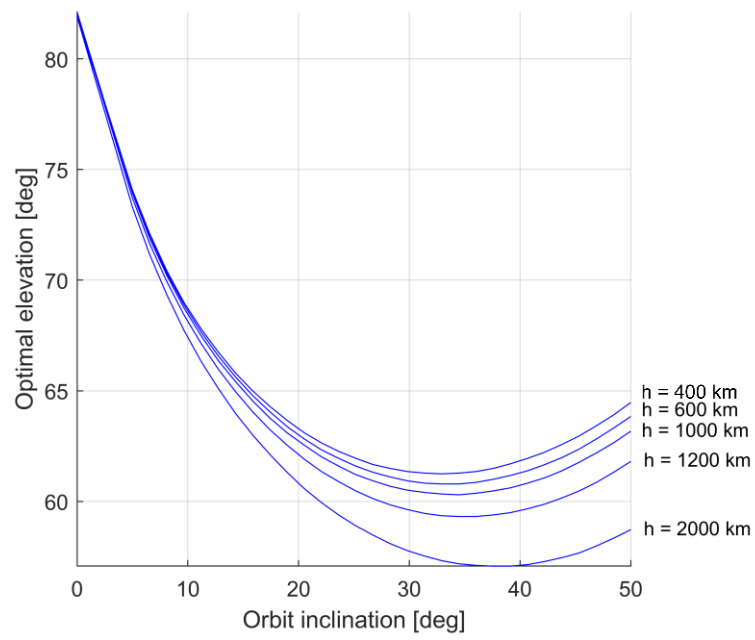
Figure 4.12: Optimal elevation for the double fence configuration.

Chapter 5 : Space Objects in Low Earth Orbit (LEO)

5.1　Low Earth Orbits

In order to assess radar performance through a simulated scenario, a comprehensive analysis of Low Earth Orbit (LEO) space object characteristics is essential. The LEO definition employed in this study aligns with the one provided by USSPACECOM, which considers orbits with a period of 128 minutes or less and an eccentricity less than 0.25 [34]. The orbital period is indicative of an orbit altitude of approximately 2042 km in the case of a circular orbit, which is consistent with the upper altitude limits in certain LEO definitions.

A catalogue containing details of all known objects is available on "SpaceTrack.com", presenting two-line elements for each object, along with a catalog number and classification. Analyzing this catalog offers an overview of the objects and their orbits. The catalog, current as of December 15th , 2023, comprises 21174 LEO objects, which include 9,654 debris and unknown objects, 932 rocket bodies, and the remaining are satellites.

Given the immense computational cost associated with simulating all these objects, the aim is to analyze the catalog to extract valuable information about the orbits. This information is then utilized to conduct a simulation with a significantly reduced number of objects, which nonetheless presents a realistic scenario. To realize this objective, semimajor-axis, eccentricity, inclination, and right ascension of ascending node distributions are examined. The findings are summarized in Figure 5.1.

Satellites are most abundant at around 500 km of altitude, an area largely occupied by the Starlink constellation. Conversely, debris is scarce there, largely due to atmospheric drag, which effectively maintains cleanliness in the region. Debris in orbits below 600 km usually re-enter Earth's atmosphere within several years. At altitudes of 800 km, orbital decay can take centuries, while above 1000 km, debris may continue orbiting Earth for over a millennium [27].
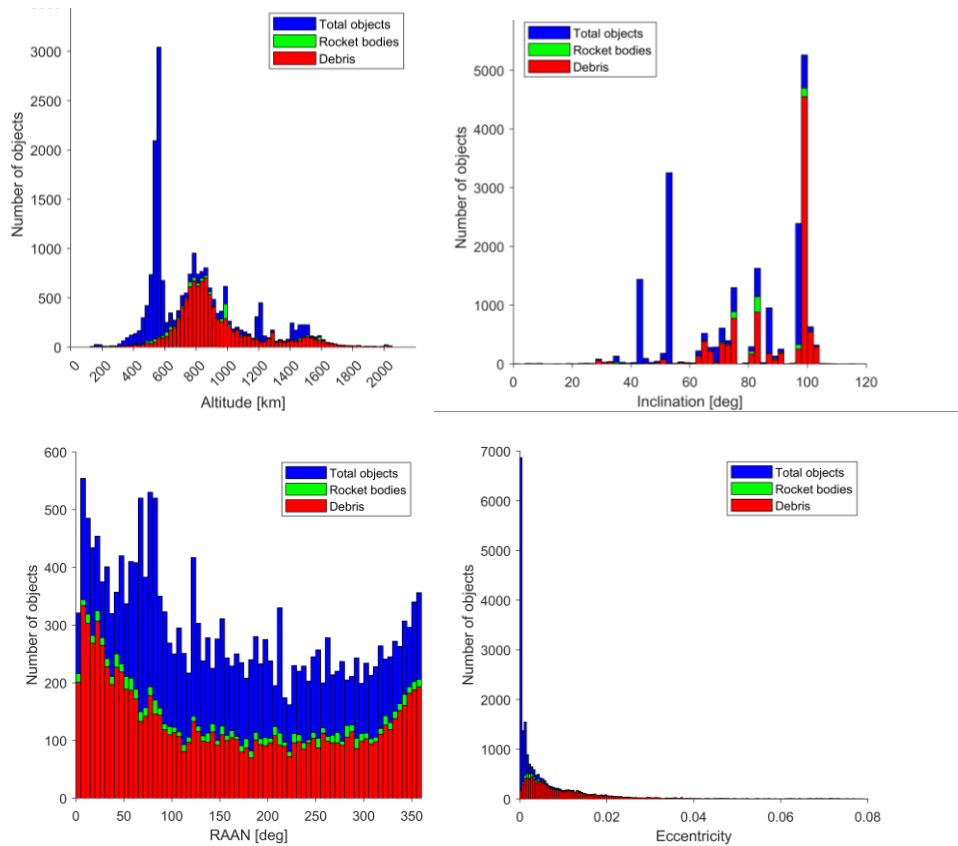
Figure 5.1: Keplerian elements distribution for objects in LEO.

The proliferation of debris can be traced back to two major incidents. The first event, which significantly increased the debris count, occurred on February 10, 2009. It involved the accidental collision of two communications satellites - the active commercial Iridium 33 and the defunct Russian military Kosmos 2251. The collision, occurring at a speed of 11.7 km/s, resulted in the creation of 1668 and 628 catalogued debris pieces, with 1141 and 364 pieces of tracked debris remaining in orbit as of January 2016 [33]. Fourteen years later, the US Space Surveillance Catalog listed 1,014 and 290 debris pieces still in orbit, respectively.

The second event that significantly contributed to the debris count was the 2007 Chinese ASAT test, which targeted the Chinese weather satellite, the FY-1C (COSPAR 1999-025A). The polar orbit satellite, located at an altitude of 865 km and weighing 750 kilograms [29], was destroyed by a kinetic kill vehicle. This test created the largest field of space debris in history, resulting in more than 3000 pieces of trackable size (golf ball size and larger) being catalogued immediately after the incident. An estimated 150000 debris particles were produced [28]. As of October 2016, a total of 3438 debris pieces had been detected, with 571 having decayed and 2867 remaining in orbit nine years after the incident.

More than half of the tracked debris orbits Earth with a mean altitude above 850 km, making it likely that they will remain in orbit for decades or centuries [28]. According to the NASA Orbital Debris Program Office, based on 2009 and 2013 calculations of solar flux, it is estimated that around 30% of the debris larger than 10 centimeters will still be in orbit by 2035 [38].

These two events have left a clear impact on the debris distribution, as illustrated in Figure 5.2. The first peak is attributed to the collision between the two satellites, while the second peak is a result of the Chinese ASAT test.
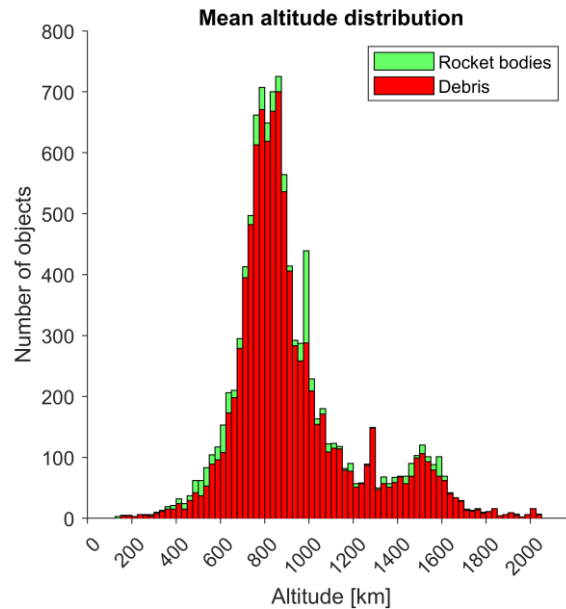
Figure 5.2: Mean altitude distribution of debris (red) and rocket bodies (green).

The altitude distribution is inherently linked to the inclination distribution, as evidenced by the involvement of satellites with high inclinations in these two significant events. For instance, Fengyun-1C had an inclination of 98.8 degrees, Iridium-33 had 86.4 degrees, and Kosmos-225 had 74.0 degrees. Moreover, the most densely populated LEO orbits include numerous Sun-synchronous satellites. These satellites maintain a fixed angle between the Sun and their orbital plane, facilitating consistent Earth observation angles and lighting conditions. Typically, Sun-synchronous orbits are polar, traversing over the polar regions. They exploit the Earth's J_2 gravitational perturbation to gradually alter their RAAN over time. Figure 5.3 illustrates the inclination as a function of orbit altitude for Sun-synchronous orbits.
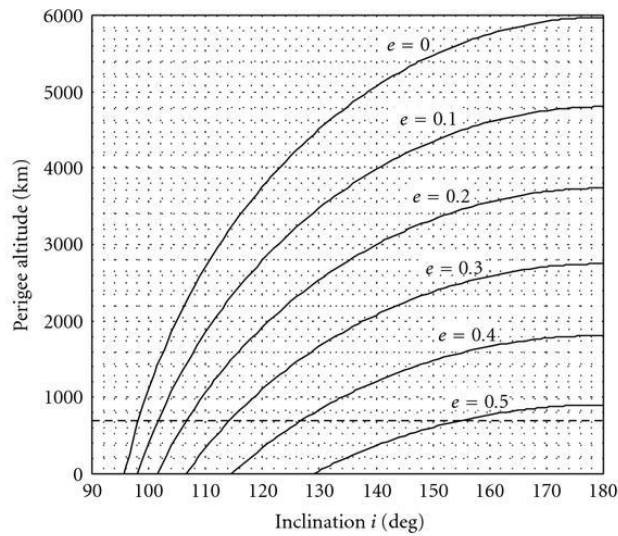
Figure 5.3: Inclination as function of the orbit altitude for Sun-synchronous orbit [1].

The RAAN profile appears to exhibit a random distribution due to various perturbation factors that continually alter the orbit planes around Earth's axis. These perturbations cause classical orbital elements to undergo consistent changes over time. Prior studies have indicated that, for reliable results, orbital elements with relatively small amplitude of variation, such as the semi-major axis, eccentricity, and inclination, are deemed stable, while elements with greater amplitude of variation are typically considered random. It is essential to understand that although collisions may generate debris with differing altitudes, inclinations, and eccentricities compared to the original satellite, these elements remain stable over time, as demonstrated in Figure 5.4 and Figure 5.5. These figures illustrate the evolution of spatial density of the fragments generated by an anti-satellite test, with one figure depicting the altitude and another showing the spreading of debris cloud orbital planes during the first year after the breakup, as a function of inclination. Notably, the fragments exhibit a tendency to maintain their altitude and inclination while the RAAN changes rapidly over time [30].
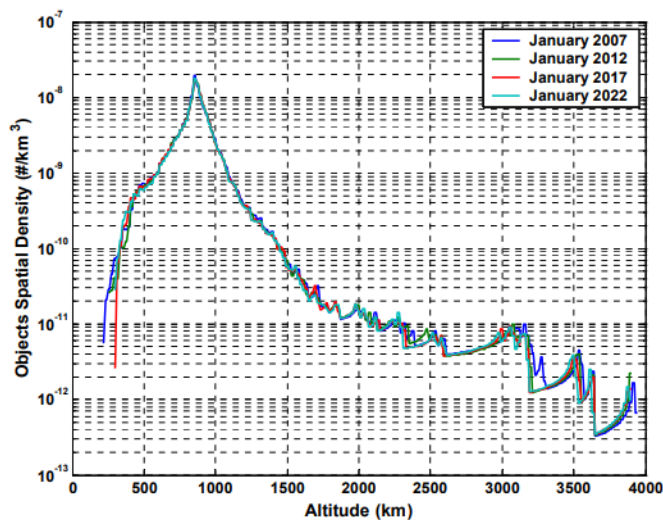
Figure 5.4: Evolution of the spatial density of the fragments generated by the anti-satellite test [30].

54
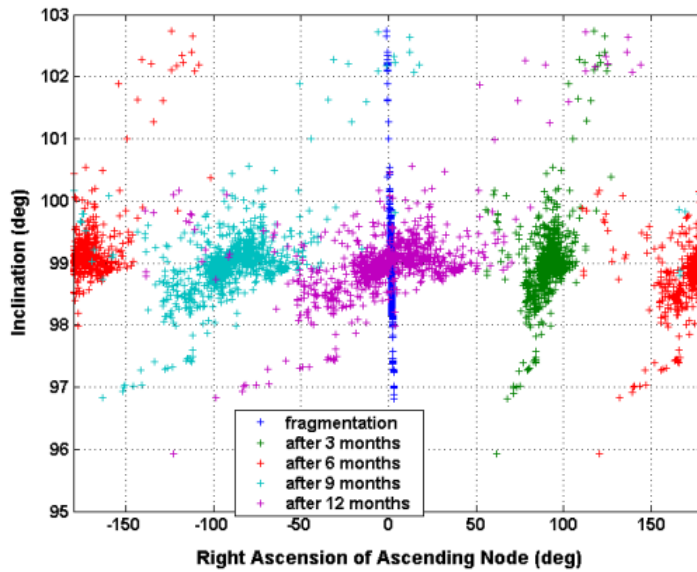
Figure 5.5: Spreading of the debris cloud orbital planes during the first year after the breakup [30].

In regard to eccentricity, a subtle discrepancy exists between satellites and other space objects. The majority of satellites exhibit an eccentricity smaller than 0.001, as illustrated in Figure 5.6. On the other hand, debris presents a distinct distribution, which resembles an exponential distribution with an average eccentricity of 0.0135.
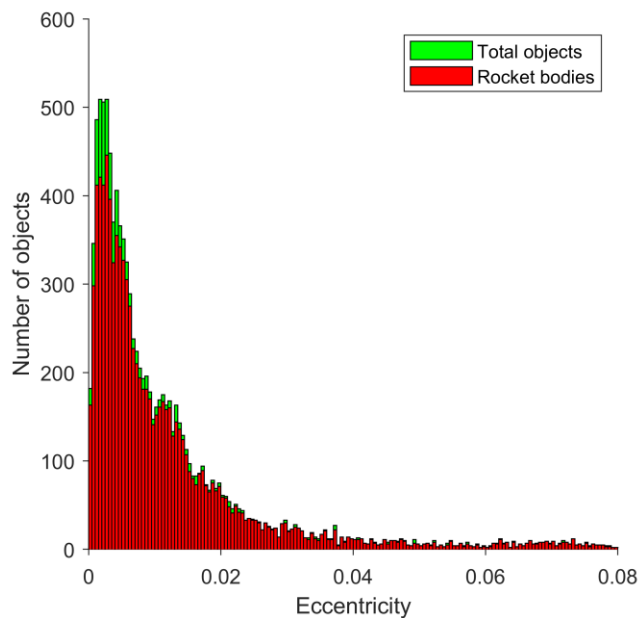
Figure 5.6: Eccentricity distribution of debris (red) and rocket bodies (green).

Based on this analysis, a practical compromise has been identified to approximate the environment, consisting of six altitude bands and four inclination bands. These bands and their corresponding representative values are shown in Table 5-1 and Table 5-2.

Table 5-1: Main altitude bands for LEO objects.

Representative altitude [km]	Altitude range [km]
550	500 < h < 600
825	750 < h < 900
1000	900 < h < 1100
1200	1100 < h < 1300
1500	1400 < h < 1600

Table 5-2: Main inclination bands for LEO objects.

Representative inclination	Inclination range
50°	40° < i < 60°
70°	60° < i < 80°
86°	80° < i < 92°
98°	94° < i < 102°

Not all orbit inclinations are detectable by the fence system, due to its inherent geometry. Consequently, the field of view is optimized to detect objects with higher inclinations, which tend to dominate the LEO region. This optimization is based on the analysis of the current catalogue. However, to increase the space environment awareness, additional radars capable of tracking orbits with small inclinations are necessary. This is particularly important because two objects with the same altitude, but different inclinations can still collide.

Another crucial point to note is that objects within a certain altitude band exhibit varied inclinations distribution, as depicted in Figure 5.7. For instance, the first altitude band, primarily occupied by Starlink satellites, comprises a mix of three inclination bands. Conversely, the second altitude band, housing debris from the aforementioned collisions, predominantly consists of polar orbits. This distinction enables a reduction in the number of required simulations.
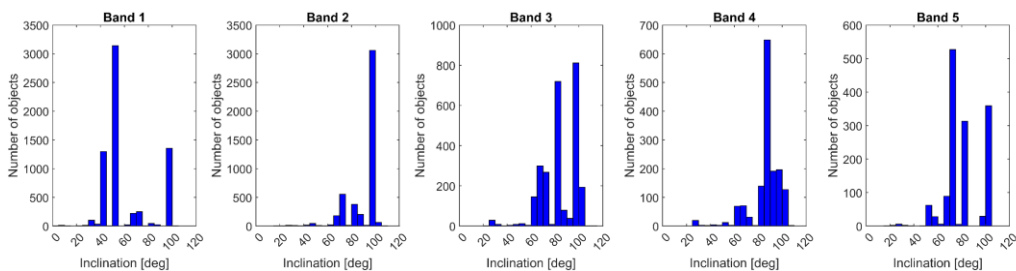
Figure 5.7: Inclination distribution for the different altitude bands.

5.2   Debris physical properties

Space debris is not only distinguished by diverse orbital characteristics but can also be classified based on size. The size of an individual object is a crucial factor due to its implications for trackability and the level of damage it could cause in the event of a collision. While larger objects can cause more considerable damage, it is the sheer volume of smaller objects in orbit that poses the current collision hazard.

Indeed, statistical models estimate that the number of debris objects currently in orbit (MASTER-8, projected to 2021) significantly exceeds the count of objects larger than 10 cm, as illustrated in Table 5-3. This underscores the magnitude of the challenge posed by smaller debris in terms of collision risks.

Table 5-3: ESA categorization of space debris by size, approximate numbers in orbit as of August 2022 [12].

Category	Diameter	Number in orbit	Trackability
Large	> 10 cm	36,500	Tracked and catalogued
Medium	1 cm to 10 cm	1,000,000	Trackable but with lower reliability
Small	1 mm to 1 cm	130,000,000	Not currently tracked

Even small debris can be incredibly destructive due to their high orbit velocities, especially given the substantial relative velocities between objects in Low Earth Orbit (LEO), often reaching approximately 10 km/s. Of the total space debris population, only objects classified as large and medium in size are currently trackable, as indicated in Table 5-3. These trackable objects represent a minor proportion (< 1%) of the overall space debris population. Medium-sized objects can be tracked using existing technology, but the reliability of this tracking can vary, with some objects being tracked intermittently (for example, through periodic radar surveys) and with lower precision.

The data presented in Table 5-3. is derived from the ESA's prominent MASTER (Meteoroid and Space Debris Terrestrial Environment Reference) risk assessment tool, which provides estimates of the orbital debris environment. Over the years, various models have been developed, one of the most well-known being the ORDEM (Orbital Debris Engineering Model) developed by NASA's Orbital Debris Program Office (ODPO). ORDEM is designed to offer information and estimates on the orbital debris environment (such as debris spatial density, flux, etc.) for engineering purposes, such as spacecraft design.

One of the pieces of information provided by ORDEM is the density of particles in circular and elliptical orbits as a function of altitude, as shown in Figure 5.8. Although these results are obtained from ORDEM96, which only considers data available up to 1995, it is evident that the profile of the distribution for objects larger than 100 micrometers is similar. This similarity indicates that across various altitude bands, the proportion of objects of varied sizes remains relatively constant.
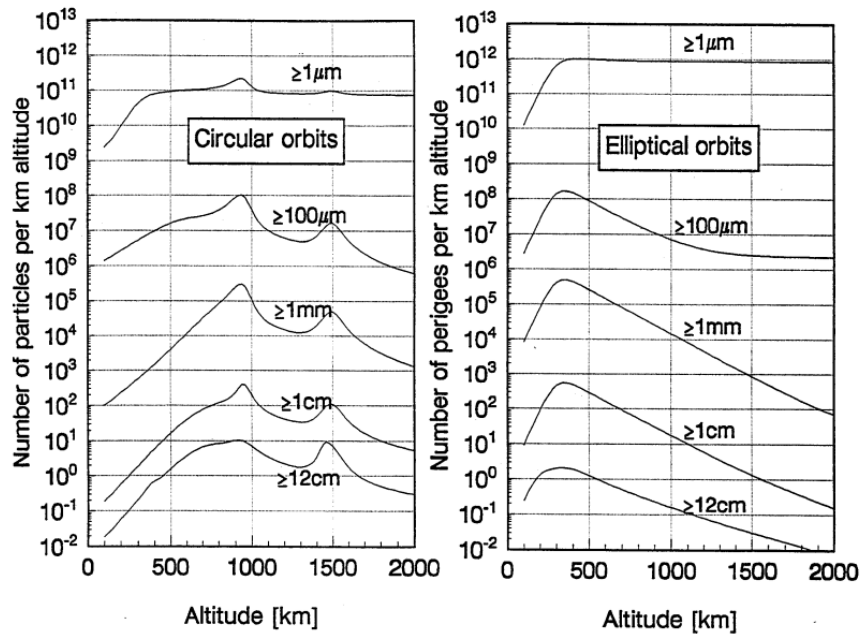
Figure 5.8: Modeled number density of particles as a function of altitude using ORDEM96 [20].

The deployment of a new space surveillance radar, known as the Space Fence, by the U.S. Space Force in March 2020 has significantly enhanced the capability to track medium-sized objects. Additionally, the private company LeoLabs has recently completed the Kiwi Space Radar and Costa Rica Space Radar, which are designed to catalogue objects as small as 2 cm in size.

It is crucial to differentiate between physical size and radar cross-section (RCS), which measures the target's image on radar. For radar wavelengths substantially smaller than the object's characteristic dimension, RCS is frequency-independent and corresponds to the physical cross-section. However, determining the RCS of an object as a function of its geometry, electromagnetic properties, and frequency is typically complex, except for specific cases such as a perfectly conducting sphere.

In electromagnetism, the Mie solution to Maxwell's equations is used to describe the scattering of an electromagnetic plane wave by a homogeneous sphere.

The values calculated from Mie scattering theory are shown as a solid curve (Figure 5.9), approximated in the Rayleigh region by

$$\sigma = \frac{9\pi^5 d^6}{4\lambda^4}.$$

(5.1)

When the diameter of a sphere exceeds approximately 0.2 times the wavelength (λ), the radar cross-section begins to oscillate around the optical approximation

$$\sigma = \frac{\pi}{4}d^2,$$

(5.2)

and the oscillations dampen to less than ±1 dB for $d \geq 2\lambda$.

58
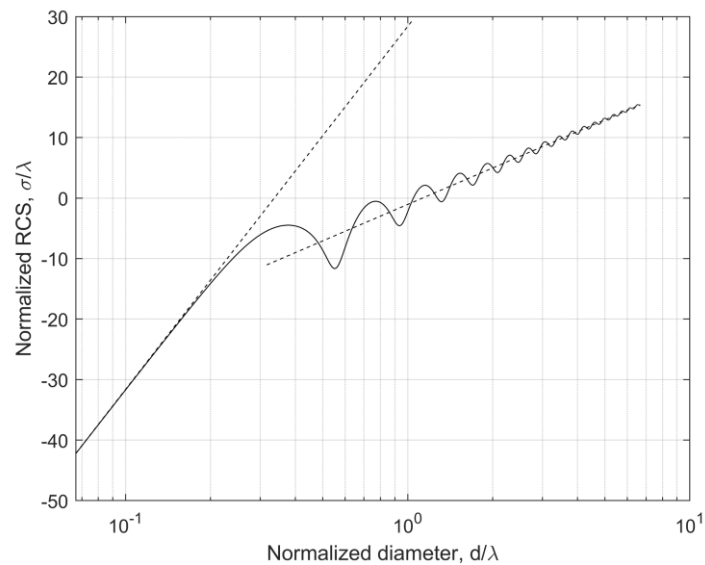
Figure 5.9: Radar cross section (RCS) of a perfectly conducting metal sphere as a function of frequency.

While this specific result pertains to a particular scenario, NASA has demonstrated that the radar cross-section for debris particles can be approximated by smoothing the oscillations of the resonant region and connecting the data points to the straight-line segments in the Rayleigh and optical regions, as illustrated in Figure 5.10. The solid curve in the graph is referred to as the size estimation model (SEM). To establish this function, the NASA research team selected a set of 44 objects gathered from two hypervelocity impact shots on satellite mockups conducted at AEDC and some debris-like objects collected by the research team [14]. The RCS of these objects was measured over four radar frequency bands: 2.56-3.92 GHz, 4.12-7.986 GHz, 8.15-12.77 GHz, and 12.92-17.54 GHz, each with eight steps in the band for the lowest frequency and 16 steps in the band for the other three. The measurements were taken at approximately 200 source-object orientation angles [36].
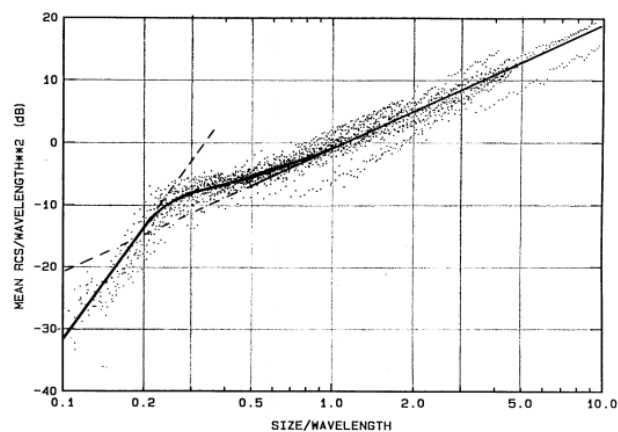
Figure 5.10: SEM curve based on measured RCS data [36].

The Size Estimation Model (SEM) curve primarily captures the sphere's response in the resonance region, where traveling waves on the surface either reinforce or cancel each other out. However, it does not encompass the complete response of the sphere. It is important to

59

note that irregularly shaped objects will exhibit more complex responses than spherical ones. Thus, the SEM curve serves as a statistical calibration curve for the reduction of measured data. The Mie curve will play a crucial role in determining radar design parameters, particularly in the selection of the carrier frequency, as discussed in the following chapter.

Chapter 6 : Radar design

6.1 Radar geometry

6.1.1 Fence elevation

The initial sections of the study were dedicated to optimizing the radar beam's elevation. This examination remained largely indifferent to radar parameters like frequency and bandwidth, prioritizing an ideal elevation drawn from the accuracy profile, independent of accuracy values. In essence, the key influencers of the profile were range, which influences SNR and hence the precision of measurements, and the correlation between those measurements. These elements are affected by radar geometry, and modifications in other radar parameters alter the orbit determination's precision but not its profile in relation to elevation angle.

Two distinct approaches were adopted to ascertain the optimal elevation angle, with their respective outcomes summarized in Figure 6.1. The first method relied on propagating the initial detection to the subsequent one. The inherent flaw in this technique lies in the propagation process itself, which necessitates an orbit determination already from the first sensor, which as it will be seen in the last chapter is possible with multiple detections. The second model offers the advantage of simulating radar performance with straightforward equations, avoiding any constraints on the target's orbit. However, the results are less accurate due to the non-linearity of the problem. For this reason, the first method will be employed to choose the optimal elevation for the double-fence configuration.
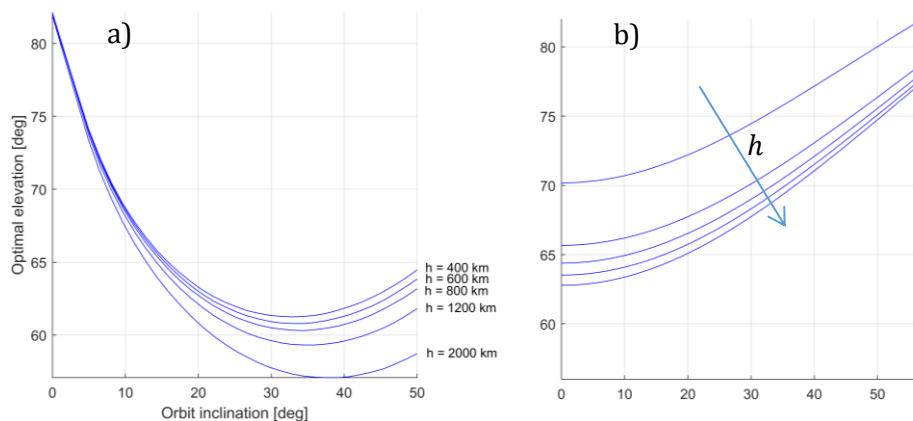
Figure 6.1: Comparison of the optimal fence elevation analyzed using two different approaches, described in Chapter 3 (a) and Chapter 4 (b).

The configuration explored in both approaches is a double-fence radar located on the equatorial plane, with the bisector of the two fences being perpendicular to this plane. This setup is effective in detecting orbits with low inclination. However, an analysis of the object population in Low Earth Orbit (LEO) indicates a concentration in high inclination orbits. Therefore, a more suitable configuration would entail a bisector parallel to the equator, which can be achieved by rotating the system 90 degrees around the axis pointing from the Earth

center to the radar location. The results derived from the previous chapters can be easily adapted to this new configuration by applying the following transformation to the orbital inclination:

$$i_2 = 90° - i_1 \,.$$
(6.1)

The optimal elevation for the new configuration is depicted in Figure 6.2, which portrays the optimal elevation for orbit inclinations ranging between 40° and 90°. This profile remains consistent for greater orbit inclinations due to the fact that the only difference between an orbit with inclination i and an orbit with inclination $180° - i$, is the direction of motion – prograde or retrograde. However, this is not entirely accurate if the Earth's rotation is considered. In one instance, the radar tends to move further away from the object in the case of a prograde orbit, and closer in the case of a retrograde orbit. Despite this, the effect is negligible given the small-time interval between the two detections and the Earth's rotation only spanning a few degrees.
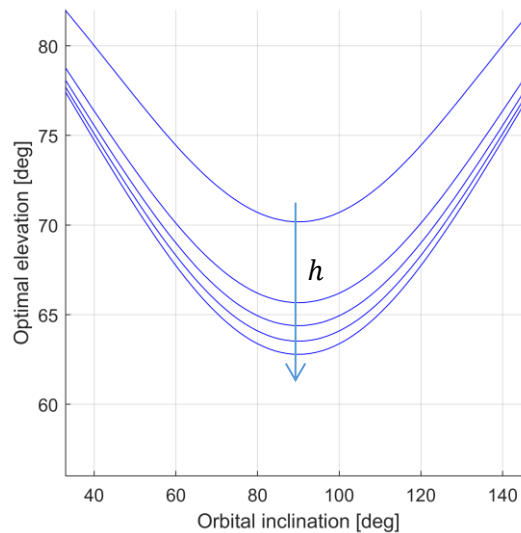
Figure 6.2: Optimal fence elevation for a configuration having the bisector parallel to the orbital plane.

The average inclination from the analyzed catalog is 78.56°, and the average altitude is 822 km. With this data, it can be deduced that the optimal elevation is 67° based on the curve depicted in the Figure 6.2.

6.1.2 Fence cross-elevation width

The width of the electromagnetic fence influences various aspects of radar performance. Primarily, the minimum detectable inclination is influenced by this parameter, as is the likelihood of an object crossing the field of view. A broad fence increases radar coverage along the longitude and enables tracking of objects with minor orbital inclinations. Initially, it may seem that a wide fence only offers advantages; however, there are technical constraints related to the scanning area. The efficiency of this antenna arrangement is most pronounced in the principal direction perpendicular to the antenna field. Excessive tilting of the main direction amplifies the number and size of unwanted sidelobes while concurrently diminishing the

gain [15]. Phased-array radars typically possess a limited scanning range, usually restricted to only 120°. It is significant to note that an extensive field of regard in the cross-elevation direction may result in an object orbiting at a specific altitude crossing the fence at one of its borders, thereby yielding a range much greater than the altitude.

However, in the present study, the maximum achievable scanning range is considered, which is 120°, to maximize coverage. The consequences of this choice are analyzed, commencing with the maximum and minimum ranges that an object can have as a function of orbital altitude. The results are presented in the Figure 6.3. The minimum range is achieved when the object crosses the fence at its midpoint, while the maximum range is attained when the object crosses the fence at its extremes.
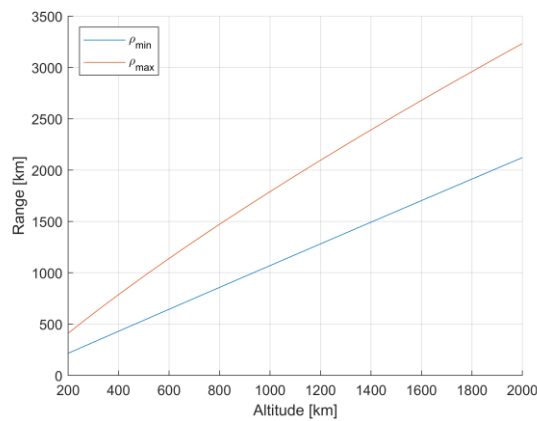
Figure 6.3: Maximum and minimum target range as function of the orbit altitude.

Regarding the minimum detectable inclination, it can be computed from the scenario illustrated in Figure 6.4. In this case, the object crosses the first fence at one of its extremes and then the second fence at its opposite end. It is important to note that this analysis applies only to the specific configuration where the bisector of the V-shape configuration is parallel to the equator and the Earth's rotation is not taken into consideration. In reality, Earth's rotation could affect the inclination range covered, either increasing or decreasing it, depending on whether the orbit is prograde or retrograde.
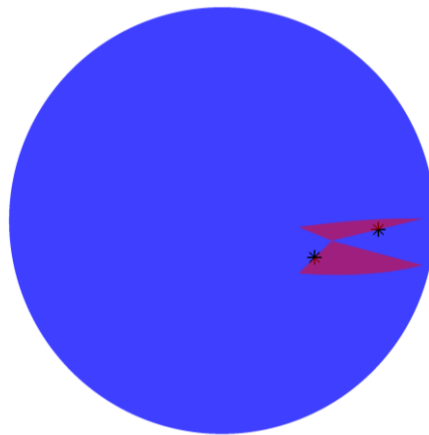
Figure 6.4: Detection of targets in the event of an orbit with the minimum detectable inclination.

In this particular scenario, the minimum detectable inclination can be determined based on the two detections. This is calculated using the Equations (4.7) and (4.8). The resulting values are presented in Figure 6.5, where various scanning angles and radar latitudes are analyzed. It is apparent that a radar positioned at a higher latitude would enhance the minimum detectable inclination. Naturally, this value will always be greater than the radar's latitude.
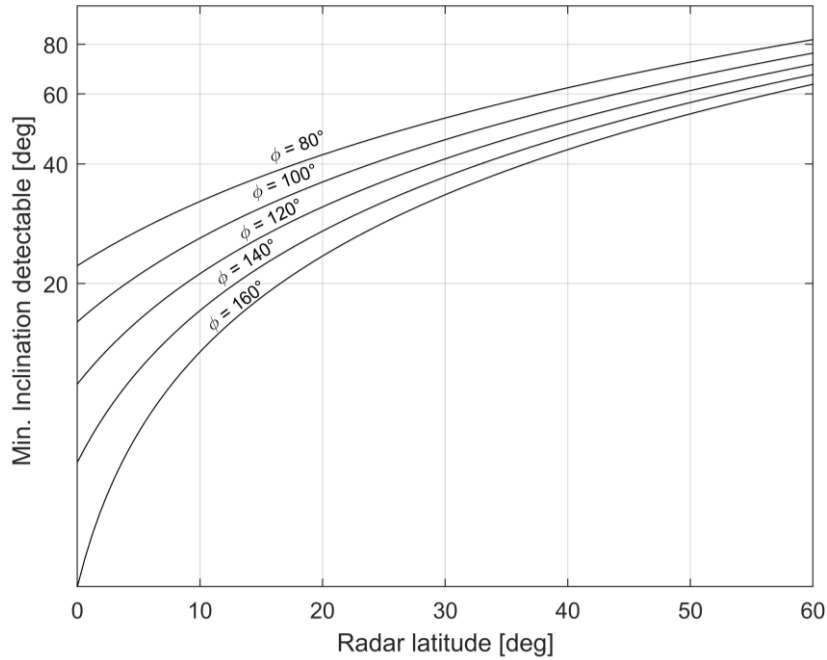
Figure 6.5: Minimum inclination detectable as function of the radar scanning angle and the latitude.

The last aspect to consider is the radar system's coverage. Intersecting the radar field of regard with a sphere of a diameter equal to the Earth's radius plus a certain altitude, centered at the Earth's center, provides the radar coverage in latitude and longitude for the given orbit altitude. An example is shown in the Figure 6.6, where the ground-track of a satellite with an altitude of 825 km and inclination of 98° is plotted alongside the radar field of regard at the same altitude. After one period, the right ascension longitude changes due to the Earth's rotation by an angle equal to

$$\Delta\lambda = \omega_E T, \tag{6.2}$$

where ω_E is the Earth's angular speed and T is the orbital period. This holds true when disturbances are neglected. This value is a function of the orbit altitude, as is the radar coverage $\Delta\lambda_{rad}$. Conversely, the time for an object to have the ascending and descending nodes for different revolutions, spanning the entire interval of longitude, does not depend on the altitude, but it is only related to the Earth's rotation, and it is equal to about 12 hours, half the revolution period. Therefore, if the radar's longitude coverage is larger than $\Delta\lambda$, each object orbiting at that altitude will cross at least one of the fences in 12 hours.

For example, this does not happen for an orbit altitude of 825 km, given the configuration studied. In fact, the radar coverage is smaller then $\Delta\lambda$ and the target could not cross the fence,

and considering the RAAN to be random, the probability of tracking every half Earth rotation could be calculated as follows:

$$p_t = \begin{cases} \dfrac{\Delta\lambda_{rad}}{\Delta\lambda}, & \text{if } \Delta\lambda_{rad}/\Delta\lambda < 1 \\ 1, & \text{if } \Delta\lambda_{rad}/\Delta\lambda > 1 \end{cases} . \qquad (6.3)$$
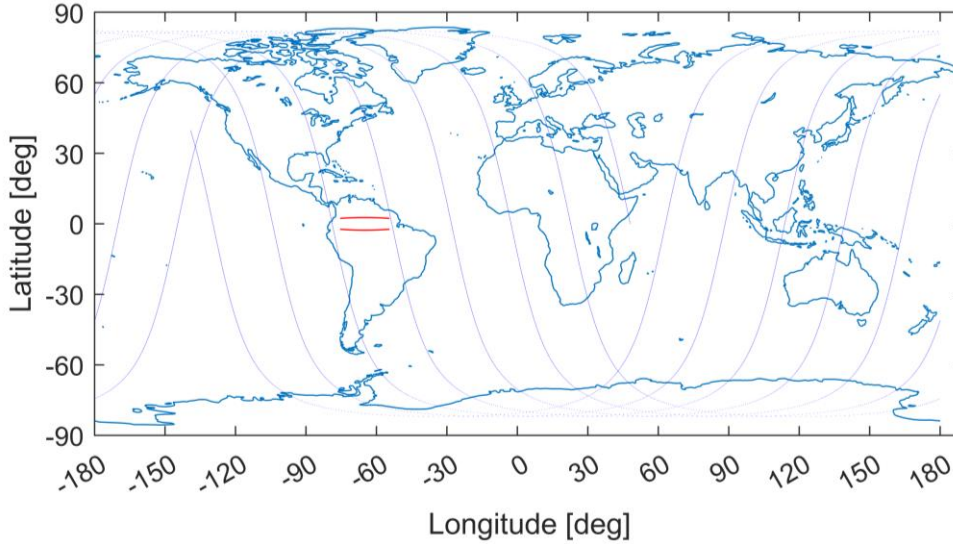
Figure 6.6: Radar field of regard for orbit altitude of 825 km,
and ground-track of a satellite with an altitude of 825 km and inclination of 98°.

Figure 6.7 illustrates the tracking probability as a function of the mean orbit altitude. For an object orbiting at an altitude of 825 km, the likelihood of being tracked within a 12-hour interval is approximately 0.82. For orbits with altitudes higher than 1170 km, they invariably intersect the radar's field of regard at least once every half Earth's rotation, assuming their orbit inclination exceeds the minimum radar threshold.
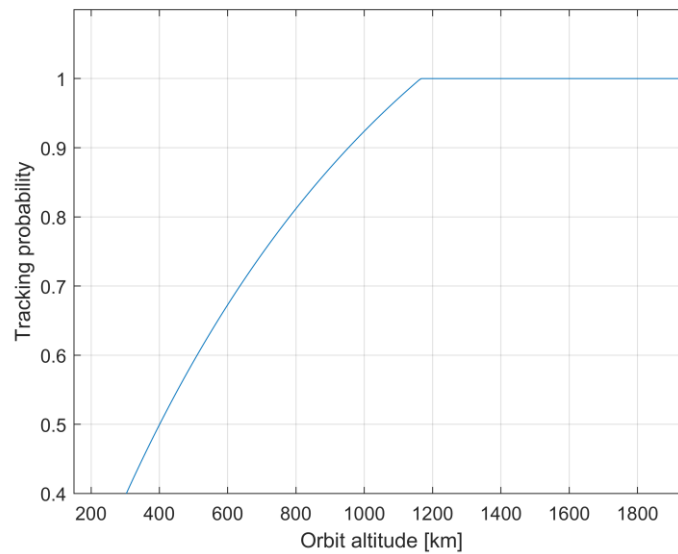
Figure 6.7: Radar tracking probability as a function of the mean orbit altitude.

6.2   Design scenario

The process of optimizing radar parameters, including pulse repetition frequency, pulse width, and antenna beamwidth, is commonly referred to as "radar parameter optimization." This process aims to refine the radar's performance while accounting for various constraints such as desired range, resolution, and power consumption. This task involves defining a design scenario that encapsulates specific conditions or requirements under which radar parameters are to be designed.

Analysis of Low Earth Orbit (LEO) objects reveals that the 750-900 km altitude band, with a representative altitude of 825 km, contains a substantial portion of the objects. Moreover, the objective is to track objects ranging in size from 1 to 10 cm due to their elevated risk of collision. Consequently, the radar is designed to detect and track objects with a size of 2 cm and orbiting at an altitude of 825 km. This means that the radar should be capable of detecting objects that cross the fence at its extremes, specifically at a range of 1515 km. However, the radar should also be capable of tracking objects across the entire LEO region (200-2000 km). Nevertheless, as the population of satellites and debris is small below 300 km, due to orbital decay, the radar is designed to detect objects with a minimum range of 300 km.

Regarding the maximum unambiguous range, the chosen value is around 3300 km, which is the maximum range an object can have when crossing the fence's extreme at an altitude of 2000 km. Another significant constraint is the power used to feed each array element, which should not exceed 500 W to avoid Intermodulation Distortion (IMD). High-power operation can result in non-linear behavior in the array's components, leading to IMD. This phenomenon occurs when high-energy signals interact with each other, generating additional frequencies, which are not present in the original signals. Furthermore, high power levels in each element can cause significant heat dissipation, necessitating appropriate thermal management to prevent degradation or failure of the array.

6.3 Radar parameters

A radar design cannot prescind from the study of its parameters and its performance, bearing in mind that the final goal is to provide a simulation of the system capabilities. The first step regards the requirements definition.

The primary requirements for a radar system include probability of detection, probability of false alarm, range resolution, required target cross section, maximum unambiguous range, and velocity. A typical radar system aims to operate with a detection probability of 0.9 and a probability of false alarm of 10^{-6}. In this scenario, due to the small radar's field of view, the system is designed to have a detection probability of 0.99. In this case the required signal-to-noise ratio for a single pulse of a steady sinusoidal signal in Gaussian noise with no detection losses is 14.51 dB [5]. This result is typically derived assuming a white Gaussian noise, which is consistent with thermal noise. However, once this noise passes through a narrowband filter, the probability density function (PDF) of the envelope of the noise voltage output takes on the form of the Rayleigh probability density function [5]:

$$p_N(x) = \frac{x}{\sigma^2} e^{-\frac{x^2}{2\sigma^2}},$$

(6.4)

where σ^2 is the variance of the noise voltage.

If a signal of amplitude A is present along with the noise, the resulting PDF is described by the following equation:

$$p_{SN}(x) = \frac{x}{\sigma^2} e^{-\frac{x^2+A^2}{2\sigma^2}} I_0\left(\frac{xA}{\sigma^2}\right)$$

(6.5)

where $I_0(Z)$ modified Bessel function of order zero and argument Z. Figure 6.8 shows the shape of the two distributions.
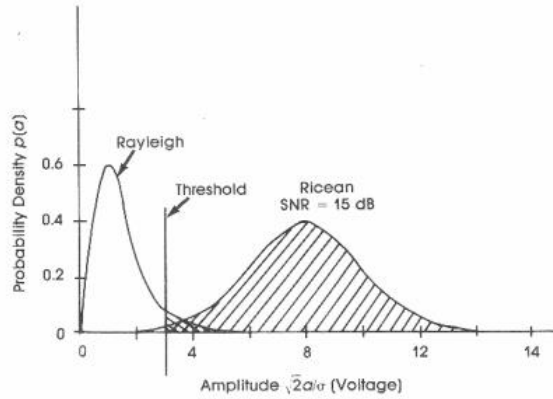
Figure 6.8: PDFs of noise and signal-plus-noise with threshold shown for $P_{fa} = 10^{-2}$.

As such, given a specific probability of detection and the probability of false alarm, one can calculate the required signal-to-noise ratio. In this scenario, the following requirements are employed:

- $p_d = 0.99,$
- $p_{fa} = 10^{-6}.$

6.3.1 System noise temperature

The noise figure of a radar system serves as a crucial performance metric, with several parameters contributing to its calculation [7]:

- Antenna Noise Figure (T_{ant}): Accounts for various scene effects including the noise temperature of the sky, Sun, and other galactic sources, as well as radome losses, and ohmic resistance of the antenna itself, including side lobes directed towards the ground.
- Transmission Line Noise Contribution (T_{Ω}): Includes all ohmic losses between the antenna and Low-Noise Amplifier (LNA), such as feed-lines, adaptors, and circulators.
- Internal Antenna Effects Noise Temperature (T_{int}): Primarily governed by the Low-Noise Amplifier (LNA) within the system.

For space situational awareness (SSA) radar systems, where the noise temperature of the sky can be below 50 K and the antenna temperature can reach up to 100 K, the typical feed line components like plugs and adapters. Collectively, these factors sum up to less than 1 dB for an L-Band system. Additionally, the typical values for LNA noise figure (T_{rec}) in an L-Band system fall between 0.7 and 1.4 dB [7]. Considering an antenna temperature of 100 K and noise figures of 1 dB and 0.7 dB for the transmission line and the LNA respectively, the system noise temperature would be approximately 225 K. This aligns with the noise temperatures of other radar systems employed in SSA applications, such as the new GESTRA radar boasts a system noise temperature lower than 110 K [26].

6.3.2 Radar losses

The radar equation (1.4) introduced in the first Chapter allows for the computation of the signal-to-noise ratio for a single pulse received by the radar. However, it does not account for the various losses that the system may experience:

- Beam-shape loss: this term describes the loss experienced as the radar's beam scans across a target, resulting in varying signal amplitudes during coherent or non-coherent integration. The full integration gain cannot be realized due to this loss.
- Scan loss: this term represents the reduction in gain and effective aperture area due to beam scanning, described by the equation (1.14).
- Atmospheric losses: these are caused by atmospheric absorption and depend on the radar's operating frequency, target range, and the target's elevation angle relative to the radar. In clear weather conditions, these losses are insignificant at frequencies below 3 GHz.
- Transmit line losses: these occur in the waveguides and other components between the power amplifier and the antenna, usually amounting to 1-2 dB in a well-designed radar.
- Receive losses: they are included in the noise figure.

The power equation for 1-D beam shape loss for an antenna with a Gaussian pattern, L_b, is [3]:

$$L_b = \sqrt{\frac{8\ln(2)}{\pi}}. \qquad\qquad (6.6)$$

Regarding atmospheric losses, the MATLAB function "tropopl" is used which calculates the path loss L in dB due to tropospheric refraction using the International Telecommunication Union (ITU) standard atmospheric model known as the Mean Annual Global Reference Atmosphere (MAGRA), which approximates the U.S. Standard Atmosphere 1976 with insignificant relative error [19]. It is important to note that the first absorption band, around 23 GHz, is significantly higher than the radar's typical frequency limit. As a result, the K-band should be avoided in radar design.
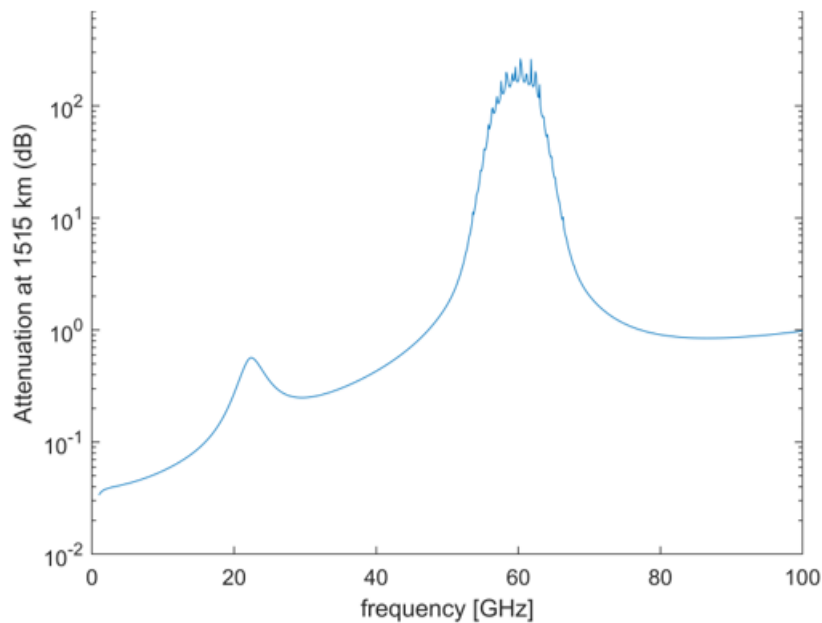
Figure 6.9: Atmospheric losses at an altitude of 1515 km as function of the frequency.

6.3.3 Radar signal

The system requirement dictates the detection of objects sized 2 cm, orbiting at an altitude of 825 km, with a detection probability of 0.99 and a false alarm rate of 10^{-6}. Simultaneously, the radar should have the capability to detect objects orbiting within an altitude range of 300 km to 2000 km. This latter requirement enables the computation of the minimum detectable range and the unambiguous range, factoring in the system's geometry. Figure 6.3 illustrates the minimum and maximum detectable ranges for a given orbit altitude. According to the graph, the minimum range for a 300 km altitude orbit is 323 km, while the maximum range for a 2000 km altitude orbit is 3234 km. For a monostatic radar, the minimal measuring range R_{min} (referred to as the "blind range") represents the minimum distance at which a target must be detectable. This necessitates that the transmitting pulse completely clears the antenna, and the radar unit activates the receiver, a process linked to the pulse duration τ:

$$R_{min} = \frac{c\tau}{2}. \tag{6.7}$$

Since R_{min} in this case should be smaller than 323 km it follows that

$$\tau < \frac{2R_{min}}{c} = 2.15 \ ms \ . \tag{6.8}$$

Conversely, the maximum unambiguous range (R_{max}) refers to the farthest distance a transmitted pulse can travel round trip between consecutive pulses while still providing reliable information. In essence, R_{max} represents the limit of radar energy travel between pulses. The relationship between the Pulse Repetition Frequency (PRF) or its reciprocal value, the interpulse period (PRT), and R_{max} determines the radar's unambiguous range. Suppose the radar emits a pulse that strikes a target and returns to the radar in round trip time t:

- If $t < PRT$, then the return signal arrives before the next pulse is emitted.
- If $t = PRT$, then the return signal arrives exactly as the next pulse is emitted.
- If $t > PRT$ PRT, then the return signal arrives after the next pulse is emitted, introducing ambiguity. The radar cannot distinguish whether the return signal originates from the first or second pulse.

Therefore, the maximum unambiguous range R_{max} represents the maximum range for which $t < PRT$:

$$R_{max} = \frac{c(PRT - \tau)}{2}. \tag{6.9}$$

Since R_{max} in this case should be larger than 323 km it follows that

$$PRT > \frac{2R_{max}}{c} + \tau = 21.6 \ ms + \tau. \tag{6.10}$$

Different combinations of PRT and τ can be selected. A possible solution is $\tau = 2 \ ms$ and a pulse repetition frequency (PRF) of 45 Hz which determines a PRT of around 22 ms. The duty cycle in this case is equal to 9%.

Regarding the carrier frequency, it holds significant importance in determining the power of the received signal, as demonstrated in Equation (1.4). This equation can be reformulated by considering the correlation between debris size and radar cross-section:

$$\sigma = \begin{cases} \dfrac{9\pi^5 d^6}{4\lambda^4} \ , & d < 0.2\lambda \\ \dfrac{\pi d^2}{4} \ , & d > 1.2\lambda \end{cases} . \tag{6.11}$$

Since the power received, and therefore the signal to noise ratio is proportional to the product $\sigma\lambda^2$, it follows that:

$$P_r \sim \sigma\lambda^2 \sim \frac{1}{\lambda^2} \sim f_c^2 \tag{6.12}$$

in the Rayleigh region, while in the optical region

$$P_r \sim \lambda^2 \sim \frac{1}{f_c^2}, \tag{6.13}$$

where f_c is the carrier frequency. It implies that with a constant transmitting power, antenna gain, and debris size, the SNR increases with higher carrier frequencies, whereas the opposite trend is observed in the optical region. In the transition between these two regions, the slope of the curve, as depicted in the Figure 6.10, is smaller compared to the slope in the optical region. This indicates that in the intermediate region, the SNR decreases less rapidly than in the optical region. Frequency bands within the microwave range are typically designated by letters. This convention originated around World War II with military classifications for frequencies utilized in radar systems, which were the initial applications of microwaves (source: https://en.wikipedia.org/wiki/Radio_spectrum). The frequency bands are detailed in the accompanying Table 6-1: Radio frequency bands..

Table 6-1: Radio frequency bands.

Band designation	Frequency
VHF	0.03 to 0.3 GHz
UHF	0.3 to 1 GHz
L	1 to 2 GHz
S	2 to 4 GHz
C	4 to 8 GHz
X	8 to 12 GHz
Ku	12 to 18 GHz

Figure 6.10: Normalized RCS as function of the normalized sphere diameter, with the region referred to the radar bands for a 2 cm diameter sphere highlighted. illustrates the region in which different frequency bands fall, assuming a debris size of 2 cm. It is apparent that the boundary for the Rayleigh region lies within the S-band, approximately at 3 GHz, whereas both the C and X-bands entirely reside within the transition region. Hence, an optimal selection for the carrier frequency would be 3 GHz. This choice yields a radar cross-section for a 2-cm debris size equal to -34.11 dBsm.

After determining the pulse width, carrier frequency, system noise temperature, and radar losses, along with the target information, the last step involves calculating the peak power and gain to achieve the required signal-to-noise ratio for the specified probability of detection and false alarm rate. The SNR can be expressed using Equation (1.4) as:

$$SNR = \frac{P_{tx}G^2\lambda^2\sigma\,M\,\tau}{(4\pi)^3\rho^4 k_B T_S}, \tag{6.14}$$

with M the number of coherently integrated pulses. In order to generate different detections inside the beam, and to allow to integrate coherently the pulses, $M = 3$ is chosen.

With most parameters defined, the remaining unknowns are the transmitted peak power and the antenna's gain. Both parameters can be expressed as functions of the number of elements comprising the linear array N:

$$P_{tx} = N \cdot P_{el}, \tag{6.15}$$

$$G = \frac{4\pi}{\lambda^2}D_w D_l = \frac{4\pi}{\lambda^2}D_w N d, \tag{6.16}$$

where d is the distance between the antenna elements, which is half of the wavelength, namely 5 cm. The product $P_{tx}G^2$ can be written as:

$$P_{tx}G^2 = SNR\frac{(4\pi)^3\rho^4 k_B T_S}{\lambda^2\sigma\,M\tau} = a, \tag{6.17}$$

and it is a constant since all the parameters on the right side are defined. The same product can also be written as function of N:

$$P_{tx}G^2 = P_{el}\left(\frac{4\pi}{\lambda^2}D_w d\right)^2 N^3 = bN^3. \tag{6.18}$$

In this equation, b represents a constant once P_{el} and D_w are defined. It is advantageous to use the maximum power that a single element can withstand, which in this study is set at 500 W. This approach allows for reducing the antenna dimensions and, consequently, the costs associated with it. The antenna width D_w is a design parameter, influencing the beamwidth in the elevation direction. A smaller width would increase the beamwidth, thus improving the elevation resolution and accuracy. This would also lead to a longer dwell time within the field of view, allowing for more detections. Conversely, a larger width would increase the gain for the same array length while decreasing the beamwidth. This trade-off will be the subject of study in the next chapter. Figure 6.11 illustrates the number of elements as a function of the elevation beamwidth. It is evident that increasing the elevation beamwidth requires compensating for the loss in gain by reducing the beamwidth in the cross-elevation direction. This necessitates a longer phased array and an increase in transmitting power. Conversely, the area of the reflector, approximated by $D_l D_w$, exhibits the opposite trend, as depicted in Figure 6.12.
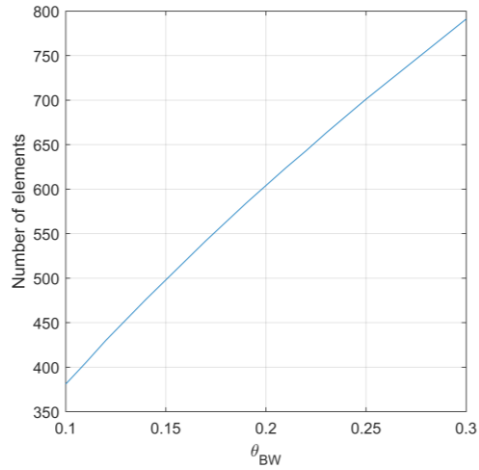
Figure 6.11: Number of elements composing the linear phased array as function of the elevation beamwidth.
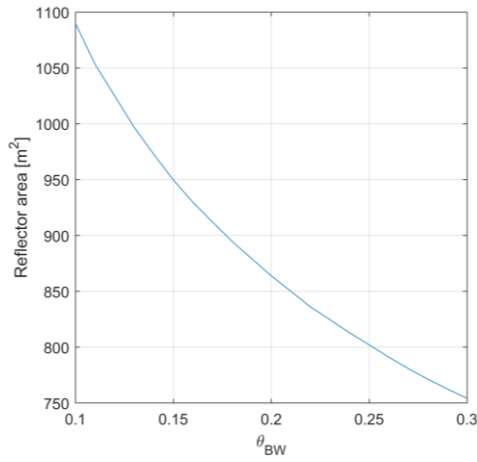
Figure 6.12: Approximated area of the antenna reflector as function of the elevation beamwidth.

The goal is to calculate the number of elements of the phased array necessary to achieve the desired signal-to-noise ratio. This can be achieved by combining equations (6.17) and (6.18):

$$N = \sqrt[3]{\frac{a}{b}}. \tag{6.19}$$

Subsequently, the antenna transmitting power and its gain can be computed from equations (6.15) and (6.16), along with the beamwidth in the two directions.

Another critical radar parameter is the signal bandwidth, which directly affects radar performance in terms of range resolution, Doppler resolution, clutter rejection, interference mitigation, and frequency agility. A more precise design of the signal processing would enable the definition of a range of values for this parameter. However, for this preliminary design, the bandwidth value is adopted from the Kiwi-Space radar parameters [24], specifically set at 10 MHz.

Chapter 7 : Radar performance

This chapter delves into simulating the radar system introduced in the preceding chapter across various scenarios, incorporating an examination of the distribution of Keplerian elements for objects in Low Earth Orbit (LEO). The simulation leverages MATLAB's "Sensor Fusion and Tracking Toolbox," enabling the creation of a radar system and the generation of detections for objects traversing the radar field of regard. In addition to defining the FOR, several radar parameters require specification:

- Radar update rate: the frequency at which the radar produces new reports.
- Location: latitude, longitude, and altitude (LLA system) of the radar.
- Mounting angles: intrinsic Euler angle rotations of the sensor around the z-axis, y-axis, and x-axis relative to the platform body frame.
- Center frequency: critical for atmospheric refraction, denotes the center frequency of the radar band.
- False alarm rate: rate of false alarm reports within each radar resolution cell.
- Probability of detection: likelihood of detecting a target with a radar cross-section (RCS) at the reference detection range.
- Reference range: the range associated with the given probability of detection and reference RCS.
- Reference RCS: the RCS corresponding to the given probability of detection and reference range.
- Range limits: minimum and maximum range of the radar, beyond which targets are undetectable.
- Measurement resolution: elevation, cross-elevation, and range resolution of the radar.
- Measurement bias: fixed elevation, cross-elevation, and range bias expressed as function of the resolution. A value of 0.1 is employed for the range and 0.01 for elevation and cross-elevation.

This study analyzes radar performance without considering range rate measurement. To establish the space fence, two radar sensors are created, each sharing identical parameters except for mounting angles. One system is rotated by 67 degrees around the y-axis in the body frame, while the other is rotated by 113 degrees.

Regarding orbiting objects, their Keplerian elements are defined, and Keplerian propagation is implemented using the fourth order Runge-Kutta method.

7.1 Radar tracking model

7.1.1 Detection model

The initial step in generating detections involves determining whether objects fall within the radar's field of regard. This necessitates expressing both object and radar positions in the same coordinate frame. An optimal choice for this is the Earth-centered, Earth-fixed coordinate system (ECEF), also referred to as the geocentric coordinate system (Figure 7.1). In the ECEF system, a Cartesian spatial reference system is utilized, with the following characteristics:

- The X-axis lies within the equatorial plane, extending from 180° longitude (negative) to the prime meridian (positive).
- The Y-axis also lies within the equatorial plane, extending from 90°W longitude (negative) to 90°E longitude (positive).

One significant advantage of this system is that the radar's location remains fixed within this frame. However, it is important to note that while the reference frame is not inertial, the object's motion model must still account for the centrifugal force resulting from the Earth's rotation and the Coriolis force.
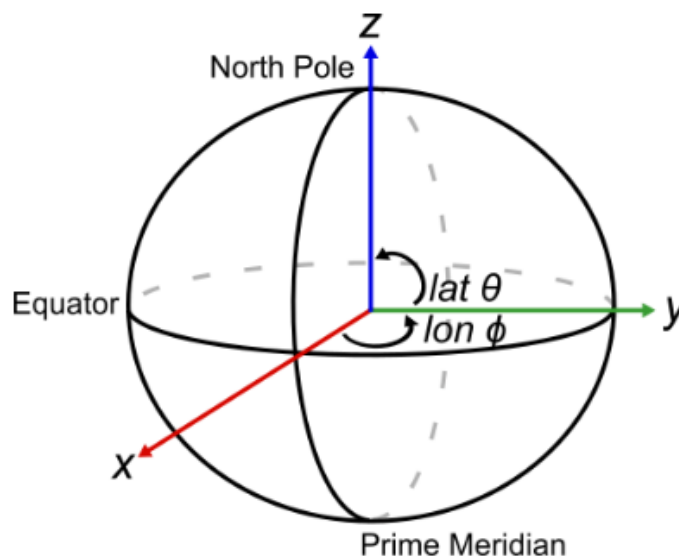
Figure 7.1: An Earth-centered Earth-fixed (ECEF) system, from [22].

The radar input is derived by calculating the disparities between the satellite's position and the ground station's position, followed by rotating these disparities into the local North-East-Down (NED) axes of the ground station. This process provides information on the spherical coordinates of the targets.

Within the MATLAB toolbox, an atmospheric model is incorporated to adjust for atmospheric refraction, which causes the radar to perceive the target at slightly altered positions in terms of elevation and range compared to their actual positions. Initially, the script filters out all objects lying outside the specified range limits to streamline the subsequent processing. Subsequently, it verifies whether the remaining objects fall within the sensor's field of regard.

If any objects are detectable by either of the two sensors, a detection vector can be defined, containing the adjusted range and elevation.

Furthermore, the script computes the signal-to-noise ratio for each detection. This is facilitated by calculating the radar loop gain, which is derived from the probability of detection, the reference range (ρ_{ref}), and the reference radar cross-section (σ_{ref}):

$$RLP_{dB} = SNR_{dB,ref} + 40\log_{10}\rho_{ref} - \sigma_{dB,ref} \, , \qquad (7.1)$$

The signal-to-noise ratio for a specific target with a radar cross-section (σ) at a range (ρ) is calculated as follows:

$$SNR_{dB} = RLP_{dB} - 40\log_{10}\rho + \sigma_{dB} \, . \qquad (7.2)$$

Ultimately, the standard deviation of the error for elevation, cross-elevation and range can be determined using Equations (1.9) and (1.11). The precision is contingent upon the radar resolution for each measurement and the sensor biases, which set a lower threshold on the estimated accuracies. These biases may arise from factors such as instrumentation or timing discrepancies. A random noise is generated from the covariance noise matrix and appended to the detection vector. In the final phase, the detection is once more converted into the Earth-centered, Earth-fixed (ECEF) coordinate system, serving as input for the tracker. The schematic illustrating the logic of the radar detection model is depicted in Figure 7.2, while the different coordinate systems are described in Table 7-1.
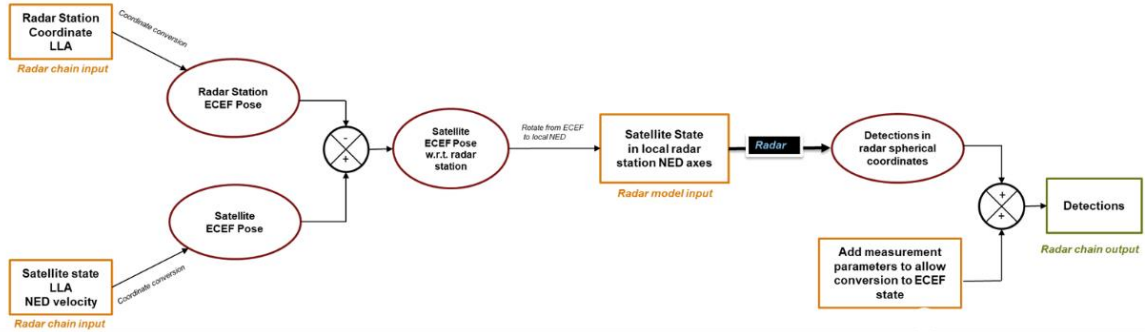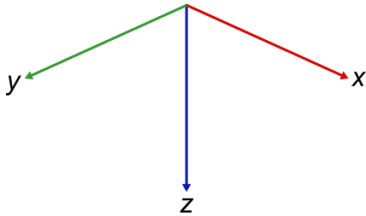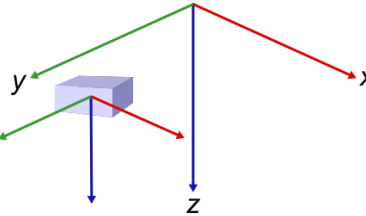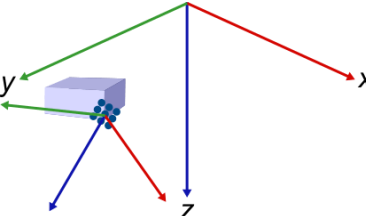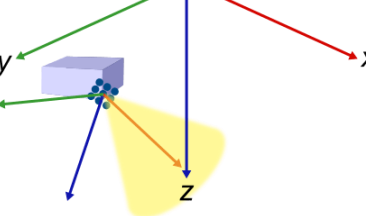
Figure 7.2: Flow-chart showing the steps to generate the radar's detections [22].

Coordinate Frame	Definition
Global Frame	A *global frame* is the highest-level frame. All other frames are referenced within it.
Body Frame	A body frame is typically centered in a platform and oriented in the same direction as the platform. Typically, the x-axis represents the forward orientation of the body. The origin of the body frame is therefore the position of the object or platform in the global frame.
Mounting Frame	A mounting frame is the frame in which the sensor is referenced and mounted. The origin and orientation of the mounting frame is a position relative to the platform.
Sensor Frame	A *sensor frame* represents the position and orientation of the sensor. For a rotating sensor: ▪ The mounting frame origin represents the position of the sensor. ▪ The sensor frame orientation represents the direction of the sensor beam relative to the mounting frame.

7.1.2 Tracking model

The radar model outlined previously produces detections. To estimate satellite orbits, a tracker is employed. In this study, a Joint Probabilistic Data Association (JPDA) tracker is utilized due to its favorable balance between tracking performance and computational efficiency. The JPDA tracker can process detections from multiple targets across multiple sensors. It utilizes joint probabilistic data association to assign detections to tracks. The tracker employs soft assignment, allowing multiple detections to contribute to each track. It initializes, confirms, corrects, predicts (coasts), and deletes tracks. The tracker's inputs are detection reports generated by the preceding algorithm. It estimates the state vector and state estimate error covariance matrix for each track. Each detection is then assigned to at least one track, and if a detection cannot be assigned to any existing track, a new track is created. A new track begins in a tentative state. If enough detections are assigned to a tentative track, its status changes to confirmed. When a track is confirmed, it is considered to represent a physical object. If detections are not assigned to a track within a specified number of updates, the track is deleted. The primary parameters for the tracker include:

- Filter initialization function: utilized for estimating the evolving state of a process when measurements are made.
- Assignment threshold: threshold used to assign a detection to a track.
- Confirmation threshold: defined by the vector $[M_c, N_c]$, a track is confirmed if it recorded at least M_c hits in the last N_c updates.
- Deletion threshold: Defined by the vector $[M_d, N_d]$, a track is deleted if there are at least M_d misses in the recent N_d updates.

An optimal filter for orbit determination is the Unscented Kalman Filter (UKF). It estimates nonlinear systems using discretely sampled points to parameterize the mean and covariance. The UKF algorithm takes noisy measurements from sensors and produces state variable estimations that are more accurate than using each measurement individually. Model and measurement approximations or noise contribute to the estimates. The filter combines a prediction of the system's state with new measurements using a weighted average, with weights derived from the covariance. This process repeats recursively using only information from the previous time step.

A track is initialized when a detection cannot be assigned to an existing track. During initialization, the state and state covariance matrix are computed, although the track remains unconfirmed. The state vector includes position and velocity components in the ECEF system. Since only position is obtained from a single measurement, velocity components are set to zero, with their standard deviation in the covariance matrix set to 10 km/s if a new object is detected, a suitable value for LEO objects. The position vector's standard deviation is set to 1 km for each component. Other track information includes detection time and track logic. Once initialized, tracks are propagated to the next time step, facilitating comparison of track states with new detections. Assignments are made using a cost matrix, with each element containing the normalized distance between track predictions and detections. The tracker can only assign a detection to a track if the normalized distance is less than the assignment threshold.

It is worth noting that the filter itself can introduce noise in orbit determination due to the motion model used for state propagation, which may differ from the real target motion. This

noise, known as process noise, is set to zero in this case, as the filter's prediction model aligns with the real target's dynamic model, namely the Keplerian orbit model.

Once a detection is assigned to a track, the state and state error covariance are corrected using the new measurement and the UKF. The inputs for the correction are:

- y: Measurement vector
- $\boldsymbol{R}$: Measurement noise covariance
- $\bar{X}$: State estimate
- $\boldsymbol{P}$: State covariance
- α, β, κ: Parameters controlling sigma points distribution
- h: Measurement function

The outputs are:

- $\hat{X}$: Corrected state
- $\hat{\boldsymbol{P}}$: Corrected state covariance

The measurements and the state are vectors, but for clarity, the apex is omitted. The concept of the Unscented Kalman Filter process is briefly outlined here, with a detailed explanation provided in [11]. When a detection y_k occurs at time t_k, all existing tracks must be updated to the time of the detection. The most recent update of the tracks occurred at time t_{k-1}. To propagate a track state, a set number of sigma points are generated around the state vector $\hat{X}_{k-1}$, which is treated as a randomly distributed variable. This process, known as the unscented transformation (UT), produces 13 sigma points $\chi_{i,k}$. The number of sigma points is given by $2n + 1$, where n is the size of the state vector, which contains the position and the velocity components:

$$\chi_{0,k-1} = \hat{X}_{k-1}$$

$$\left.\begin{array}{l} \chi_{i,k-1} = \hat{X}_{k-1} + \sqrt{(n+\lambda)\boldsymbol{P}_{k-1}|_i} \\ \chi_{n+i,k-1} = \hat{X}_{k-1} - \sqrt{(n+\lambda)\boldsymbol{P}_{k-1}|_i} \end{array}\right\} \quad i = 1, \dots, n \tag{7.3}$$

Each column of the covariance matrix $\boldsymbol{P}$ is utilized to compute the sigma points, and the scaling parameter λ is computed as follows:

$$\lambda = \alpha^2(n + \kappa) - n. \tag{7.4}$$

Subsequently, these points are propagated using the filter motion model, and the resulting propagated points $\chi_{i,k}^*$ are then combined to obtain the propagated state vector $\bar{X}_k$. The sum is weighted using the weighting factors, which are function of the tracker parameters. Also, the covariance matrix is propagated ($\bar{\boldsymbol{P}}_k$) by calculating the residues of sigma points and propagated state vector, including the process noise matrix. The UKF procedure is showed in Figure 7.3: Procedure of the UKF [10].

During the measurement update, one component involves comparing the true measurement y_k with the propagated state vector $\bar{X}_k$. Consequently, the latter needs to be transformed into the same coordinate system as the measurement. This nonlinear transformation is executed by the function h, which is applied to the new sigma point $\chi_{i,k}$, given by the state vector $\hat{X}_k$ and the covariance matrix $\bar{\boldsymbol{P}}_k$. The measurements generated ($Y_{i,k}$) are then combined using the

same weights applied to compute the state vector $\bar{X}_k$, and the results is the transformed state vector $\bar{y}_k$. Finally, the Kalman gain $\boldsymbol{K}_k$ can be computed from the covariance matrix of the transformed state vector $\boldsymbol{P}_{yy,k}$ and the cross covariance matrix $\boldsymbol{P}_{xy,k}$. The second matrix is calculated using the sigma points $\chi_{i,k}$, while the first one exploits the transformed sigma points $Y_{i,k}$ and measurement noise matrix. The Kalman filter is necessary to correct the state vector $\bar{X}_k$ and its covariance matrix, exploiting the measurement y_k:

$$\hat{X}_{k-1} = \bar{X}_k + \boldsymbol{K}_k(y_k - \bar{y}_k). \tag{7.5}$$

The block diagram of the measurement update performed by the UKF is shown in Figure 7.4.
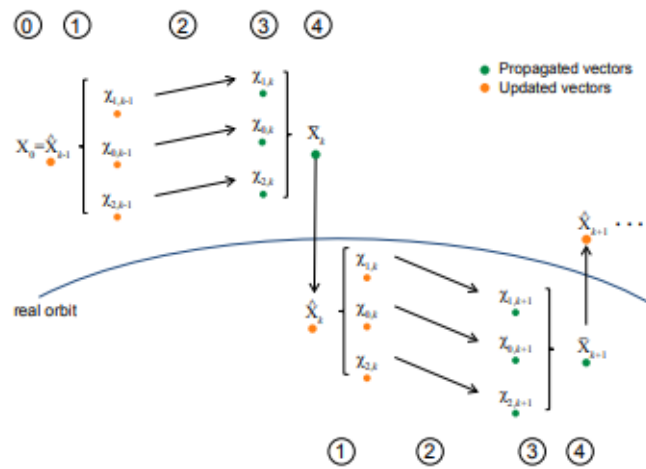
Figure 7.3: Procedure of the UKF [10].
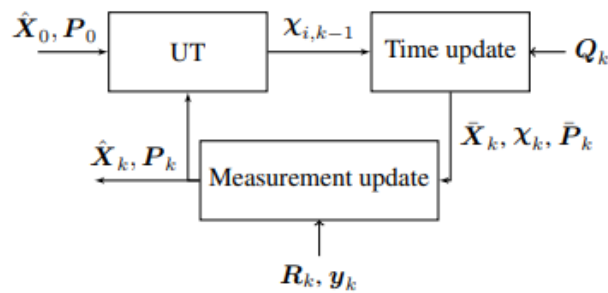
Figure 7.4: Block diagram of the UKF [10].

7.2   Radar beamwidth

7.2.1 Performance parameter

At this stage, the geometric configuration of the radar's field of regard has been precisely delineated, alongside most radar parameters. However, certain parameters, including transmitted power, gain, and beamwidth, remain contingent upon the radar's beamwidth. A strategy to optimize this parameter involves evaluating radar tracking performance using varied elevation beamwidths, using the tool described in the previous paragraph. Tracking performance is quantified via the state covariance matrix provided by the UKF subsequent to the most recent detection by radar sensors. This matrix facilitates the extraction of position and velocity component distributions under the assumption of a normal distribution. A more precise procedure entails simulating numerous tracking instances of the same object, calculating position and velocity errors relative to the actual object in each simulation. This approach extrapolates the statistical properties of state estimation. However, due to significantly higher computational costs, the focus remains on studying the covariance derived from a single simulation. The covariance matrix exhibits the following structure:

$$\boldsymbol{P} = \begin{bmatrix} \sigma_{x,x} & \cdots & \sigma_{x,vz} \\ \vdots & \ddots & \vdots \\ \sigma_{x,vz} & \cdots & \sigma_{vz,vz} \end{bmatrix} \tag{7.6}$$

This matrix allows for the extraction of sub-matrices $\boldsymbol{P}_r$ and $\boldsymbol{P}_v$:

$$\boldsymbol{P}_r = \begin{bmatrix} p_{11} & p_{12} & p_{13} \\ p_{21} & p_{22} & p_{23} \\ p_{32} & p_{32} & p_{33} \end{bmatrix}. \tag{7.7}$$

$$\boldsymbol{P}_v = \begin{bmatrix} p_{44} & p_{45} & p_{46} \\ p_{54} & p_{55} & p_{56} \\ p_{64} & p_{65} & p_{66} \end{bmatrix}. \tag{7.8}$$

The state vector $\vec{X}$ contains the expected values of the position and velocity vectors. Therefore, the position vector can be written as follows:

$$\begin{cases} x = X_1 + \Delta x \\ y = X_2 + \Delta y \\ z = X_3 + \Delta z \end{cases} \tag{7.9}$$

The variables Δx, Δy, and Δz follow a Gaussian distribution characterized by the covariance matrix P_r. Although the cross-variance components are not zero, indicating that the variables are not independent, the covariance matrix can be diagonalized to isolate the three independent directions and determine the variance in each of them.

$$\mathbf{P}_r^* = \begin{bmatrix} p_{11}^* & 0 & 0 \\ 0 & p_{22}^* & 0 \\ 0 & 0 & p_{33}^* \end{bmatrix}. \tag{7.10}$$

The error vector can be defined as follows:

$$\overrightarrow{\Delta r_*} = (\Delta x_*, \Delta y_*, \Delta z_*). \tag{7.11}$$

The radar performance can be characterized by the distribution of the norm of this vector, as illustrated in the figure. Deriving the probability density function of this variable can be complex. However, an upper bound for its expected value can be derived from the variance formula:

$$Var(Z) = E[Z^2] - E[Z]^2, \tag{7.12}$$

where $E[Z]$ is the expected value of Z, and $Var(Z)$ its variance. This relation can be written as:

$$E[Z]^2 = E[Z^2] - Var(Z) < E[Z^2]. \tag{7.13}$$

In this case Z^2 is the square of the norm of a random vector with Gaussian distribution, and its expected value can be easily computed:

$$E\left[\left\|\overrightarrow{\Delta r_*}\right\|^2\right] = E[\Delta x_*^2] + E[\Delta y_*^2] + E[\Delta z_*^2] = tr(\mathbf{P}_r^*). \tag{7.14}$$

The same procedure can be applied to the velocity vector. In conclusion, radar performance is defined using the square root of the trace of the diagonalized matrix.

7.2.2 Simulation

In order to compute the optimal beamwidth, it is necessary to analyze the tracking of the same object using different beamwidths. For simplicity, it is assumed that the object has zero eccentricity and a 90° inclination, allowing it to cross the field of regard of the two sensors in nearly the same region. The orbit altitude is set at 825 km, as specified in the design scenario. In this case, a known object is simulated, meaning a prior knowledge of its state is available, with an accuracy of 1 km for the position components and 100 m/s for the velocity components. To compare the different simulations accurately, the detections for each beamwidth should ideally occur at the same points. However, due to the narrower field of regard with a smaller beamwidth, fewer detections are expected. Despite this limitation, the assumption is made that the beamwidth only affects the measurement accuracy and not the detection points. Therefore, an average field of regard is considered.

An example of radar detections is depicted in Figure 7.5, where the red circles represent the radar measurements, and the blue dots indicate the actual target position. Figure 7.6 displays the target, the track estimate, and its 50-sigma covariance matrix for improved visibility. The noticeable reduction in the covariance matrix after the target crosses the second sensor's field of regard is significant.
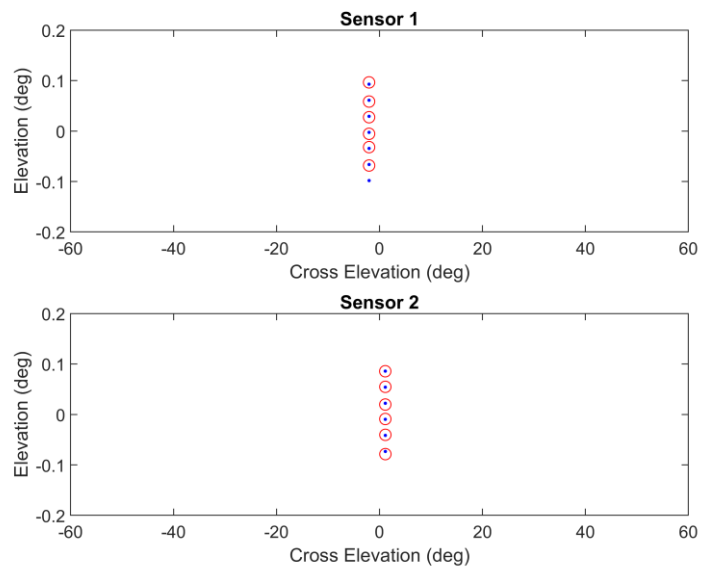
Figure 7.5: Target positions (blue dots) and the detections (red circles) from the point of view of each sensor.
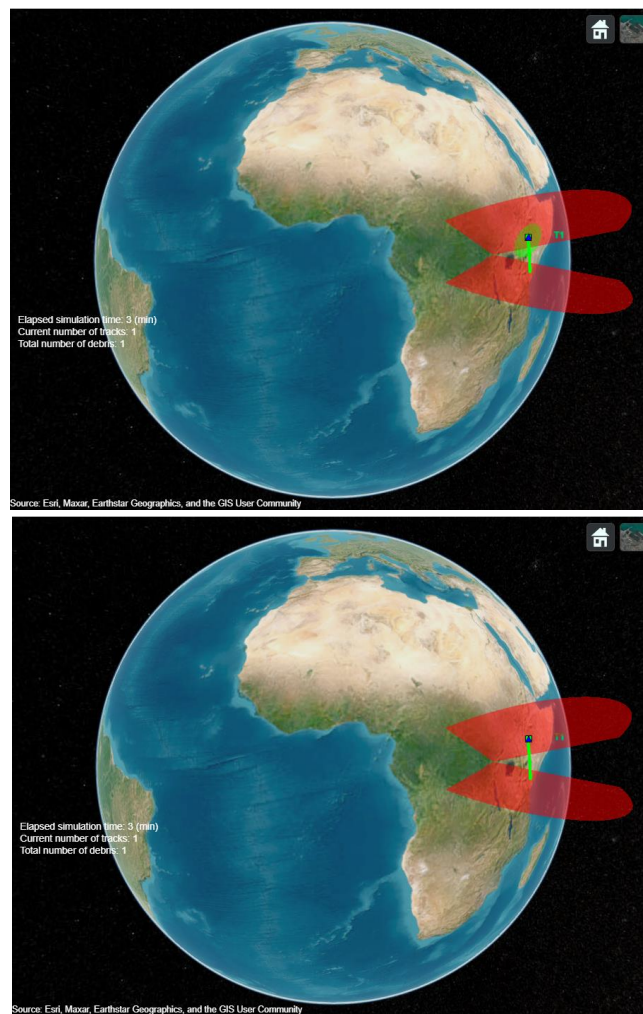
Figure 7.6: The target track (green) and its covariance matrix, before and after the second sensor detections.

The tracking performances are depicted in Figure 7.7: Position and velocity accuracy as function of θ_{BW}, for an object crossing the fence close to its center., where the irregular shape of the curve arises due to the requirement that the number of antennas composing the linear array must be an integer. Notably, it is evident that there exists an elevation angle that optimizes the performance, closely approximating the value that determines an equal beamwidth in elevation and cross-elevation. This alignment can be predicted, considering that the primary source of error is represented by the cross-range error in the two directions, which are determined by

$$\sigma_{cr,\theta} = \rho\sigma_\theta = \rho f \theta_{BW} \, , \qquad (7.15)$$

$$\sigma_{cr,\varphi} = \rho\sigma_\varphi = \rho f \varphi_{BW} \, , \qquad (7.16)$$

where f is the scaling factor, function of the SNR and the sensor bias. The total cross-range error is:

$$\sigma_{cr} = \rho f \sqrt{\theta_{BW}^2 + \varphi_{BW}^2} \, . \qquad (7.17)$$

The profile is depicted in Figure 7.7, assuming the beam is pointing at the boresight. The value of θ_{BW}, at which the minimum of σ_{cr} is achieved, closely corresponds to the optimal elevation beamwidth, albeit slightly smaller. This minor deviation can be attributed to the fact that cross-range error in the elevation direction disproportionately impacts the error in the S-component within the RSW coordinate system. Conversely, error in the cross-elevation direction primarily affects the W-component, located outside the orbital plane, leading it to oscillate rather than grow like the S-component error. Consequently, a smaller elevation beamwidth offers improved estimation after the first sensor.
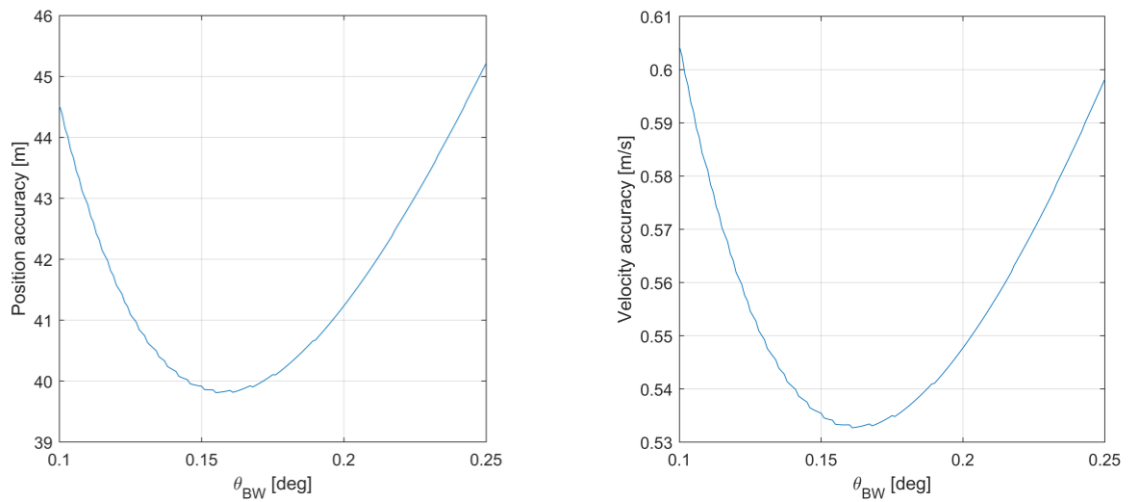
Figure 7.7: Position and velocity accuracy as function of θ_{BW}, for an object crossing the fence close to its center.
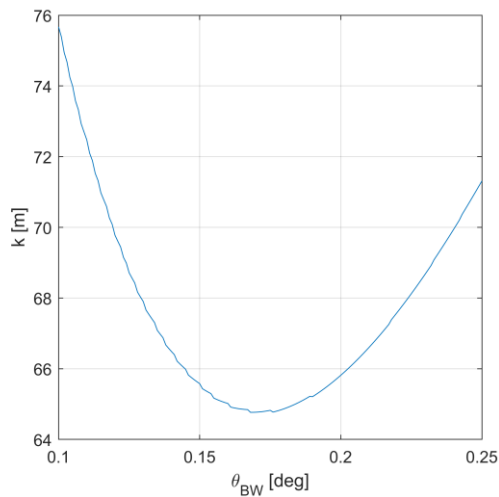
Figure 7.8: Total cross-range error as function of θ_{BW}, for an object crossing the fence close to its center.

The analysis is repeated for the same object (Figure 7.9), but this time it crosses the fence close to the edge. Due to scan losses and the larger range, the measurements are less precise, and φ_{BW} increases by a factor of $(\cos\varphi)^{-1}$. Consequently, it is expected that the optimal elevation angle this time is larger, as it needs to compensate for the scan loss, as illustrated in Figure 7.10. Since the probability for the target to cross each area of the fence is the same, a logical choice would be to use the average between the optimal value at the center and the one at the edge. However, the deterioration of accuracy at the edge due to the scan loss and the larger distance of the target from the sensors make choosing the optimal value at the edge a better choice.
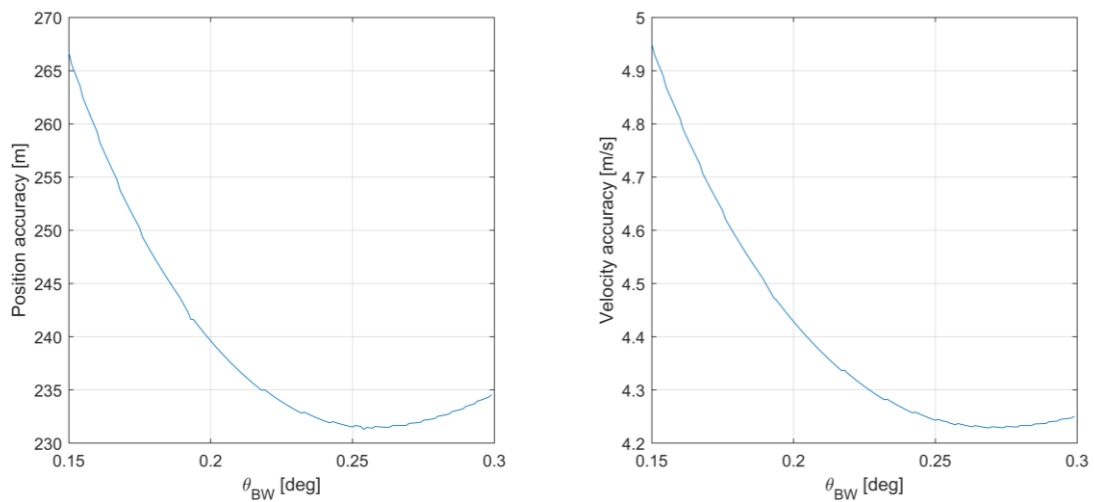
Figure 7.9: Position and velocity accuracy as function of θ_{BW}, for an object crossing the fence close to its edge.
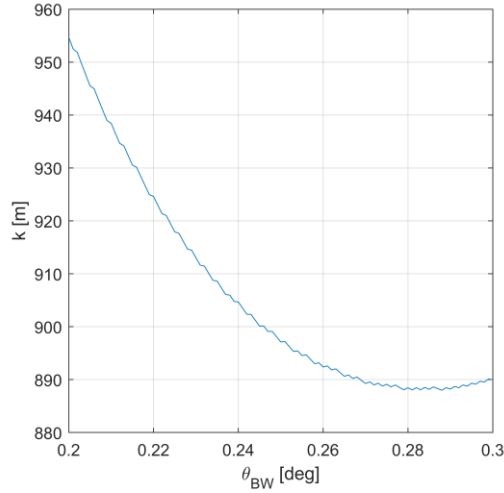
Figure 7.10: Total cross-range error as function of θ_{BW}, for an object crossing the fence close to its center.

This analysis clearly illustrates the impact of cross-range error on radar accuracy. Furthermore, the model introduced in the third chapter demonstrates how effectively the second sensor can mitigate the standard deviation of errors perpendicular to the first sensor's field of regard due to cross-elevation error. However, this reduction does not occur in the other direction. Hence, it is apparent that radar accuracy is linked to the parameter $\sigma_{cr,\varphi}$. This parameter can be diminished through two approaches: narrowing the beamwidth in the cross-range direction or enhancing the signal-to-noise ratio. The latter can be achieved by developing a sensor capable of detecting an object with the same radar cross-section and detection probability but at a greater distance. For instance, designing the radar for a 2000 km target range instead of 1515 km would decrease the error influenced by the signal-to-noise ratio by a factor of

$$\left(\frac{\rho_{ref,1}}{\rho_{ref,2}}\right)^2 = \left(\frac{1515}{2000}\right)^2 = \frac{1}{1.7427}. \tag{7.18}$$

The updated design range necessitates a higher gain to maintain the same signal-to-noise ratio at the new distance. This necessitates a narrower beamwidth, consequently enhancing radar accuracy once more. However, this improvement comes at the cost of requiring a larger reflector. The enhancements in tracking performance are depicted in Figure 7.11, illustrating the position accuracy for an object crossing the fence near the edge with the new design. In this worst-case scenario, the new tracking accuracy is approximately 120 meters, which is deemed acceptable. For the final design, values of θ_{BW} and 0.1 for φ_{BW} are chosen to establish an optimal beamwidth in the worst-case scenario. As a result, the transmitted power can be decreased to meet the required probability of detection:

$$P_{tx} = SNR \frac{(4\pi)^3 \rho^4 k_B T_S}{G^2 \lambda^2 \sigma \, M\tau} = 254.56 \text{ kW}, \tag{7.19}$$

with approximately 444 watts of power allocated to each of the 573 antenna elements and a reflector dimension of 29 meters by 58 meters.
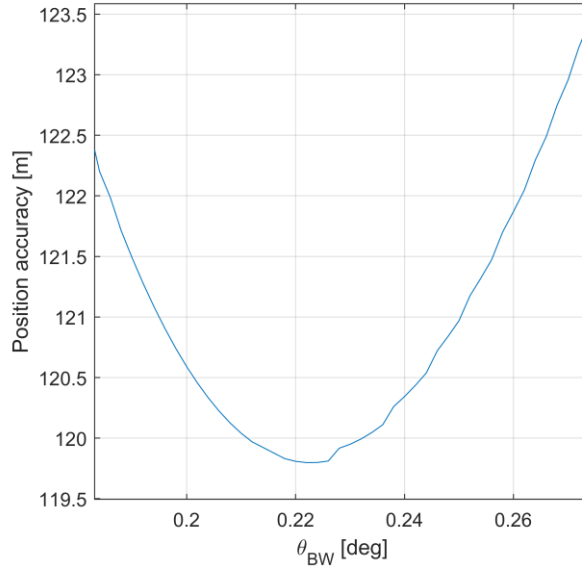
Figure 7.11 Position accuracy as function of θ_{BW}, for an object crossing the fence close to its edge and a reference range of 2000 km.

7.3   Radar performance simulation

This final paragraph is dedicated to simulating radar performance. In this phase, a considerable number of objects undergo simulation, allowing for the comparison between their real positions and velocities with those detected by the radar, in the RSW-frame. To assess radar performance across various orbits, multiple simulations are conducted, each defined by distinct distributions of Keplerian elements and involving 1000 objects. Of particular importance are the semi-major axis and inclination, parameters for which the objects in Low Earth Orbit (LEO) have been categorized into different bands, as detailed in Chapter 5. Each simulation is characterized by a specific semi-major axis value, aligned with the reference value of its respective band. Additionally, the inclination is assigned a Gaussian distribution centered at the band's central value. The optimal fit for the eccentricity distribution of space debris is determined to be an exponential distribution, with an expected value which depends on the orbit altitude. Concerning the Right Ascension of the Ascending Node (Ω), a uniform distribution is assumed. It has been observed that an object passes near the radar location approximately every 12 hours within a longitude interval dependent on the object's revolution period. To reduce the simulation time, objects with a random RAAN within this interval are generated, ensuring their proximity to the ascending node at the beginning of the simulation, thereby starting with a true anomaly equal to

$$v = -\omega - const\,,\tag{7.20}$$

where the constant represents a small angle necessary for the object to pass the first sensor. This assumption imposes minimal restrictions on the orbit, as the argument of perigee (ω) is assumed to vary randomly between 0 and 360°.

When considering orbits at different altitudes, it is crucial to acknowledge that the radar system is optimized to track objects as small as 2 cm in size, orbiting at an average altitude of 825 km. Therefore, for higher orbits, the minimum detectable object size increases. As per the radar equation, it is evident that the Signal-to-Noise Ratio (SNR) is influenced by the object's size, as expressed by its radar cross-section, and the target range:

$$SNR \sim \frac{\sigma}{\rho^4}.$$ (7.21)

In the worst-case scenario, the target crosses the fence near its edge, making it crucial to determine the radar cross-section value that ensures the same signal-to-noise ratio as in the design scenario. In this instance, the following equation can be formulated as follows

$$\frac{\sigma_{des}}{\rho_{des}^4} = \frac{\sigma(h)}{\rho_{max}^4(h)} \rightarrow \sigma_{dB}(h) = \sigma_{des,dB} + 4\left(\frac{\rho_{max}(h)}{\rho_{des}}\right)_{dB}.$$ (7.22)

where $\rho_{des} = 1515$ km and $\sigma_{des,dB} = -34.11$ dBsm.

The maximum range as a function of orbit altitude has been computed in Chapter 6 (pp. 62). This computation leads to the results showed in Table 7-2, which delineates the radar-cross section the system is capable of tracking for each representative altitude band, along with its conversion to physical size. In the last step of this process, the optical approximation is employed for σ values greater than -34.11 dBsm. Utilizing the 3 GHz frequency, the Rayleigh approximation is effective for objects up to 2 cm in size. It is worth noting that for an orbit altitude of 2000 km, representing the upper limit of Low Earth Orbit (LEO), the radar can track debris as small as 10 cm in physical size.

Table 7-2: Minimum object size trackable for different orbit altitudes.

Representative altitude [km]	Radar cross-section	Physical size [cm]
550	-40.3	~1.5
825	-34.1	2
1000	-31.2	~3
1200	-28.4	~4
1500	-25.1	~6

7.3.1 First altitude band (550 km)

At this altitude, the main inclination bands are the one centered at 50°, due to the high number of satellites, and the one centered at 98°. The mean value for the eccentricity is 0.005, while the minimum RCS is -40.3.

- $40° < i < 60°$

Figure 7.12: Position and velocity error distribution, $h = 550\ km, i_{avg} = 50°$.

Table 7-3: Mean and standard deviation for the position and velocity error, $h = 550\ km, i_{avg} = 50°$.

	Position (m)		Velocity (m/s)	
	μ	σ	μ	σ
R	-0.13	4.63	0.00	0.23
S	1.53	7.13	-0.11	0.22
W	5.69	9.93	-0.40	0.42

The number of objects tracked is 504 out of 1000.

- $94° < i < 102°$

Figure 7.13: Position and velocity error distribution, $h = 550\ km, i_{avg} = 98°$.

Table 7-4: Mean and standard deviation for the position and velocity error, $h = 550\ km, i_{avg} = 98°$.

	Position (m)		Velocity (m/s)	
	μ	σ	μ	σ
R	-5.48	8.82	-0.39	0.70
S	9.02	11.98	-0.31	0.46
W	6.04	10.69	-0.31	0.50

The number of objects tracked is 574 out of 1000.

7.3.2 Second altitude band (825 km)

In this band the main the main inclination bands are the one centered at 98°, due to the two main fragmentations, and the ones centered at 70° and 86°. The mean value for the eccentricity is 0.008, while the minimum RCS is -34.11.

- $60° < i < 80°$
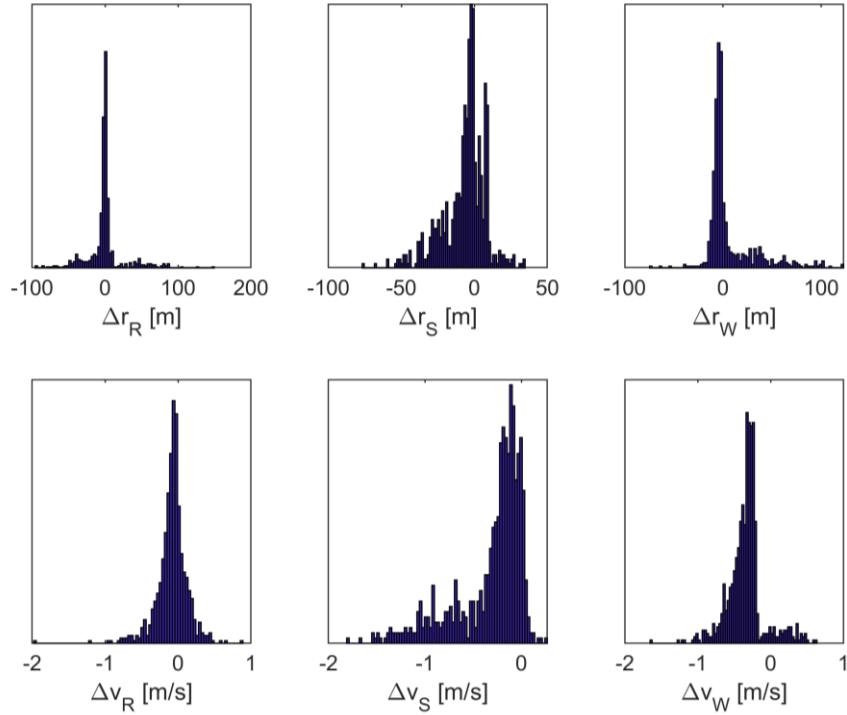
Figure 7.14: Position and velocity error distribution, $h = 825\ km, i_{avg} = 70°$.

Table 7-5: Mean and standard deviation for the position and velocity error, $h = 825\ km, i_{avg} = 70°$.

	Position (m)		Velocity (m/s)	
	μ	σ	μ	σ
R	-0.15	25.3	-0.08	0.21
S	-6.48	14.9	-0.32	0.36
W	6.22	25.3	-0.34	0.26

The number of objects tracked is 715 out of 1000.

- $80° < i < 92°$
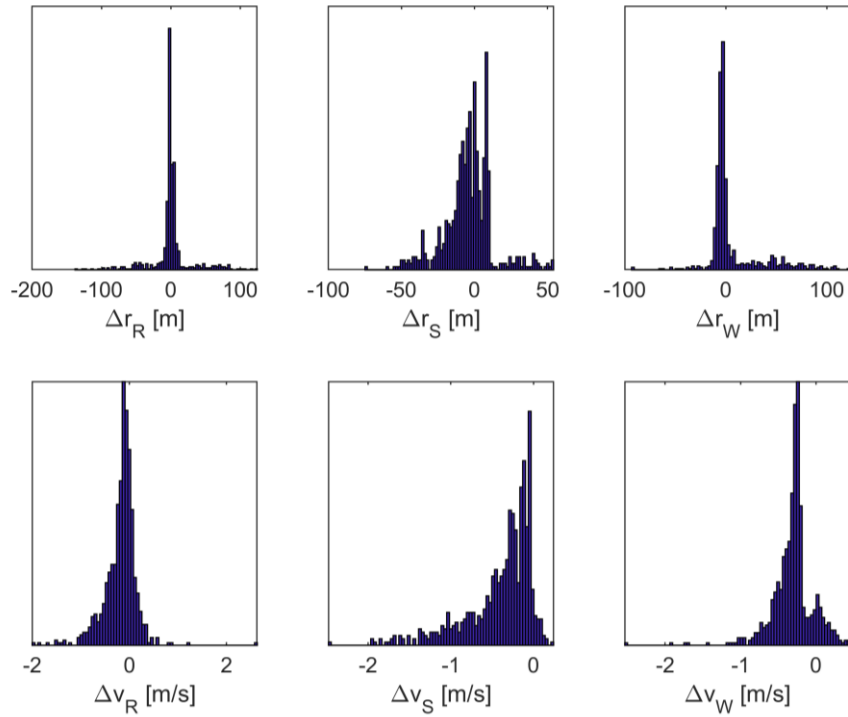
Figure 7.15: Position and velocity error distribution, $h = 825\ km, i_{avg} = 86°$.

Table 7-6: Mean and standard deviation for the position and velocity error, $h = 825\ km, i_{avg} = 86°$.

	Position (m)		Velocity (m/s)	
	μ	σ	μ	σ
R	-0.12	28.2	-0.18	0.34
S	-3.39	17.0	-0.40	0.41
W	6.36	27.4	-0.30	0.27

The number of objects tracked is 729 out of 1000.

- $94° < i < 102°$
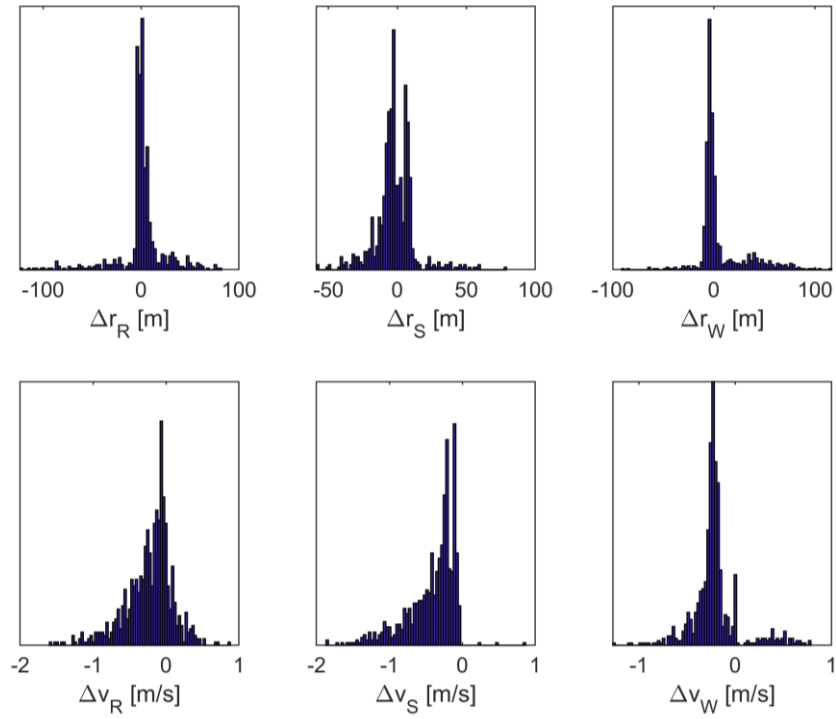
Figure 7.16: Position and velocity error distribution, $h = 825\ km, i_{avg} = 98°$.

Table 7-7: Mean and standard deviation for the position and velocity error, $h = 825\ km, i_{avg} = 98°$.

	Position (m)		Velocity (m/s)	
	μ	σ	μ	σ
R	0.59	23.74	-0.23	0.33
S	-2.00	14.3	-0.42	0.34
W	5.87	24.1	-0.21	0.25

The number of objects tracked is 715 out of 1000.

7.3.3 Third altitude band (1000 km)

At this altitude, the main inclination bands are the one centered at 98°, due to the two main fragmentations, and the one centered at 70°. The mean value for the eccentricity is 0.016, while the minimum RCS is -31.2.

▪ $60° < i < 80°$
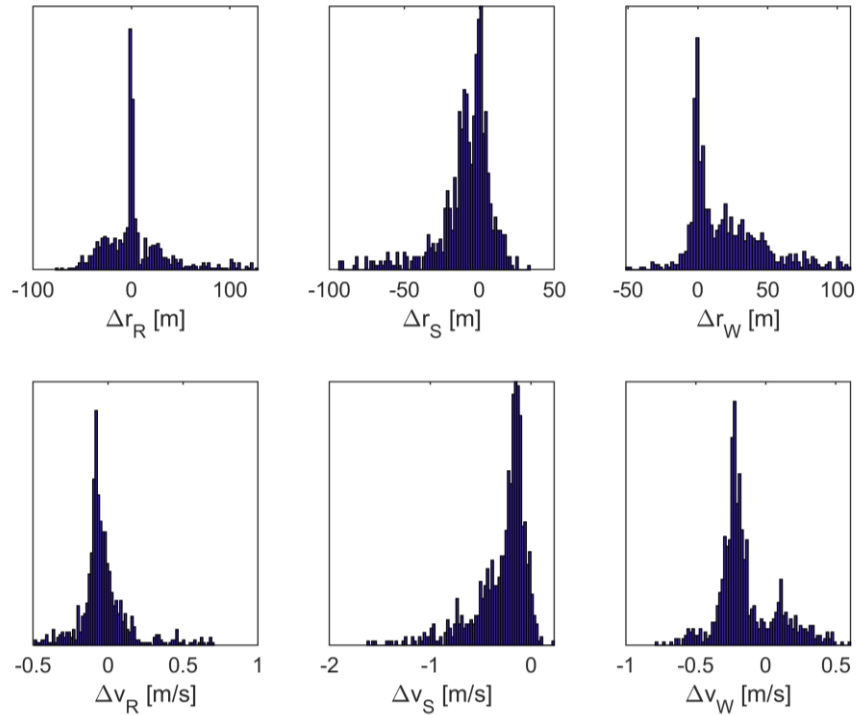
Figure 7.17: Position and velocity error distribution, $h = 1000\ km, i_{avg} = 70°$.

Table 7-8: Mean and standard deviation for the position and velocity error, $h = 1000\ km, i_{avg} = 70°$.

	Position (m)		Velocity (m/s)	
	μ	σ	μ	σ
R	3.38	32.5	-0.03	0.17
S	-9.18	18.4	-0.29	0.27
W	19.5	27.0	-0.14	0.22

The number of objects tracked is 763 out of 1000.

- $94° < i < 102°$
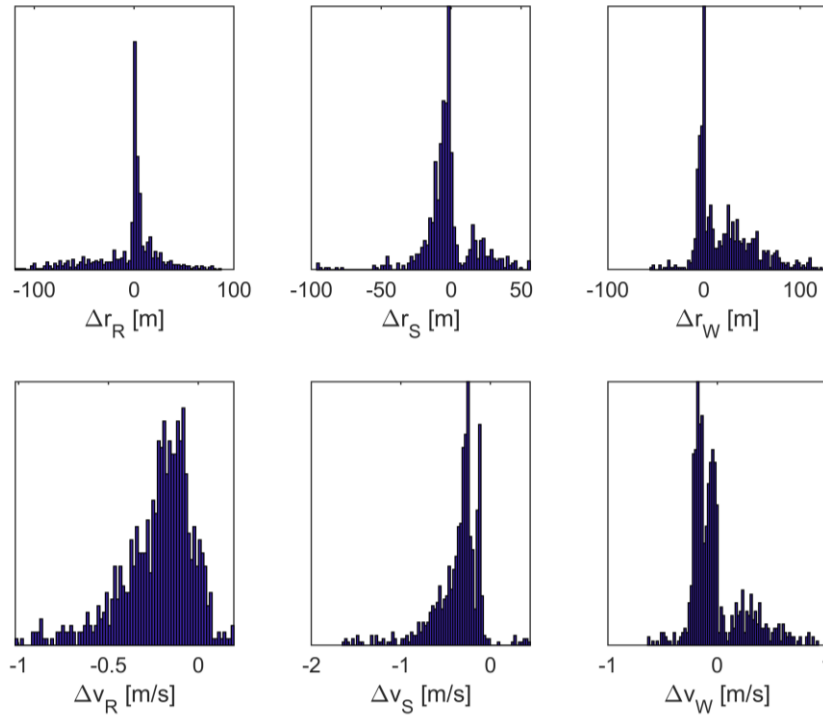
Figure 7.18: Position and velocity error distribution, $h = 1000\ km, i_{avg} = 98°$.

Table 7-9: Mean and standard deviation for the position and velocity error, $h = 1000\ km, i_{avg} = 98°$.

	Position (m)		Velocity (m/s)	
	μ	σ	μ	σ
R	-5.11	32.6	-0.23	0.20
S	-2.57	18.6	-0.37	0.28
W	20.5	30.7	-0.01	0.25

The number of objects tracked is 766 out of 1000.

7.3.4 Fourth altitude band (1200 km)

At this altitude, the main inclination band is the one centered at 86°. The mean value for the eccentricity is 0.02, while the minimum RCS is -28.4.

- $80° < i < 92°$
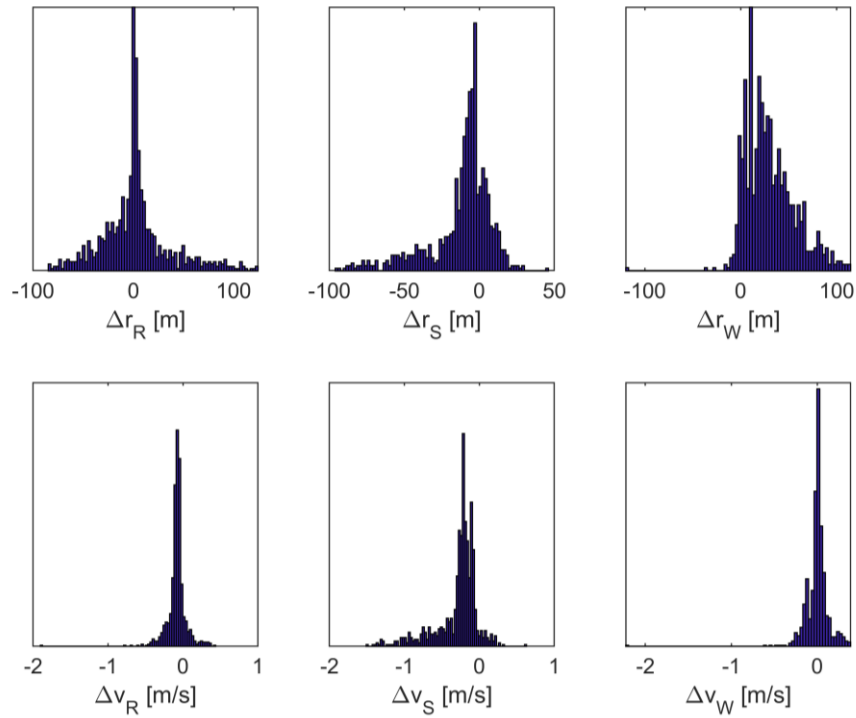
Figure 7.19: Position and velocity error distribution, $h = 1200\ km, i_{avg} = 86°$.

Table 7-10: Mean and standard deviation for the position and velocity error, $h = 1200\ km, i_{avg} = 86°$.

	Position (m)		Velocity (m/s)	
	μ	σ	μ	σ
R	2.32	34.0	-0.08	0.13
S	-9.18	21.1	-0.29	0.28
W	30.3	25.6	-0.00	0.14

The number of objects tracked is 932 out of 1000.

7.3.5 Fifth altitude band (1500 km)

At this altitude, the main inclination bands are the one centered at 98° and the one centered at 70°. The mean value for the eccentricity is 0.023, while the minimum RCS is -25.1.

- $60° < i < 80°$
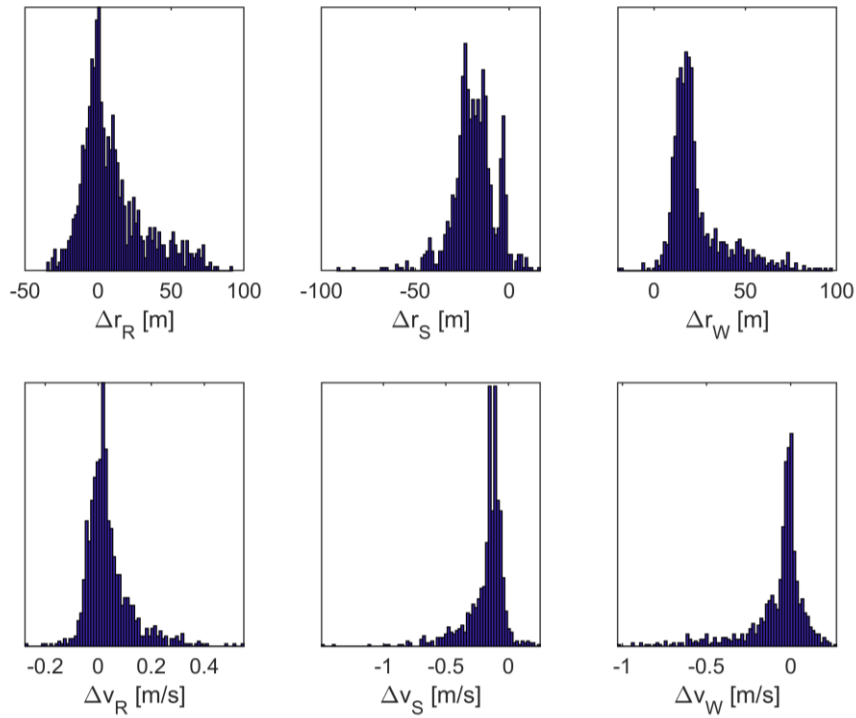
Figure 7.20: Position and velocity error distribution, $h = 1500\ km, i_{avg} = 70°$.

Table 7-11: Mean and standard deviation for the position and velocity error, $h = 1500\ km, i_{avg} = 70°$.

	Position (m)		Velocity (m/s)	
	μ	σ	μ	σ
R	9.21	21.9	0.04	0.09
S	-18.7	11.5	-0.18	0.16
W	23.8	15.9	-0.08	0.18

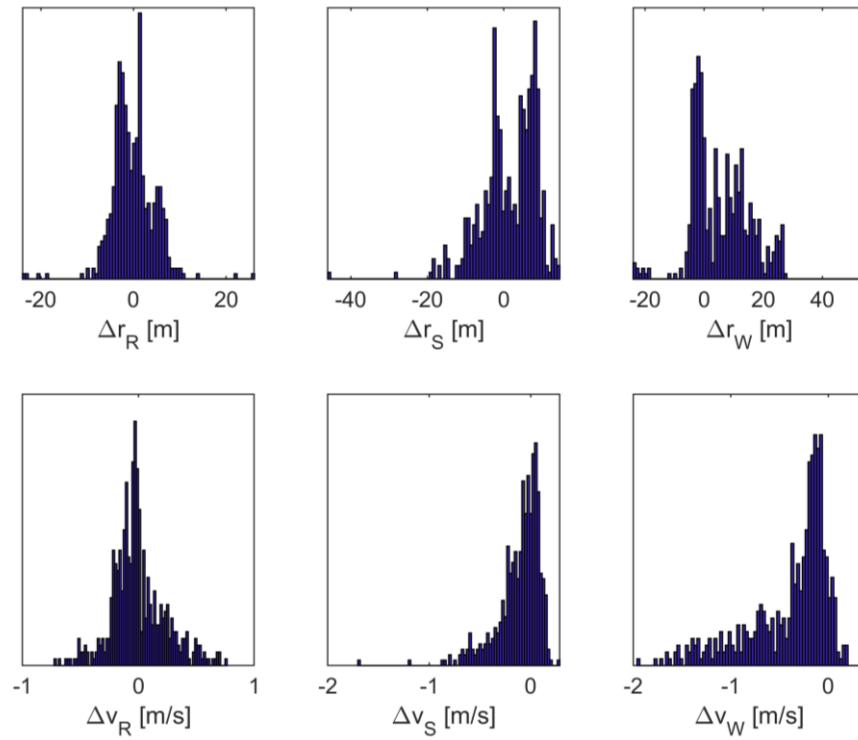The number of objects tracked is 981 out of 1000.

- $94° < i < 102°$

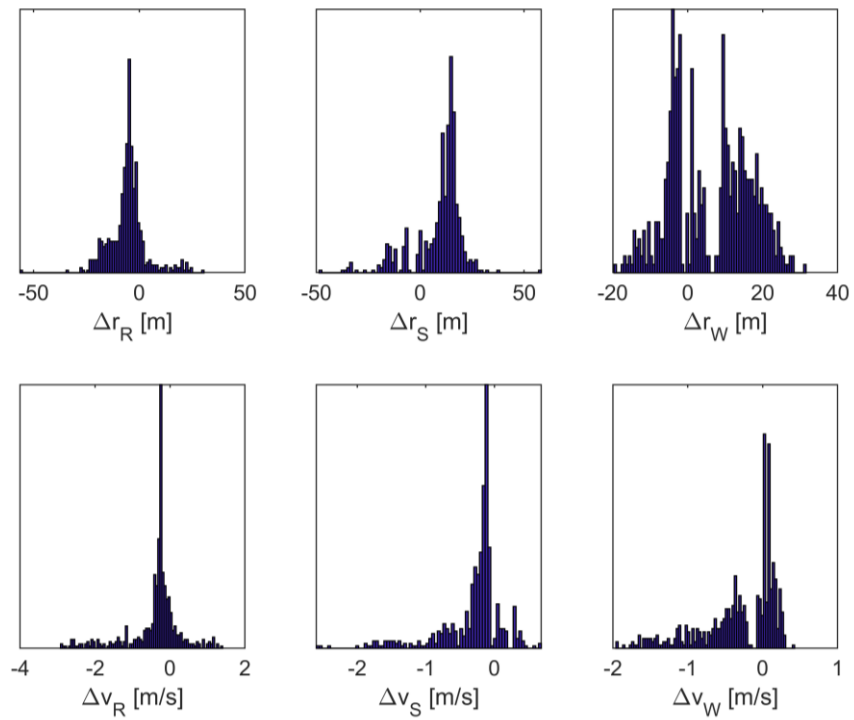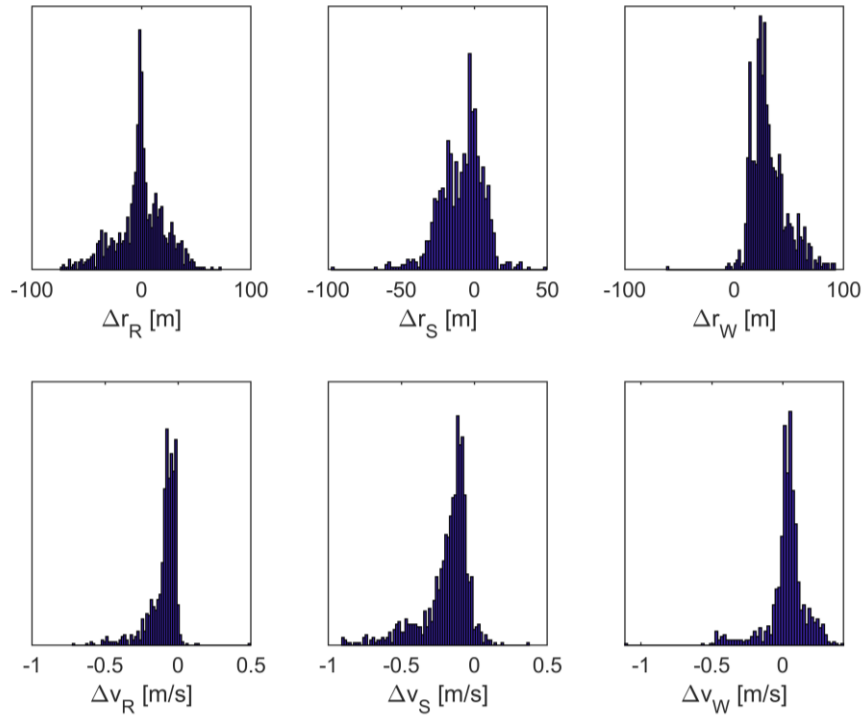*Figure 7.21: Position and velocity error distribution, $h = 1500\ km, i_{avg} = 98°$.*

Table 7-12: Mean and standard deviation for the position and velocity error, $h = 1500\ km, i_{avg} = 98°$.

	Position (m)		Velocity (m/s)	
	μ	σ	μ	σ
R	-1.00	22.4	-0.10	0.10
S	-8.61	14.9	-0.19	0.17
W	31.7	16.3	-0.03	0.14

The number of objects tracked is 961 out of 1000.

7.4 Results Analysis

The presented results validate those of the three-dimensional fence model. Primarily comprising orbits with high inclinations, the double-fence design effectively mitigates position errors in the R and S components, while W component errors persist. Notably, velocity errors predominantly affect the S component, especially for orbits with low eccentricity. Comparing orbits within the same inclination band but at varying altitudes highlights superior tracking performance at lower altitudes. Additionally, tracking efficacy appears optimal for inclinations between 60° and 80°, aligning with the chosen fence elevation angle aimed at optimizing performance around 76° inclination.

These results stem from a targeted approach focused on enhancing the precision of known space debris tracking. Acknowledging the time required for the beam to cover the entire field of regard, it becomes apparent that searching for new objects within this timeframe poses challenges. One potential remedy involves employing diverse sensors covering smaller cross-elevation sectors while maintaining the overall field of regard.

To significantly expand the cataloging of space debris, a comprehensive radar network must be established, ensuring coverage across all possible orbits, and minimizing revisit times for each object.

Conclusions

This study has primarily focused on designing a radar system based on the configuration used by the LeoLabs Kiwi Space Radar. The first goal was to compute the optimal elevation angle for the V-shape fence radar.

To achieve this objective, a simple 2D model was initially developed. While this model considered circular orbits with the radar situated within the orbital plane, it provided valuable insights and preliminary results. As a result, it served as a foundational framework for the subsequent development of the 3D model, which enabled the examination of more general scenarios. Within the 3D model, the impact of orbital inclination on the optimal elevation angle was explored. Furthermore, the model allows for the variation of other parameters, including the RAAN and eccentricity. This flexibility can facilitate the computation of the set of values for distance and range ratio detected by the radar across different orbits, aiding in the detailed radar design process. Additionally, the model allows for adjustments to the radar's position and orientation, offering the potential to assess its capabilities for measuring several types of orbits.

After optimizing the fence elevation angle, the radar's other parameters were designed, creating a scenario that considers cataloged objects in Low Earth Orbit. Subsequently, radar performance was simulated across various scenarios using an Unscented Kalman Filter for tracking. This comprehensive analysis not only establishes radar capabilities but also validates previously presented study findings.

Despite employing straightforward equations to model the radar system and target dynamics, this study offers valuable insights into the issue. It highlights both the advantages and limitations of the double-fence configuration while providing a versatile tool for analyzing various configurations.

References

[1]   Ahme Gad & Ossama Abdelkhalik. 2009. Repeated Shadow Track Orbits for Space-Sun Setter Missions.

[2]   Banchoff Thomas & John Wermer. 1993. *Linear Algebra Through Geometry*. Springer.

[3]   Barton David Knox. 2013. Radar Equations for Modern Radar: Beamshape Loss for Different Patterns. Artech House.

[4]   Bridget Bertoni. 2010. Multi-dimensional Ellipsoidal Fitting.

[5]   Brooker Graham. 2009. Introduction to Sensors for Ranging and Imaging.

[6]   Cai Han & Yang Yang & Gehly Steve & He Changyong & Jah Moriba. 2020. Sensor tasking for search and catalog maintenance of geosynchronous space objects. *Acta Astronautica*.

[7]   Christoph Reising & Ludger Prunte. Noise figure calculation for space surveillance radar systems.

[8]   Chuong B. Do. 2008. The Multivariate Gaussian Distribution.

[9]   Clifford A. A. 1973. Multivariate error analysis: a handbook of error propagation and calculation in many-parameter systems. John Wiley & Sons.

[10]   Eduard Gamper. 2015. Analysis and Implementation of an Unscented Kalman Filter for Orbit Determination: Studienarbeit, Institute of Space Systeme - Technische Universitat Braunschweig.

[11]   Eduard Gamper & Christopher Kebschull & Enrico Stoll. Statistical orbit determination using the Ensemble Kalman Filter.

[12]   ESA. 2022. *Space debris by the numbers* (March 2022). Retrieved from https://www.esa.int/%20Safety_Security/Space_Debris/%20Space_debris_by_the_numbers.

[13]   ESA ESOC. 2022. ESA'S ANNUAL SPACE ENVIRONMENT REPORT.

[14]   Everett Rebecca et al. 1991. Summary of Processing of January 1991 SPC Debris Data: XonTech Report 910383-1965.

[15]   G. Richard Curry. *Radar System Performance Modeling.* (2nd ed.). Artech House.

[16]   Gu Min-Hee & Cho Chihyun & Chu Hahng-Yun & Kang No-Weon & Lee Joo-Gwang. 2021: Uncertainty propagation on a nonlinear measurement model based on Taylor expansion.

[17]   Hu Weidong & Fang Aili & Xu Jin. 2006. Radar fence for space debris measurement. Space Debris Res. 6 (3), 42–47 (in Chinese).

[18]   2007. IADC Space Debris Mitigation Guidelines: IADC-02-01 Revision 1 (Sep. 2007).

[19]   International Telecommunication Union. 2019. Attenuation by Atmospheric Gases Recommendation ITU-R P.676-12, P Series, Radiowave Propagation.

[20]   Kessler D. & Stansbery E. & Zhang J. & Matney M. & Eichler P. & Reynolds R. & Anz-Meador Phillip. 1996. A Computer-Based Orbital Debris Environment Model for Spacecraft Design and Observation in Low Earth Orbit.

[21]   LeoLabs. *LeoLabs platform visualization*. Retrieved from https://platform.leolabs.space/visualizations/leo.

[22]   MathWorks. *Detect and Track LEO Satellite Constellation with Ground Radars*. Retrieved from https://it.mathworks.com/help/fusion/ug/detect-and-track-a-LEO-satellite-constellation-with-ground-radars.html.

[23]   MathWorks. *Radar Coordinate Systems and Frames*. Retrieved from https://it.mathworks.com/help/radar/ug/radar-coordinate-systems-and-frames.html.

[24]   Matthew A. Stevenson. Measurement Precision and Orbit Tracking Performance of the Kiwi Space Radar.

[25]   Merrill I. Skolnik. Introduction to Radar Systems, Third Edition.

[26]   Nadav Neuberger. Signal Processing for Space Surveillance Radar. Fraunhofer Verlag.

[27]   NASA Orbital Debris Program Office. *Astromaterials Research & Exploration Science*. Retrieved from https://orbitaldebris.jsc.nasa.gov/.

[28] NASA Orbital Debris Program Office. 2008. *History of On-Orbit Satellite Fragmentations*: *pp. 26, 386.* (14th ed.).

[29] Nicholson Brendon. 2012. World fury at satellite destruction. *The Age.*

[30] Pardini Carmen & Anselmo Luciano. Evolution of debris cloud generated by the FENGYUN-1C fragmentation event: Space Flight Dynamics Laboratory.

[31] Richard Curry. Radar System Performance Modeling, Second Edition.

[32] Shin Yuchul & Yoon Seyoung & Seo Yongmyung & Jin Ho & Seon Jongho. 2015. Radiation effect for a CubeSat in slow transition from the Earth to the Moon: Advances in Space Research.

[33] Space News. 2016. 10 breakups account for 1/3 of catalogued debris (Apr. 2016).

[34] Space-track.org. *Bulk Catalog Data Downloads*. Retrieved from https://www.space-track.org/.

[35] SRI International. 2016. 1D Phased Array antenna for Radar and Communications. Retrieved from.

[36] Stansbery E. G. et al. 1994. Haystack Radar Measurements of the Orbital Debris Environment: Appendix A: Detailed Description of the Data Collection and Data Processing.

[37] Tsui James Bao-Yen. 2000. Fundamentals of Global Positioning System receivers: A software approach. (3rd ed.). John Wiley & Sons.

[38] Vavrin A. B. 2015. Solar Cycle Sensitivity Study of Breakup Events in LEO: Orbital Debris Quarterly.

[39] Weisstein Eric W. *Eccentric Anomaly*: *From MathWorld--A Wolfram Web Resource*. Retrieved from https://mathworld.wolfram.com/EccentricAnomaly.html.

Appendix

A.   Radar measurements to Keplerian elements

```matlab
% Calculate the target Keplerian elements from the radar measurements
% Inputs:
%    r1: vector containing the position coordinates of the first radar detection
%    r2: vector containing the position coordinates of the second radar detection
%    t:  t(1) time of the first detection; t(2) time of the second detection
% Output
%    x:  vector containing the target Keplerian elements,
%    x = [SMA ECC INC RAAN AP T0]'

function [x, res] = myrad2kep(r1, r2, t)

    dt = t(2)-t(1); % delta-time between the two detections

    % Rotation Matrix around x and z-axis
    Rx = @(t) [1 0 0; 0 cos(t) -sin(t); 0 sin(t) cos(t)];
    Rz = @(t) [cos(t) -sin(t) 0; sin(t) cos(t) 0; 0 0 1];

    % Inclination and RAAN computation
    n = sign(dt)*cross(r1, r2)/norm(cross(r1, r2));
    k = [0,0,1];
    inc = acos(k*n);
    raan = atan2(n(1), -n(2));

    % Compute the matrix to pass from the ECI frame to the orbital frame
    Rorb = @(inc,raan) Rx(-inc)*Rz(-raan);

    % Express the detections in the orbital frame
    r1_orb = Rorb(inc,raan)*r1;
    r2_orb = Rorb(inc,raan)*r2;

    % Compute the argument of perigee
    omega1 = atan2(r1_orb(2),r1_orb(1));
    omega2 = atan2(r2_orb(2),r2_orb(1));

    % Numerical method
    %normalize the parameters
    a_star = max(norm(r1),norm(r2)); % length-scale
    r1_adim = r1_orb(1:2)/a_star;
    r2_adim = r2_orb(1:2)/a_star;
    da0 = 10;
    a0 = 1; % initial value for the semi-major axis
    it = 1000; % max number of iterations
    tol = 1e-8; % tolerance threshold to stop the iterations
    k = 1; % factor to prevent the method from diverging

    for i=1:it

        % Ellipse equation (r-rc)'*E*(r-rc)-1 = 0
        A = @(x) cos(x(2))^2+1/(1-x(1)^2)*sin(x(2))^2;
        B = @(x) sin(x(2))^2+1/(1-x(1)^2)*cos(x(2))^2;
        C = @(x) 1/2*sin(2*x(2))*(1-1/(1-x(1)^2));
        E = @(x) 1/a0^2*[A(x) C(x); C(x) B(x)];
        rc = @(x) -a0*x(1)*[cos(x(2)); sin(x(2))];
        fun =  @(x) [(r1_adim-rc(x))'*E(x)*(r1_adim-rc(x)) - 1;...
                     (r2_adim-rc(x))'*E(x)*(r2_adim-rc(x)) - 1];
```

```matlab
            % ECC and AOP computation
            options = optimset('Display','off');
            ntry = 1e3;
            aop_try = linspace(0,2*pi,ntry);
            if i==1
                for j=1:ntry
                    [x,res,flag] = fsolve(fun,[0;aop_try(j)],options); % x=[ECC AP]
                    if flag==1 && x(1)<1 && x(1)>0 && norm(res)<1e-5
                        break
                    end
                end
            else
                x = fsolve(fun,x,options);
            end
            %check the ECC to fall within the interval [0, 1]
            %and the AP within [0, 2pi]
            if x(1)<0
                x(1) = -x(1);
                x(2) = x(2)+pi;
            elseif x(1)==0
                x(2) = 0;
            end
            x(2) = wrapTo2Pi(x(2));

            % SMA correction
            v1 = omega1-x(2);
            v2 = omega2-x(2);
            dt_i = orbtime([v1,v2],a0*a_star,x(1),0);
            dx = 0.001;
            df = orbtime([v1,v2],(a0+dx)*a_star,x(1),0)-orbtime([v1,v2],...
            (a0-dx)*a_star,x(1),0);
            da = k*2*(abs(dt)-abs(dt_i))/df*dx;

            % Convergence check and update
            if abs(da0)<abs(da)
                k = -1*k;
                da = k*2*(abs(dt)-abs(dt_i))/df*dx;
            end
            a1 = a0+da;
            a0 = a1;
            da0 = da;

            % Stop the iterations if the correction is smaller than tol
            if abs(da)<tol
                break
            end
        end

    end
```

B.   Radar Tracking Model

```matlab
global plat

% Generate a population of debris
numObj = 1e3;
semiMajorAxis = earthRadius + 825e3*ones(numObj,1);
eccentricity = 0.015 + 0.005*randn(numObj,1);
eccentricity(eccentricity<0) = 0;
inclination = 70 + 10/3*(randn(numObj,1));
rightAscension = [0; dRaan*(rand(numObj-1,1)-1/2)];
argOfPerigee = 360*rand(numObj,1);
trueAnomaly = 360*rand(numObj,1);

% Radar parameters
rcsRef = 0;      % reference radar cross-section[dB]
rgRef = 2000e3; % reference range [m]
freq = 3e9;      % carrier frequency
elBW = 0.2;      % elevation beamwidth [deg]
azBW = 0.1;      % cross-elevation beamwidth [deg]
pd = 0.99;       % probability of detection
M = 3;           % number of integrated pulses
PRF = 45;        % pulse repetition frequency
% Radar geometry
FOR = [120;elBW];   % field of regard [deg]
el = 67;            % fence elevation [deg]
MountingAngles = [0 el 0 0 180-el 0];

% Create a satellite scenario
satscene = satelliteScenario;
% Add satellites from Keplerian elements
obj = satellite(satscene,semiMajorAxis,eccentricity,inclination, ...
    rightAscension,argOfPerigee,trueAnomaly,"OrbitPropagator","two-body-keplerian");
set(satscene.Satellites,'MarkerSize',2)
set(satscene.Satellites,'MarkerColor',[1,0,0])

% Time interval of the simulation
minTimeStep = 0.07; % integration time = PRF/M
maxTimeStep = 7;
step = 1;
time = 0;
fast = 0; % flag to speed-up the simulation
satscene.StopTime = satscene.StartTime + seconds(maxTimeStep);
satscene.SampleTime = maxTimeStep;
stopSim = 12; % simulation duration[h]

% Get constellation positions and velocity at the beginning of the simulation
plats = repmat(...
    struct('PlatformID',0,'Position',[0 0 0], 'Velocity', [0 0 0]),...
    1, numel(satscene.Satellites));
for i=1:numel(obj)
    [pos, vel] = states(obj(i),'CoordinateFrame',"ECEF");
    plats(1,i).Position = pos(:,1)';
    plats(1,i).Velocity = vel(:,1)';
    plats(1,i).PlatformID = i;
end


% Radar coordinates in LLA
station = [0 -60 0];
% Create fan-shaped monostatic radars
radar1 = fusionRadarSensor(1,...
    'UpdateRate',PRF,... Hz
    'ScanMode','No scanning',...
```

```matlab
        'MountingAngles',MountingAngles(1:3),...
        'FieldOfView',FOR,...
        'DetectionProbability',pd,...
        'ReferenceRange',rgRef,...
        'ReferenceRCS',rcsRef,...
        'RangeLimits',[0 3500e3],...
        'AzimuthResolution',azBW,...
        'ElevationResolution',elBW,...
        'RangeResolution',15, ... [m]
        'AzimuthBiasFraction',0.01,... fraction of the resolution
        'ElevationBiasFraction',0.01,...
        'RangeBiasFraction',0.1,...
        'HasElevation',true,...
        'HasNoise',false,...
        'HasFalseAlarms',false,...
        'DetectionCoordinates','Sensor Spherical',...
        'TargetReportFormat','Detections');
radar2 = fusionRadarSensor(2,...
        'UpdateRate',PRF,... Hz
        'ScanMode','No scanning',...
        'MountingAngles',MountingAngles(4:6),...
        'FieldOfView',FOR,...
        'DetectionProbability',pd,...
        'ReferenceRange',rgRef,...
        'ReferenceRCS',rcsRef,...
        'RangeLimits',[0 3500e3],...
        'AzimuthResolution',azBW,...
        'ElevationResolution',elBW,...
        'RangeResolution',15, ... [m]
        'AzimuthBiasFraction',0.01,... fraction of the resolution
        'ElevationBiasFraction',0.01,...
        'RangeBiasFraction',0.1,...
        'HasElevation',true,...
        'HasNoise',false,...
        'HasFalseAlarms',false,...
        'DetectionCoordinates','Sensor Spherical',...
        'TargetReportFormat','Detections');

% Define the tracker
tracker = trackerJPDA('FilterInitializationFcn',@initKeplerUKF,...
        'HasDetectableTrackIDsInput',true,...
        'ClutterDensity',1e-20,...
        'AssignmentThreshold',5e4,...
        'DeletionThreshold',[8 8,...
        'ConfirmationThreshold',[3 8]);


% Define coverage configuration of each radar and visualize it on the globe
%calculates the direction cosine matrix dcm for a given set of geodetic latitude and
longitude
ned1 = dcmecef2ned(station(1), station(2));
ned2 = dcmecef2ned(station(1), station(2));
%allows you to specify the position and orientation of the platform on which each sensor
or emitter is mounted
covcon(1) = coverageConfig(radar1,lla2ecef(station),quaternion(ned1,'rotmat','frame'));
covcon(2) = coverageConfig(radar2,lla2ecef(station),quaternion(ned2,'rotmat','frame'));

% Initialize Global Viewer
f = uifigure;
viewer = trackingGlobeViewer(f,'Basemap','satellite','ShowDroppedTracks',...
                             false,'PlatformHistoryDepth',100);
% Initialize tracks and tracks log
confTracks = objectTrack.empty(0,1);

while time < second(satscene.StartTime)+3600*stopSim
```

```matlab
        timeSamples(step) = time;

        % Generate detections of the constellation following the radar
        % processing chain
        targets = assembleRadarInputs(station, plats(step,:));
        isFar = matlabshared.tracking.internal.fusion.targetTruth.isFarAway(targets,3500e3);
        [dets1,numdets1] = radar1(targets, time);
        dets1 = addMeasurementParams(dets1,numdets1,station);
        [dets2,numdets2] = radar2(targets, time);
        dets2 = addMeasurementParams(dets2,numdets2,station);
        %add noise
        dets1 = addNoise(dets1,radar1);
        dets2 = addNoise(dets2,radar2);
        %reduce the atmospheric bias
        dets1 = corrAtmosphericRefraction(dets1);
        dets2 = corrAtmosphericRefraction(dets2);

        % Generate and update tracks
        detections = [dets1; dets2];
        detectableInput = isDetectable(tracker,time, covcon);
        if ~isempty(detections) || isLocked(tracker)
            [confTracks,~,~,info] = tracker(detections,time,detectableInput);
            confTracks = deleteBadTracks(tracker,confTracks);
        end
        trackLog{step} = confTracks;

        % Update viewer
        plotPlatform(viewer, plats(step,:),'ECEF', 'Color',[1 0 0],'LineWidth',1);
        plotDetection(viewer, detections,'ECEF');
        plotTrack(viewer, confTracks, 'ECEF','Color',[0 1 0], 'LineWidth',3);
            infobox.Text = simulationInfoText(time, numel(confTracks), numDebris);

        % Reduce the time-step if a target is closed to the radar FOV
        slow = isClose(plats(step,(~isFar)),station,fov,el);
        if slow
            timeStep = minTimeStep;
        else
            timeStep = maxTimeStep;
        end

        % Propagate objects to the next time step
        step = step + 1;
        time = time + timeStep;
        for i=1:numel(obj)
            pos = plats(step-1,i).Position;
            vel = plats(step-1,i).Velocity;
            state = [pos(1); vel(1); pos(2); vel(2); pos(3); vel(3)];
            state = keplerorbit(state,timeStep);
            pos = state([1,3,5]);
            vel = state([2,4,6]);
            plats(step,i).Position = pos';
            plats(step,i).Velocity = vel';
            plats(step,i).PlatformID = i;
        end
    end

end
```

```matlab
%%%%%%%%%%%%%%%%%%%%%%%%%%% Supporting functions %%%%%%%%%%%%%%%%%%%%%%%%%%%%

% initKeplerUKF initializes an Unscented Kalman filter using the Keplerian
% motion model.
function filter = initKeplerUKF(detection)
global plat
radarsphmeas = detection.Measurement;
% measmodel= @(x,varargin) x([1 3 5],:);
[x, y, z] = sph2cart(deg2rad(radarsphmeas(1)),deg2rad(radarsphmeas(2)),radarsphmeas(3));
radarcartmeas = [x y z];
Recef2radar = detection.MeasurementParameters.Orientation;
ecefmeas = detection.MeasurementParameters.OriginPosition + radarcartmeas*Recef2radar;
% This is equivalent to:
% Ry90 = [0 0 -1 ; 0 1 0; 1 0 0]; % frame rotation of 90 deg around y axis
% nedmeas(:) = Ry90' * radarcartmeas(:);
% ecefmeas = lla2ecef(lla) +  nedmeas * dcmecef2ned(lla(1),lla(2));
sigpos = 1000; % [m]
sigvel = 100; % [m/s^2]
sigposMeas = deg2rad(sqrt(detection.MeasurementNoise(1)))*detection.Measurement(3);
pos = plat(end,1).Position+sigpos*randn(1,3);
vel = plat(end,1).Velocity+sigvel*randn(1,3);
% catalogued object
initState = [pos(1); vel(1); pos(2); vel(2); pos(3); vel(3)];
% new object
% initState = [ecefmeas(1); 0; ecefmeas(2); 0; ecefmeas(3); 0];
filter = trackingUKF(@keplerorbit,@cvmeas,initState,...
    'Alpha', 1e-0, 'Beta', 2, 'Kappa', 0, ...
    'StateCovariance', diag(repmat([sigpos, sigvel].^2,1,3)),...
    'ProcessNoise',diag(repmat([0, 0].^2,1,3)),...
    'MeasurementNoise',detection.MeasurementNoise);
end


%%%%%%%%%%%%%%%%%%%%%%%%%%%%%%%%%%%%%%%%%%%%%%%%%%%%%%%%%%%%%%%%%%%%%%%%%%%%%%%

function state = keplerorbit(state,dt)
% keplerorbit performs numerical integration to predict the state of
% Keplerian bodies. The state is [x;vx;y;vy;z;vz]
% Runge-Kutta 4th order integration method:
k1 = kepler(state);
k2 = kepler(state + dt*k1/2);
k3 = kepler(state + dt*k2/2);
k4 = kepler(state + dt*k3);
state = state + dt*(k1+2*k2+2*k3+k4)/6;
    function dstate=kepler(state)
        x = state(1,:);
        vx = state(2,:);
        y = state(3,:);
        vy = state(4,:);
        z = state(5,:);
        vz = state(6,:);
        mu = 398600.4405*1e9; % m^3 s^-2
        omega = 7.292115e-5; % rad/s
        r = norm([x y z]);
        g = mu/r^2;
        fs = zeros(3,1);
        % Coordinates are in a non-intertial frame, account for Coriolis
        % and centripetal acceleration
        ax = -g/r*(x+fs(1)) + 2*omega*vy + omega^2*x;
        ay = -g/r*(y+fs(2)) - 2*omega*vx + omega^2*y;
        az = -g/r*(z+fs(3));
        dstate = [vx;ax;vy;ay;vz;az];
    end
end


%%%%%%%%%%%%%%%%%%%%%%%%%%%%%%%%%%%%%%%%%%%%%%%%%%%%%%%%%%%%%%%%%%%%%%%%%%%%%%%
```